Title
Searches for Anomalous Resonances in the Large Hadron Collider for New Physics

Author
Ng, Ying Wun Yvonne

Publication Date
2022

Peer reviewed|Thesis/dissertation

UNIVERSITY OF CALIFORNIA,
IRVINE

Searches for Anomalous Resonances in the Large Hadron Collider for New Physics

DISSERTATION

submitted in partial satisfaction of the requirements
for the degree of

DOCTOR OF PHILOSOPHY

in Physics

by

Yvonne Ng

Dissertation Committee:
Professor Daniel Whiteson, Chair
Professor Tim Tait
Professor Andrew Lankford

2022

TABLE OF CONTENTS

LIST OF FIGURES

LIST OF TABLES

ACKNOWLEDGMENTS

First of all, I would like to thank my advisor Daniel Whiteson and Andy Lankford for the guidance, support, trust, and freedom they have given me over the years. I am especially grateful for Daniel's continuous encouragement towards my growth into an independent researcher.

I would also like to thank my postdocs Dan Guest and Mike Fenton. Thank you for all the big and small advice on my work and personal encouragements over the years- sometime in the form of French Kabob runs or pandemic zoom coffees sessions. A special thank you is also dedicated to Kate Pachal, for your generous support through my first major analysis, for teaching me so much that I know now, and for the afternoon cake time at R1. I will strive to be like what you all were to me to my future students.

I am grateful for my colleagues at CERN, especially Verena Martinez, Bill Murray, Ben Nachman, Bogdan Malaescu, Caterina Doglioni, Christopher Haynes, Ljiljana Morvaj, Heather Russell, and Kyle Cranmer. The end product of this thesis would not have the same rigor without your technical comments and contributions.

A gratitude is also extended to my informal advisors in Irvine, Tim Tait, Muchun Chen, Simona Murgia, and Michael Ratz for the intellectual support and advice. I also want to thank Flip Tanedo for all the coffee and restaurant runs in my first two years of grad school. I was nourished in the mind, in my stomach, and also in my caffeine level. I also want to thank Chase and Seyda for all the thought-provoking chats.

If I am allowed the indulgence to take it back to where the journey begins, I want to thank my middle science teacher Miss Chau, thank you for always having so much trust in my abilities and for showing me how practical and relatable science is. I also want to thank my math teacher Miss Fung: for both the lessons in math and outside of math. Some words outside of math took me many years more years to understand after class was over. I am grateful to my undergraduate friends and "Senpais" David and Jason, for showing me the fun of solving technical problems with science and engineering and for being great friends. I am also thankful for research time from MC Chu in his lab. I learned not just the rigor of scientific research but also responsibility as a scientist to society. I aspire to continue my efforts of scientific outreach as a postdoc like you have done for so many.

It only took 3 continents to finish my Ph.D. These would not have been possible without the support of my friends across all three continents. Special shout out to Andy, Clare, Diane, Haidee, Alexis, Ros, Yanyi, CY, Rhoda, Alice, Joakim, Lily, Arianna, Freida, Kit, Ho, Amber, Tamara, Kiwi, Shelly, Danny, friends in Kindle Hills. My life in the last few years both instead and outside of physics really wouldn't have been the same without you.

Finally to my family: mom and dad, I hope I made you proud. To my brother Rene, I am lucky to have your support and to have you as a partner in crime through all of life's adventures.

This thesis is for all of you.

Yvonne Ng

University of California, Irvine
Department of Physics and Astronomy
Irvine, CA, USA, 92617

CERN CH-1211
Bâtiment 104-C-R24
23 Genève, Switzerland

Email: yvonne.ng@cern.ch
Phone: +1 949-870-9807

Education:

Ph. D., Particle Physics, University of California, Irvine (Irvine, CA) Sept 2021
Advisor: Prof. Daniel Whiteson

B. S., Physics, *Magna Cum Laude,* University of Texas, Arlington (Arlington, TX) Jul 2015
Advisor: Prof. Andrew White

Research Experience:

Member of the ATLAS Collaboration. 2016-Present

- ***Analysis Contact*** Leading the effort in searching for resonances in the low mass di-muon final state in the ATLAS experiment.
- Conducting study on unconventional signatures in the di-muon final state with a weakly-supervised learning method.
- Developing a Gaussian process based background estimation and signal bump-hunting method with Bayesian inference.
- Initiated the creation and commissioning of a novel data-scouting (trigger level analysis) di-muon trigger geared towards sensitivity improvement for future data taking period.
- Primary developer of the online monitoring software for the New Small Wheel— the ATLAS muon spectrometer upgrade. With activities at a cosmic ray stand and final site of installation.
- Primary analyzer of the dijetISR resolved analysis effort of ATLAS in year 2017-2018. Performed sensitivity study, background modeling, signal injection test, unblinding, limit setting and systematics studies.
- Developed a new jet calibration tool to reduce computation time for the experiment.
- Responsible for data-taking operation as a ATLAS control room shifter at the trigger and run-control desk in year 2017-2018.

Special Author of the DUNE Collaboration 2013-2015

- Seasonal dependence and noise study of the Gas Electron Multiplier detector as a beam aligner for the experiment
- Built hardware prototype detector and maintained the operation of a cosmic ray stand.

- Managed shifts for 5 other undergrads and oversaw the functioning of the Gas Electron Multiplier laboratory.

Research Student at the Chinese University of Hong Kong Summer 2013

- "Cosmological stimulation of galactic cluster collisions at different expansion rates of the universe"
- Advisor: Prof. Ming Chung Chu

Grants, Fellowships and Awards:

- **US ATLAS Center Funding Proposal Award**, (6.3k) (Lawrence Berkeley National Lab.) 2020
  Primary proposal writer, along with Benjamin Nachman and Daniel Whiteson, in support of travel and 3 months of living expenses to LBNL for collaboration on the CWola project.
- **Best Poster Award**, Dark Matter at LHC (Seattle, Washington) 2019
  Poster on "Low mass dijet resonances search using ISR with ~80fb^{-1} $\sqrt{s}$ = 13TeV ATLAS Data"
- **Chancellor's Fellowship** ($20k), University of California, Irvine 2015-2017
- **Magna Cum Laude**, University of Texas at Arlington 2015
- **Dean's List,** University of Texas at Arlington 2011, 2015
- **Travel Award**, National Society of Physics Students, American Physical Society April Meeting 2015
- **Truman D. Black Endowed Scholarship in Physics**, University of Texas at Arlington 2015
- **James L. Horwitz Scholarship**, University of Texas at Arlington 2014

Invited Seminars/Tutorials:

- **Session Convener**, ATLAS Higgs and Diboson Searches Workshop (Virtual) Aug 2020
  On "Background estimation techniques".
- **Particle Physics Seminar**, University of California, Riverside (Riverside, California). Oct 2019
  Talk on "Hunting for weird resonances in the Large Hadron Collider"
- **Smooth Background Fitting Tutorial,** ATLAS Exotics and HDBS Workshop (Naples, Italy) June 2019
  Tutorial on "Gaussian process as a background fitting and signal hunting method"

Conference/Workshop Presentations:

Oral Presentation

- ATLAS Higgs and Diboson Searches Workshop (Virtual) Aug 2020
  Talk on "Overview of established background estimation techniques"
- ATLAS Higgs and Diboson Searches Workshop (Virtual) Aug 2020
  Talk on "Gaussian process on background fitting and limit setting"
- ATLAS Higgs and Diboson Searches Workshop (Virtual) Aug 2020
  Talk on "Motivating the dimuon TLA trigger for ATLAS Run III"

- ATLAS Higgs and Diboson Searches Workshop (Virtual) Aug 2020
  Co-Talk on "Dark Matter reinterpretation on in the Dilepton channel "
- ATLAS Trigger Level Analysis Workshop (Geneva, Switzerland) Dec 2019
  Talk on "Motivating the dimuon trigger level analysis for ATLAS Run 3"
- Southern California Beyond the Standard Model Physics Meeting (Irvine, California) Sep 2019
  Graduate Student Gong Show — Talk on "Resonance finding in the LHC"
- Dark Matter at LHC (Seattle, Washington) Oct 2019
  Talk on "The Unexplored Landscape of Two Body Resonances"
- Latin American Symposium on High Energy Physics (Lima, Peru) Dec 2018
  Talk on "Dark Matter search In ATLAS", *On Behalf of the ATLAS Collaboration*
- American Physical Society National April Meeting, 2015 (Baltimore, Maryland) Apr 2015
  Talk on "Seasonal dependence and aging effect of the Gas Electron Multiplier"

Poster Presentation

- Neural Information Processing System—Women in ML(Vancouver, Canada) Dec 2019
  Poster on "Gaussian process in Collider Physics"
- European Summer School of High Energy Physics (St. Petersburg, Russia) Sep 2019
  Poster on "Low mass dijet resonances search using ISR with ~80fb^{-1} $\sqrt{s}$ = 13TeV ATLAS Data",
  On behalf of the ATLAS Collaboration
- Dark Matter at LHC (Seattle, Washington) Aug 2019
  Poster on "Low mass dijet resonances search using ISR with ~80fb^{-1} $\sqrt{s}$ = 13TeV ATLAS Data",
  On behalf of the ATLAS Collaboration
- Large Hadron Collider Experimental Committee Meeting (Geneva, Switzerland) Feb 2018
  Poster on "The Dijet+ISR Analysis in ATLAS: Searching For Low-Mass Dark Matter Mediator"
- American Physical Society National meeting, 2014 (Savannah, Georgia) Apr 2014
  Poster on "Long Term Multiplication Behavior Studies of the 30cmx 30cm prototype Gas Electron Multiplier"

Professional Services:

Women in Science

- **Local Organizing Committee**, Conference for Undergraduate Women in Physics Jan 2020
  American Physical Society (Irvine, California)
- **Chair for Student Presentation I**, Conference for Undergraduate Women in Physics Jan 2020
  American Physical Society (Irvine, California)
- **Panelist**, Conference for Undergraduate Women in Physics Jan 2020
  American Physical Society (Irvine, California)

- **Mentor**, Conference for Undergraduate Women in Physics — Jan 2020
  American Physical Society (Irvine, California)
- **Popular Science Talk Speaker,** — May 2019
  Talk Titled: "All things matter! — A search for dark matter in the Large Hadron Collider"
  The True Light Girls' Middle School of Hong Kong (Hong Kong)
- **Graduate Mentor** for Undergraduate Women in Physics — 2015-2016
  Women in Physics, Department of Physics and Astronomy
  University of California, Irvine (Irvine California)

Other Professional Service

- **Invited Speaker**, Grad. School Application Workshop 2020 — Oct 2020
  Oxford University Hong Kong Scholar Association (Hong Kong)
- **Invited Panelist**, Hong Kong PhD Symposium 2020 — Jan 2020
  "Scholar's Journal: Triumphs and Struggles beyond PhD"
  Oxford University Hong Kong Scholar Association (Hong Kong)
- **Science Fact-Check**, The New Yorker — Dec 2019
  "Elements — The Histories Hidden in the Periodic Table"
  Journalist: Neima Jahromi
- **Official Tour Guide**, CERN (Geneva, Switzerland) — 2017-Present
- **Volunteer**, Popular Science Outreach @ UC Irvine Astronomy Outreach Program — 2015-2016
- **Volunteer**, National Society of Physics Students @ American Physical Society April Meeting — 2015

Teaching experience:

- **Teaching Assistant**, Basic Physics III for pre-medical and biology students — Spring 2016
- **Teaching Assistant**, Basic Physics II for pre-medical and biology students — Winter 2016
- **Teaching Assistant**, Classical physics for engineering and physical science students — Fall 2015

Last updated: 2020–10-9

Publication List

Ying Wun Yvonne Ng

Published Papers

1. ATLAS Collaboration, *Search for low-mass resonances decaying into two jets and produced in association with a photon using p p collisions at √s = 13TeV with the ATLAS detector*, Phys. Lett. B (2019) 56, 2019, arXiv:1901.10917 [hep-ex]

2. ATLAS Collaboration, *In situ calibration of large-R jet energy and mass in 13 TeV proton-proton collisions with the ATLAS detector*, Eur. Phys. J. C 79 (2019) 135, 2019, arXiv:1807.09477 [hep-ex]

3. ATLAS Collaboration, *Search for light resonances decaying to boosted quark pairs and produced in association with a photon or a jet in proton-proton collisions at √s =13TeV with the ATLAS detector* Phys.Lett. B788 (2019) 316, arXiv:1801.08769 [hep-ex]

4. N. Craig, P. Draper, K. Kong, Y. Ng and D. Whiteson, *The unexplored landscape of two body resonance,* PITT-PACC-1610 arXiv:1610.09392 [hep-ex]

5. Long-Baseline Neutrino Facility (LBNF) and Deep Underground Neutrino Experiment (DUNE), Y. Ng, *Conceptual Design Report Vol.1-2* arXiv:1601.05471[hep-ex]

Work in Progress

1. ATLAS Collaboration, S*earch for low mass resonances in the dimuon and boosted dimuon channel with the ATLAS detector*

2. ATLAS Collaboration, *Dimuon Resonance searches with a weakly supervised learning method CWOLA* [In collaboration with LBNL Scientist Benjamin Nachman]

ABSTRACT OF THE DISSERTATION

Searches for Anomalous Resonances in the Large Hadron Collider for New Physics

By

Yvonne Ng

Doctor of Philosophy in Physics

University of California, Irvine, 2022

Professor Daniel Whiteson, Chair

In this thesis a few approaches are explored to advance resonance finding searches in collider physics. Two analyses in the dimuon and dijet initial-state radiation(ISR)final state resonance are searched using proton-proton collisions at $\sqrt{s}$=13 TeV with an integrated luminosity of 139/fb, collected by the ATLAS experiment. No statistically significant excess is seen in the dijetISR search. In the dimuon search, a novel background estimation method is developed, in which the smooth but unknown background is estimated using a Gaussian process fit.

Chapter 1

Introduction

An eagerness for the truth is part of what makes us human. This has been true across cultures through different times: ancient Greeks who toyed with mathematics of trigonometric objects saw an eternal truth in their beauty; in the Eastern Zhou Dynasty of China[1], influential scholars debated the truthful nature of humans and, therefore, their subsequent duty; driven by the same thirst, in modern days humans took to space, went on the moon and began exploring the extra-terrestrial frontier for beyond earth. The aspiration for truth formed knowledge. It has advanced technology, medicine, law, science, and human psychology. *Everything* in our civilization derives from this ambition in humans to seek truth.

Human's endeavor for the truth is always to uncover something more than what is already known: over two thousand years ago, Plato saw the truth in the *ideal forms* beyond the shadow projections of everyday things [1]; Amongst the mechanical industrial world view 19th century, Immanuel Kant postulated a world of the *transcendental*, a world of the fundamental nature of things, behind the world of *phenomena*, of human senses [2].[2]. In contemporary times of the 21^{st} century, faced with the clash of cultures and perspectives facilitated by the internet and modern transportation, truth is no longer seen as a static set of doctrine or statements of facts in the older days[3], but humans' endeavor to the truth has not stopped.

Combined with the idea of subjectivity, contemporary philosopher Alain Badiou has formulated the logic for the search for truth as "truth procedures": truth is the subsequent discourses and

[1] Eastern Zhou is a Chinese dynasty that existed between 771 to 476 BCE. Influential scholars include *Confucious*, *Lao-tse*, and *Mo-tse*.

[2] Kant in his famous book the Critque of Pure Reasons [2] call this world of the transcedentals the *noumenon* (contrasting with the world of *phenomenon* that can be perceived by human senses. Kant believes this *transcendental* realm that we have no access to is actually the true nature of things. The *transcendental* is sometime referred to as the *thing-in-itself*.)

[3] The view of truth as a direct correspondence to facts is known as the Correspondence theory of truth [3]. Detail objections to the theory can be found in the reference.

knowledge re-development that follows from a rupture or an accident[4] that shatters our existing knowledge system [4]. This "truth procedure" echoes ideas from Thomas Kuhn on scientific *paradigm shifts* [5], but also describes truth seeking as part of individual *ethics*. "There is always only one question in the ethics of truth", Badiou wrote, "how will I, as someone, continue to exceed my own being?"[6]. The search for truth is not seen merely a human desire, but also a moral duty to remain authentic to himself/herself.

Particle physics is a search for truth in the most elementary form. It seeks to understand fundamental particles and their interaction as building blocks to the world around. Not only does it expands knowledge of the smallest possible observable universe, but it is also a study of the things that constitute chemicals, biological cells, animals, highrise structures, and *everything else* under the physical realm. Knowledge in particle physics is also tightly related to objects of the largest scale, namely cosmology, knowledge in particle physics affects the structure of the entire universe, its evolution and is essential to answering questions on the origin of the human.

Particle Physics as a field was developed in the 1960s together with advances in Quantum Field Theory. Through new experimental findings and new theoretical model-building techniques, the Standard Model of Particle Physics was established. The theory is the epitome of human's understanding on the fundamental building block of the universe. The model enjoyed many successes: many predictions made were later confirmed by experimental findings. The J/Ψ, Z, and the Higgs Boson are all discovered that way. Human understanding of matter, its origin, and the governing laws between the interactions has since been greatly advanced.

However, even with its success, there remain many open questions to the Standard Model of Particle Physics. For example, the Standard Model in its current form does not describe gravity or any of its interactions; there is a mathematically unnatural fine tuning of several parameters in the theory; in addition, the Standard Model also does not include dark matter, which makes up the majority of the matter (85%) of the universe or dark energy, which in Einstein's theory explained the expanding universe seen today.

One way of fixing the inconsistency is by finding new particles predicted by different theoretical hypotheses. One way to find these new particles is through high-energy particle collisions. If dark matter interacted weakly with Standard Model particles in the early universe like many theoretical models have come to predict, it would be possible for them to be produced through high-energy collisions of Standard Model particles. One possible signature of Dark matter can be searched in forms of Dark Matter mediator that appears as anomalous resonances.

This thesis offers a few humble attempts to resolve some of these standing problems in the Standard Model of particle physics by discovering new particles that would offer extra insights to future theory

[4]Badiou called such rupture or accident an *Event*

building. These are done by attempting to create previously unobserved conditions in high-energy particle collisions via the Large Hadron Collider. It uses data collected by the ATLAS experiment in the Large Hadron Collider. These new particles, if discovered, as little inconsistencies to the Standard Model of Particle Physics, are nuggets to truth. It has great potential to add to our understanding of fundamental particle physics.

The thesis is organized as the following: chapter 2 describes the history and the description of the Standard Model; chapter 3 discusses the theory of dark matter; chapter 4 presents the experimental setup of the Large Hadron Collider and the ATLAS experiment; chapter 5 covers the common analysis items (reconstruction of objects)and their preparation before the analyses; Chapter 7- 8 outline the analyses that I played a major part in, namely the dijet resolved analysis, and the low mass dimuon analysis; this thesis also covers a future direction for resonance finding in collider physics in Chapter 9, that discusses uncovered resonances in the two body final states. These novel techniques, together with theory-driven approaches, could hold keys to unlocking the next finding that can revolutionalize our current understanding of particle physics.

The pursuit of *Aletheia*(truth) is a nessessity to human *authenticity*, as philosopher Martin Heideigger famously put. This thesis could be seen as a humble response in face of such human condition, or a fulfillment of an ethical duty to remain *authentic*, even if nothing more was achieved. But perhaps there is still more to the pursuit than any eloquent philosopher can ever formulate: it is an adventure of joy and pleasure to uncovering all things unknown. It is a journey that reminds us, what we are is always more than what we know.

Chapter 2

The Standard Model of Particle Physics

Ex pede Herculem.
(From the feet, Hercules.)

–Herodotus, Book IV, Section LXXXII. Plutarch

The Standard Model of Particle Physics (SM) is the epitome of human understanding of physical elementary building blocks to date. From the SM, the properties and interactions of seventeen fundamental particles and their interactions are laid out. It provides the foundational understanding of matter and its interactions on the quantum scale.

This chapter provides an overview of the SM: In Section 2.1, a theoretical description of the SM is given, the mechanism of the theory is discussed, and the Gauge fields and their particles are listed. As a complete picture of the SM relies on experimental measurements of its parameters, the measured values of the eighteen parameters are also cataloged in this section. Despite the many advances made by the SM, there remain many open questions left to be solved. Some of them are motivators to studies performed in this thesis. In Section 2.2, a summarized list of resolved problems to the SM is presented.

2.1 Standard Model: Theoretical Description

Mathematically, the SM is a gauge theory under the Quantum Field Theory (QFT) framework. Particles are represented as different quantized fields operators. The particle interactions are described by the SM Lagrangian which takes the form as shown in Eqaution 2.4. Through the SM

Lagrangian, all physics laws concerning the particle interaction channels, their interaction cross sections and their motion through scattering can be derived.

2.1.1 Symmetry

Symmetry is the cornerstone of many laws in physics. Mathematically, it's the invariance of quantities through transformation, and is shown by the Noether's Theorem [7] to be related to conservation laws in physics:

- Spatial Translational Symmetry ↔ Translational Momentum Conservation
- Time Symmetry ↔ Energy Conservation
- Rotational Symmetry ↔ Angular Momentum Conservation

A symmetry and its transformation can be summarized by the mathematical language of group theory. In group theory, continuous transformation is described by the Lie group and the discrete transformation is represented by a finite group.

There are two kinds of symmetries in the SM, external symmetries and internal symmetries. External symmetries are related to space-time transformation of the particle; internal particle symmetries are related to other particle properties other than space-time.

External Symmetries

External symmetries are transformations on the space-time coordinates, The SM external symmetries can be summarized by the following three groups, known collectively as the *Poincaré group*. Each of the terms conserves a physics quantity.

$$\boldsymbol{P} \times \boldsymbol{J} \times \boldsymbol{K} \tag{2.1}$$

- $\boldsymbol{P}$: Spatial Translational Symmetry

  Abelian Lie group translation on space-time conserves momentum

- $\boldsymbol{J}$: Rotational Symmetry

  Non-Abelian Lie group of three-dimensional rotation conserves Angular Momentum

- $\boldsymbol{K}$: Boost Symmetry

  Abelian Lie group of four dimensions conserves the *Invariant Interval* in Special relativity.

The *Invariant Interval* quantity is defined as:

$$\Delta s^2 \stackrel{\text{def}}{=} c^2 \Delta t^2 - (\Delta x^2 + \Delta y^2 + \Delta z^2) \tag{2.2}$$

In special relativity, when the space-time measurement of an event is transformed through different frames of reference, the *Invariant Interval* remains unchanged. In the equation above, Δs^2 is the Invariant Interval, Δt^2 is the difference in time measurements between the two frames of reference, and Δx, Δy and Δz are the difference in position in between the different frame of reference.

Internal Symmetry

The SM internal symmetries describe the transformation in physical properties of the particles other than space-time. Particle gauge field interactions can be described as "transformations" from one field to another under internal symmetry. The different physical invariant quantities that are conserved under these particle transformations/interactions are called "charges". From these internal symmetries, Charge, Parity and Time reversal symmetry (CPT) is observed.

The internal symmetries are given as:

$$SU(3)_C \times SU(2)_L \times U(1)_Y \tag{2.3}$$

	Field	Members	Spin	$\mathcal{U}(1)_Y$)	$\mathcal{SU}(2)_L$	$\mathcal{SU}(3)_C$
Leptons	L_i	$(e_{\mathrm{L}}, \nu_{e,\mathrm{L}})$, $(\mu_{\mathrm{L}}, \nu_{\mu,\mathrm{L}})$, $(\tau_{\mathrm{L}}, \nu_{\tau,\mathrm{L}})$	1/2	-1	**2**	**1**
	$e_{\mathrm{R},i}$	e_{R}, μ_{R}, τ_{R}	1/2	-2	**1**	**1**
Quarks	Q_i	$(u_{\mathrm{L}}, d_{\mathrm{L}})$, $(c_{\mathrm{L}}, s_{\mathrm{L}})$, $(t_{\mathrm{L}}, b_{\mathrm{L}})$	1/2	1/3	**2**	**3**
	$u_{\mathrm{R},i}$	u_{R}	1/2	4/3	**1**	**3**
	$d_{\mathrm{R},i}$	d_{R}	1/2	$-2/3$	**1**	**3**
Gauge Fields	B	B	1	0	**1**	**1**
	W	(W_1, W_2, W_3)	1	0	**3**	**1**
	G	G_a, $a \in [1, .., 8]$	1	0	**1**	**8**
Higgs Field	ϕ	(ϕ^+, ϕ^0)	0	1	**2**	**1**

Table 2.1: The particle fields of the SM[8].

The $\mathcal{SU}(3)_C$ symmetry describes strong force interaction, and it only affects the quark gauge field with color charges. The $\mathcal{SU}(2)_L \times \mathcal{U}(1)_Y$ transformation describes the weak-isospin(L) and hypercharge(Y) transformation and is effective on particles gauge field with the weak charge and the weak-hyper charge respectively. The combined effect of the two fields gives the familiar electro-weak force after spontaneous symmetry breaking (SSB). This affects both the quark field and leptonic fields transformations, The mechanism of SSB is given in Section 2.1.3.

A detailed list of the fields and their charges along with their mathematical group and generator can be found in Table 2.1.

2.1.2 The Lagrangian

Observing the symmetries given in the above section, the Lagrangian of the SM is written as the following:

$$\mathcal{L}_{SM} = -\frac{1}{4}\sum_{gauge} F^i_{\mu\nu}F^{i\mu\nu} - \sum_f \overline{f}\gamma^\mu D_\mu f + (D_\mu\phi)^\dagger(D^\mu\phi) - \mu^2\phi^\dagger\phi - \lambda(\phi^\dagger\phi)^2 \tag{2.4}$$

The first term describes the interactions of the gauge fields, where $F^a_{\mu\nu} = \partial_\mu A^a_\nu - \partial_\nu A^a_\mu + g f^{abc} A^b_\mu A^c_\nu$. A_μ represents a gauge field, which could be G the gluon field, B the weak hypercharge field, or W the weak isospin field, g is the gauge coupling parameter, and f^{abc} is the structure constants of the gauge group.

The second term describes the kinetic mixing of the fermion particle fields with the gauge fields; f represents the fermion matter field, which includes the quarks and the leptons. The gauge covariant derivative D_μ is a short form, where $D_\mu = \partial_\mu - ig_1\frac{Y}{2}B_\mu - ig_2\frac{\tau^i}{2}W^i_\mu - ig_3\frac{\lambda^a}{2}G^a_\mu$. Here, g_1, g_2 and g_3 is the gauge coupling constants. Y, τ^i and λ^a terms are the respective generators of the $\mathcal{U}(1)_Y$, $\mathcal{SU}(2)_L$ and $\mathcal{SU}(3)_C$ gauge groups.

The last three terms concerns the Higgs potential. They are discussed in detail in Section 2.1.3.

2.1.3 Electroweak Symmetry Breaking

The SM Lagrangian as presented in the last section does not include mass terms. This is inconsistent with observations from experiment[1] The mass problem is solved by the addition of a spin 0 Higgs field [10]. SM particles gain mass through the "spontaneous symmetry breaking" (SSB) of the $\mathcal{SU}(2)_L \times \mathcal{U}(1)_Y$ symmetry. This happen at the electron weak scale. After EWSB, the $\mathcal{SU}(2)_L \times \mathcal{U}(1)_Y$ is broken into the $Uone_{em}$ symmetry. In the following, a condensed derivation of the SSB is described [9].

SSB is consequential to the shape of the Higgs potential of the SM. It can be shown that the Higgs potential is given as the following:

$$V(\phi) = -\lambda_I\phi^2 - \lambda_{II}\phi^4 \tag{2.5}$$

where ϕ is the Higgs potential and λ_I and λ_{II} are parameters.

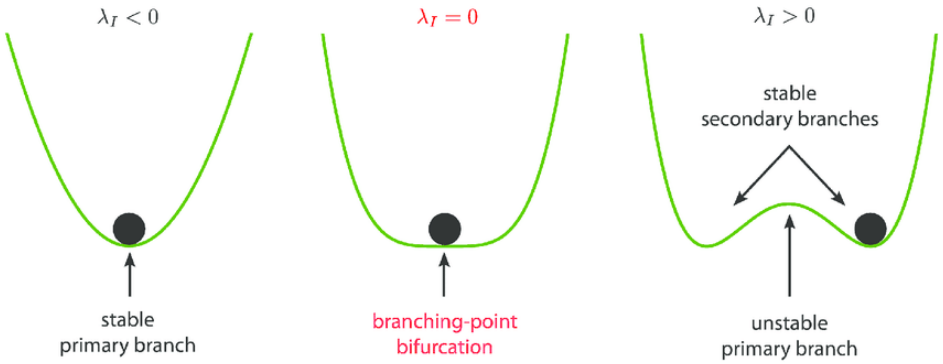

Figure 2.1: A schematic diagram of the Higgs potential [11].

When λ_1 and λ_2 both take on a negative value, the potential, though symmetric, has a minimum value not found at 0. The minimal value is found instead at ν. At this minimum point of the

[1] It can be shown that adding ad-hoc mass terms for these particle fields breaks the internal symmetries and is not permitted by the theory [9].

potential, the vacuum expectation value is:

$$\phi_0 = \frac{1}{\sqrt{2}} \begin{pmatrix} 0 \\ \nu \end{pmatrix} \tag{2.6}$$

While the overall potential is still symmetric, the particle is no longer at a symmetric equilibrium. The symmetry is "spontaneously broken".

It is shown in [9] that mass can be obtained when a gauge transformation is performed on the vacuum expectation value:

$$\phi_0 = \frac{1}{\sqrt{2}} \begin{pmatrix} 0 \\ \nu + h(x) \end{pmatrix} \tag{2.7}$$

where h(x) is the perturbation of the field along the x direction.

This leads to the $D_\mu \phi$ in the third to last term 2.4 to take the following form:

$$D_\mu \phi = (\partial_\mu - igW_\mu^a \tau^a - i\frac{1}{2} g' B_\mu)\phi \tag{2.8}$$

where W and B are weak isospin and weak hypercharge gauge fields defined as above, with g and g' are their corresponding coupling constants.

Plugging this back into the Lagrangian in Equation 2.4, the change in the Lagrangian will become:

$$\Delta\mathcal{L} = \frac{1}{2}\frac{\nu^2}{4}[g^2(W_\mu^1)^2 + g^2(W_\mu^2)^2 + (-gW_\mu^3 + g' B_\mu)^2] \tag{2.9}$$

With the following substitutions:

$$W_\mu^\pm = \frac{1}{\sqrt{2}}(W_\mu^1 \mp iW_\mu^2) \tag{2.10}$$

$$Z_\mu^0 = \frac{1}{\sqrt{g^2 + g'^2}}(g' W_\mu^3 + gB_\mu) \tag{2.11}$$

$$\gamma_\mu = \frac{1}{\sqrt{g^2 + g'^2}}(g' A_\mu^3 + g B_\mu) \tag{2.12}$$

where $W_\mu^\pm$ is the field of the $W^\pm$ bosons, Z is the Z boson field and γ is the photon field.

It can be shown that the mass of the $W^\pm$ and Z_0 boson are [9]:

$$m_W = g\frac{\nu}{2} \tag{2.13}$$

$$m_Z = \sqrt{g^2 + g'^2}\frac{\nu}{2} \tag{2.14}$$

The vector field of the photon remains massless [9]:

$$m_\gamma = 0 \tag{2.15}$$

This mass gaining process follows from the Goldstone's Theorem [12]. It states that for each broken continuous symmetry, a massless scalar boson will appear. After SSB, the $W^\pm$ and Z field acquire mass by "eating" the degree of freedom from the Goldstone boson. These other bosons thereby acquired mass.

As a consequence, after SSB, the weak isospin and hyper-weak forces $\mathcal{SU}(2)_L \times \mathcal{U}(1)_Y$ become $\mathcal{U}(1)_{EM}$. The familiar electric charge can be shown as a combination the weak and hyperweak coupling:

$$e = \frac{g g'}{\sqrt{g^2 + g'^2}} \tag{2.16}$$

Here, e is the electric charge, and g and g' are the weak isospin and weak hypercharge couplings.

The electric charge quantum number can be written as:

$$Q = T_3 + \frac{1}{2}Y_W \tag{2.17}$$

where Q is the electric charge, T_3 is the third component in the weak isospin from $\mathcal{SU}(2)_L$ and Y_W is the hypercharge quantum number from the $\mathcal{U}(1)_Y$ symmetry.

Table 2.2: The table shows the particle fields of the SM after SSB. Coupling and mass parameters are provided.

	Physical Field	Q	Coupling	Mass [GeV]
Quarks	u, c, t	$2/3$	$(y_i =)\ 1 \times 10^{-5}$, 7×10^{-3}, 1	2×10^{-3}, 1.27, 173
	d, s, b	$-1/3$	$(y_i =)\ 3 \times 10^{-5}$, 5×10^{-4}, 0.02	4×10^{-4}, 0.10, 4.18
Leptons	e, μ, τ	-1	$(y_i =)\ 3 \times 10^{-7}$, 6×10^{-4}, 0.01	5×10^{-4}, 0.106, 1.777
	ν_e, ν_μ, ν_τ	0	–	–
Bosons	γ	0	$\alpha_{\mathrm{EM}} \simeq 1/137$	0
	Z	0	$\sin\theta_W \simeq 0.5$	91.2
	(W^+, W^-)	$(+1, -1)$	$\mathcal{V}_{\mathrm{CKM}}$	80.4
	G	0	$\alpha_s \simeq 0.1$	0
Higgs	h	0	λ, μ	125.09

The particle fields and their measured properties after spontaneous symmetry breaking are given in Table 2.2.

Mass terms the SM particles are recovered after SSB. The complete SM contains seventeen particles along with their anti-particle counterparts. There are two types of particles, the bosons, and the fermions: The bosons are particles that have integer spin and are the force mediator particles, this include photon, $W^{\pm}$, Z boson, the gluons and the Higgs boson; The fermions are particles that have half spins. They include the quark and leptons, which are each divided into three generations. Their experimentally measured values can be found in Figure 2.2 and Table 2.2.

2.2 Unresolved Problems in the Standard Model

The SM in its current form has many standing unresolved problems, and so a more complete theory is out there to be discovered. These proposed extensions to the SM are called Beyond-the-Standard-Model (BSM) theories. The unresolved problems and testing the BSM solutions are the main motivators to many studies done in the particle physics community. In this section, a list of major known existing problems of the SM is summarized.

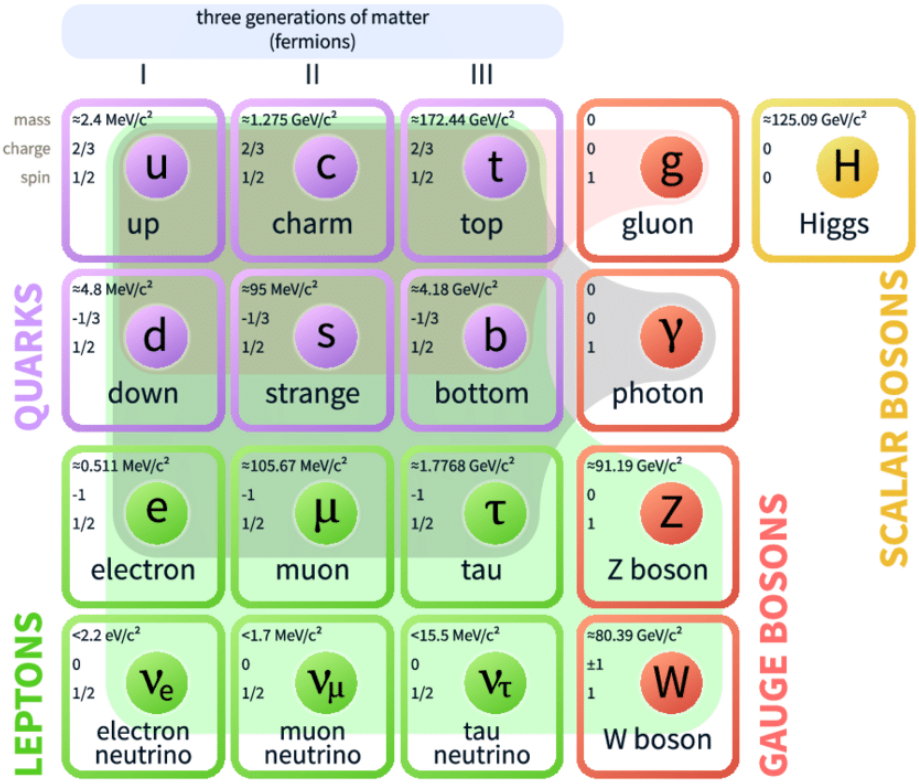

Figure 2.2: A schematic diagram of SM particles seen in the scale of the experiment of the Large Hadron Collider [13].

2.2.1 Gravity

The Standard Model does not include gravity, a fundamental force. Many attempts to reconcile gravity with the existing SM has been made, but it has proven to be challenging. More details can be found in [14].

2.2.2 Naturalness

Naturalness is the property in physics theory where the dimensionless ratio between the free parameters and the physical constants should be of order 1. When a physical theory has a parameter ratio that takes either a very large or small value outside the order of 1, they are considered "unnatural" and unlikely to be fundamental physics quantities. The Standard Model shows many naturalness issues in different dimensions: in the 0th dimension, there is a cosmological constant problem; in the 2nd order, there is the Higgs Hierarchy problem; lastly, in the fourth dimension, there is the strong CP problem. A detailed description of the problems is laid out in the following.

The Cosmological Constant Problem

The Standard Model allows for a 0th dimension constant in its Lagrangian that would not break any of its symmetries. The constant would represent the vacuum energy density and would account for the quantum fluctuation in vacuum. Under Zelokoch's calculations [15], the relations between the vacuum energy density and the cosmological constant of the Einstein's Equation are directly proportional as such:

$$\rho_{vac}c^2 = \Lambda c^4/8\pi G \tag{2.18}$$

Here, ρ_{vac} is the intrinsic density of the vacuum, Λ is the cosmological constant, G is the gravitational constant and c is the speed of light.

The cosmological constant is a well-measured value in cosmology from the measurement of the expansion of the universe. The cutting off in either the Planck scale, a fundamental scale predicted by quantum mechanics or the electro-weak scale in quantum field theory gives a theoretical prediction value of the vacuum expectation value. However, these values do not match. The experimentally measured value of $\rho_{vac} = 5.96 \times 10^{-27} kg/m^3$ [16] is about 40-100 order of magnitude smaller than the natural theoretical scale. This discrepancy poses the biggest naturalness issue in the Standard Model.

The Higgs Hierarchy Problem

The Higgs Hierarchy problem describes the apparent large discrepancy in the order of magnitude between the electroweak scale and the gravitational scale, the weak force is about 10^{24} greater than gravity. Its effect can be seen in the Higgs boson mass is 17 orders smaller than would be expected by the Planck scale. A popular solution is quantum corrections via supersymmetry [17], but as more phasespace for supersymmetry is being ruled out, this solution is increasingly unlikely to solve the problem and is left to be explored by physicists.

The Strong CP Problem

The Standard Model allows for a 4-th dimension term that describes strong Charge-Parity(CP) violation naturally:

$$\mathcal{L}_{QCD} \supset \theta_{QCD}\epsilon_{\mu\nu\rho\sigma}\mathcal{G}^{\mu\nu}\mathcal{G}^{\rho\sigma} \tag{2.19}$$

Here, $\mathcal{L}_{QCD}$ is the Lagrangian term of the QCD, θ_{QCD} is the parameter that describes CP violation, $\epsilon_{\mu\nu\rho\sigma}$ is the structure constant. $G^{\mu\nu}G^{\rho\sigma}$ is the strong gauge field.

Experimentally, strong CP violation is not observed: the neutron electric-dipole moment, which is the quantity that measures the positive and negative charge distribution within a neutron, is found to be exceptionally small [18]. As a consequence of the experimental result, the free parameter θ_{QCD} in Equation 2.19 is believed to be either exceptionally small or zero. Since, there would be no need for such a term in the theory if the parameters are exceptionally small, the term's existence in the Lagrangian is therefore seen as "unnatural". This is known as the strong CP problem. One well-known solution to the problem is the introduction of the Peccei-Quinn symmetry [19]. Under this solution, the new field will create a term that naturally cancels with the strong CP term. A particle named "axion" is predicted by this theory. Many experiments have since been on the lookout for the particle, but it's never yet been observed to date.

2.2.3 Neutrino Mass

The Standard Model does not predict neutrinos to have mass, however, this contradicts experimental findings. Neutrino oscillation, the change of neutrino flavor over time or travel distance, is observed in different solar and reactor experiments. Mathematically, this would only be possible if there must be a mixing angle between the mass eigenstates and flavor eigenstates of neutrinos. This forces the mass of neutrino to be non-zero, contradicting the SM.

Minimally, a minor extension to the SM is required for neutrino mass to be possible in the SM. This is known as the ν-SM theory. Currently, there are two leading camps of ν-SM: the former camp treats neutrinos as a Dirac field, much like other leptons in the SM; the latter predicts neutrinos as a Majorana field, where the anti-neutrinos and the neutrinos is the same particle. Further experiments are required to discover the nature of neutrinos mass.

2.2.4 Matter-Antimatter Asymmetry

The Cabibbo-Kobayashi-Maskawa(CKM) matrix of the SM, which descibes how quarks of different types transform from one type to another, allows for some matter-anti matter asymmetry. However, the measured value of the parameter in the SM is not large enough to account for its observed value in the universe. Prediction of matter over antimatter is necessary to account for the observed universe, which includes the formation of galactic structures, stars, and planets. BSM physics will be necessary to account for the asymmetry.

2.2.5 Flavor Problem

Not all flavors of quarks and leptons are created equal: the mass hierarchy of the quarks and leptons are questions not answered by the SM.

2.2.6 Dark Matter and Dark Energy

SM only accounts for ordinary matter in the universe, which takes up only 4.9% according to findings from the angular spectroscopy of the cosmic microwave background analysis. It is estimated that dark matter makes about five times as much as ordinary SM particles. However, they are not accounted for in the SM. Neither is Dark energy, which is estimated to take up 68.3% of the known content of the universe. Figure 2.3 shows a pie chart that demonstrates the mass-energy distribution of the universe. More details on the diagram and the proposed solution to dark matter in particle form are covered in Chapter 3.

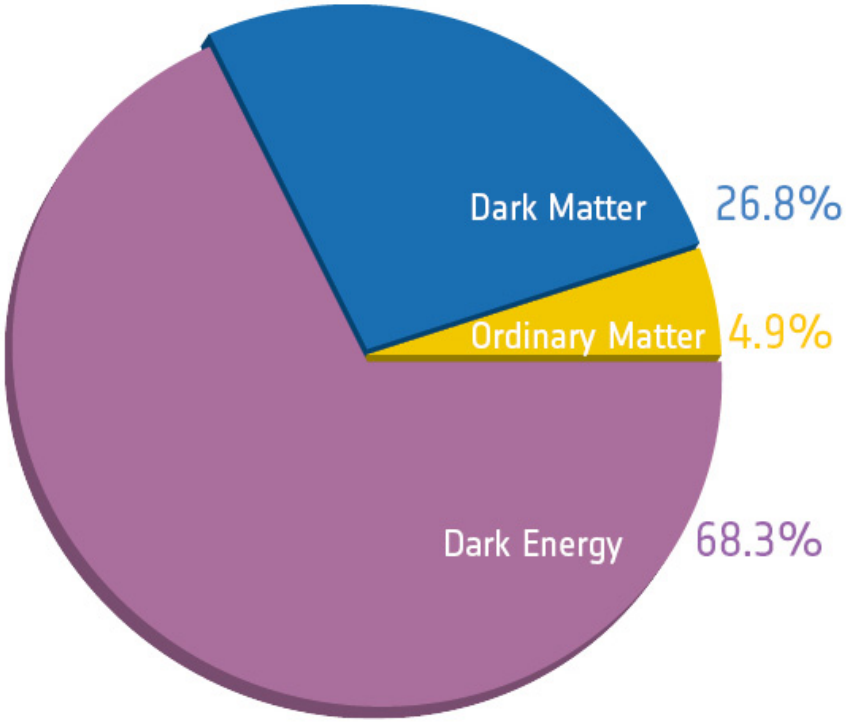

Figure 2.3: The energy distribution of ordinary matter from SM, dark matter and dark energy given from Planck observational data. [20].

2.3 Summary

The SM has led to many breakthroughs in understanding of matter at the fundamental level. Precise measurements of all of the eighteen free SM model parameters 2.2 are made in different experiments. With the discovery of the Higgs boson in 2012, all the particles predicted by the model are found. However, there remains many open questions left to be solved. These all hints at the existence of a more complete theory beyond what is known. In the next chapter, the SM extension on dark matter will be discussed in detail.

Chapter 3

Theory of Dark Matter

One does not become enlightened by imagining figures of light, but by making the darkness conscious.

–Carl Jung

Dark Matter is one of the most solid pieces of evidence for Beyond-the-Standard-Model physics. In 1933, Fritz Zwicky first conceptualized the existence of a dunkle Materie ("Dark Matter") holding the galaxies to the cluster center and thus preventing them from flying apart [21]. The proposition was later concurred by different findings by Horace W. Babcock [22] and Jan Oort [23], among many others.

It is estimated that Dark Matter makes up about 25% of the existing matter-energy composition of the universe, about 5 times more than ordinary matter(See Figure 2.3). It plays a major role in astrophysical object formation and the evolution of the universe.

Dark Matter is known for interacting gravitationally and at most weakly (though recent evidence has shown weak scale interaction to be unlikely [24]). It does not interact electromagnetically or strongly. As various cosmological surveys and astrophysics analyses has revealed more Dark Matter properties, it does not match that of any SM particle. Its creation, composition and interaction mechanisms are not yet understood.

Different theoretical candidates have since been proposed for Dark Matter, which includes primordial blackholes, massive compact halo objects(MACHOs), and weakly interactng massive particles(WIMPs) to name a few. A popular theory proposes that Dark Matter is made up of particles, just like ordinary matter. Under this hypothesis, Dark Matter would be a different kind of particle(s) that is governed by physics in the "dark sector" not yet included in the Standard Model.

Many experiments use different ways to search for Dark Matter particles. Experiments range from satellite telescopes that hunts for photon excess from possible Dark Matter interactions, to Earth target experiments that attempt to capture Dark Matter that travels through the planet. Experiments that seek to further understand the nature of Dark Matter also include the Large Hadron Collider: the machine features many experiments that seeks to produce Dark Matter through extreme high energy intensity collisions of subatomic particles. This thesis will feature two different analyses that seek to find Dark Matter with this method.

In this chapter, evidence for Dark Matter is reviewed in Section 3.1, Dark Matter and the current properties that restrict its nature will be covered in Section 3.2, and Section 3.3 reviews possible Dark Matter candidates. An overview of search methods for Dark Matter as a particle is covered in Section 3.4; highlights of the theoretical modeling approach used by the LHC of Dark Matter are discussed in Section 3.5. Lastly, LHC Dark Matter search signatures are discussed in Section 3.6.

3.1 Evidence

The evidence for dark matter include galactic rotational curvees, gravitational lensing and cosmic microwave background.

3.1.1 Galactic Rotational Curve

The first proposition of Dark Matter was in the 1930s by Fritz Zwicky based on observation of the Coma cluster. It was later confirmed by further systematic galaxy rotational curve studies by Vera Rubin, Kent Ford [25] and Ken Freeman [26].

Most of the studies can be interpreted following Zwicky's original argument: galactic clusters and galaxies are treated as stable systems of discrete particles at astrophysical scale. They are therefore governed by the Virial Theorem:

$$\langle T \rangle = -\frac{1}{2} \sum_{k=1}^{N} \langle F_k \cdot r_k \rangle \tag{3.1}$$

Here T represents kinetic energy, F is the force that holds the particles in the system together, and r is the distance between the particles, and N is the total number of particles in the system.

The Virial Theorem states that there is a direct correlation between the kinetic energy and potential energy in a particle system. In other words, there is a correlation between the velocity of the object

(through kinetic energy) and the mass (through gravitational force) of the system. The correlation is as the following:

$$v(r) \propto \frac{M(r)}{\sqrt{r}} \tag{3.2}$$

where v is the velocity, r is the distance from the center of the system and M(r) is the mass of the galaxy enclosed by a sphere with a radius of r.

In these observational studies, the striking finding was that the velocity distribution for many of these clusters and galaxies do not follow the prediction from the Virial Theorem: the velocity curves of the galaxies do not follow the expected $\frac{1}{\sqrt{r}}$ distribution, instead, they are close to constant to r, especailly in the outer rings. Figure 3.1 shows the difference between the theoretical prediction and the observation.

Since the galactic rotational curves studies are performed on the luminous objects that can be observed through light, which means invisible matter could just not be accounted for. One proposed solution to the problem is to add a halo of non-luminous Dark Matter to these galaxies. The additional mass would then make the galactic rotational curves match the Virial Theorem prediction. As the result is found across many galaxies studied, galactical rotational curves are seen as major evidence for the existence of Dark Matter.

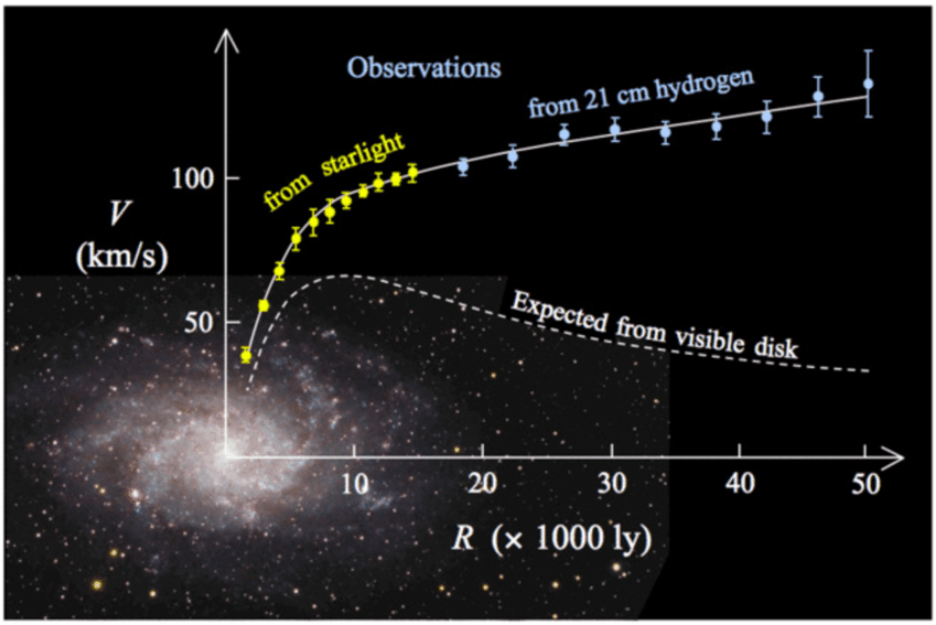

Figure 3.1: The galactic rotational curve of M33. The expected rotational curve is shown in the dotted line. Experimental data is shown in yellow and in blue [27].

3.1.2 Gravitational Lensing

General relativity verdicts that massive objects bend space-time around them. The details are captured elegantly in the Einstein's Equation 3.3.

$$R_{\mu\nu} - \frac{1}{2}R\, g_{\mu\nu} + \Lambda g_{\mu\nu} = 8\pi\frac{G}{c^4}T_{\mu\nu}, \tag{3.3}$$

In this equation, $R_{\mu\nu}$ is the Ricci curvature tensor, R is the scalar curvature. Together, they form the Einstein tensor. $g_{\mu\nu}$ is the metric tensor, and $T_{\mu\nu}$ is the stress-energy tensor. This equation states that the curvature of space-time is directly related to the mass and energy in that space.

Consequently, light rays that travel through the curved space-time around the massive object are therefore "bent". The effect is analogous to the effect of angled lenses bending light rays due to a velocity difference across different media, and is called "gravitational lensing".

There are different forms of this lensing effect: "Strong lensing" happens when bending of light result in either multiple images. Or, as a light ring or light arcs observed around massive centers of galaxy clusters and galaxies; "Weak lensing" usually involves weaker spatial distortion effects over many objects in a region; micro-lensing is when the effect is only an apparent change in the brightness of the source.

Dark Matter's existence is evident from gravitational lensing studies. An example of strong lensing that demonstrates existence of Dark Matter is shown in Figure 3.2 in the bullet cluster collision of 1E 0657-56 [28]. The image is produced from the combination of gravitational lensing and x-ray telescope imaging. The red part of the diagram denotes ordinary matter and the blue part represents Dark Matter. In the cluster collision, ordinary matter bend light around them and became luminous from the collision, captured by x-ray imaging; The blue part shows a part of the cluster that did not interact luminously and was only inferred through gravitational lensing. This is a strong evidence for the existence of non-luminous matter in the clusters. The observation also constrains the self-interaction of Dark Matter.

Weak lensing results of galaxies distribution over a large area has provided further evidence and constrained the for density and distribution of Dark Matter in the universe [29].

3.1.3 Cosmic Microwave Background

In the beginning of the universe, ordinary matter and Dark Matter existed in a hot plasma soup with frequent interaction between charged particles and photons. As the universe continued to

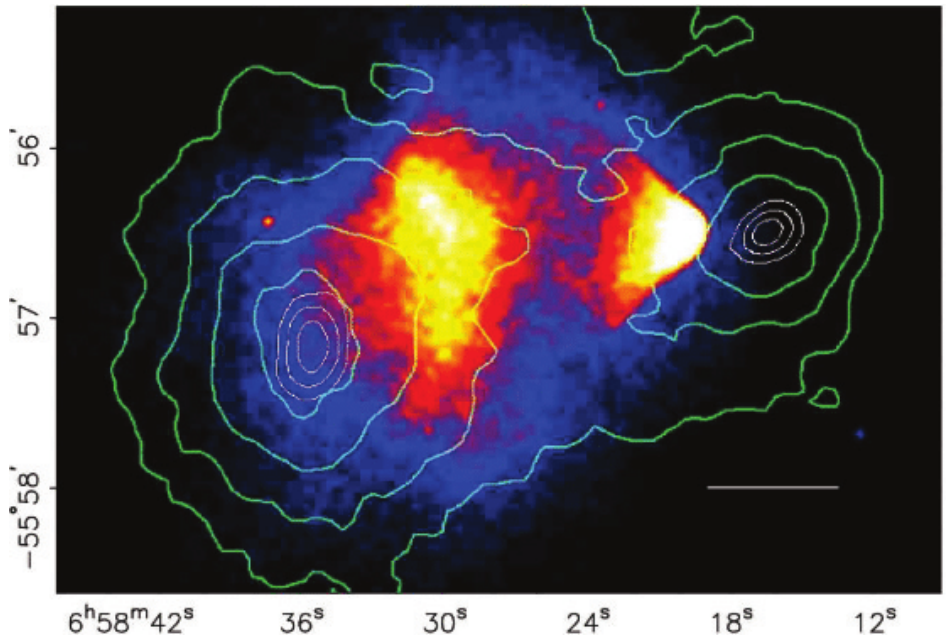

Figure 3.2: Bullet cluster (1E 0657-56) showing two colliding galaxy clusters, the part in red came from x-ray image by Chandra, highlighting normal matter distribution; the part in blue came from gravitational lensing [28].

expand, during a period called "recombination", the expansion of the universe had cooled the plasma soup enough that charged particles began to form neutral atoms. Photons do not scatter on the neutral atoms, and thus propagate to the other end of the universe. Due to red shifting, they form a microwave background of the universe that can still be observed today. This is the Comic Microwave Background (CMB). The CMB is very uniform, but there are still small temperature variations. Figure 3.3 display the CMB along with its temperature variations [30]. The variations came from primordial acoustic oscillation that came from the interaction of Dark Matter and ordinary matter with photons in the original plasma. It can be decomposed into an angular power spectrum.

Due to the different interaction rate between Dark Matter and ordinary matter with photons and each other, different Dark Matter and ordinary matter make-up of the universe would result in different angular spectroscopy shapes, the angular spectroscopy data can be fitted to find the composition of the universe. Figure 3.3 shows a fitted angular spectroscopy. From the result, it was found that Dark Matter is not only an essential part of the universe, its composition is approximately 5 times as large as ordinary matter.

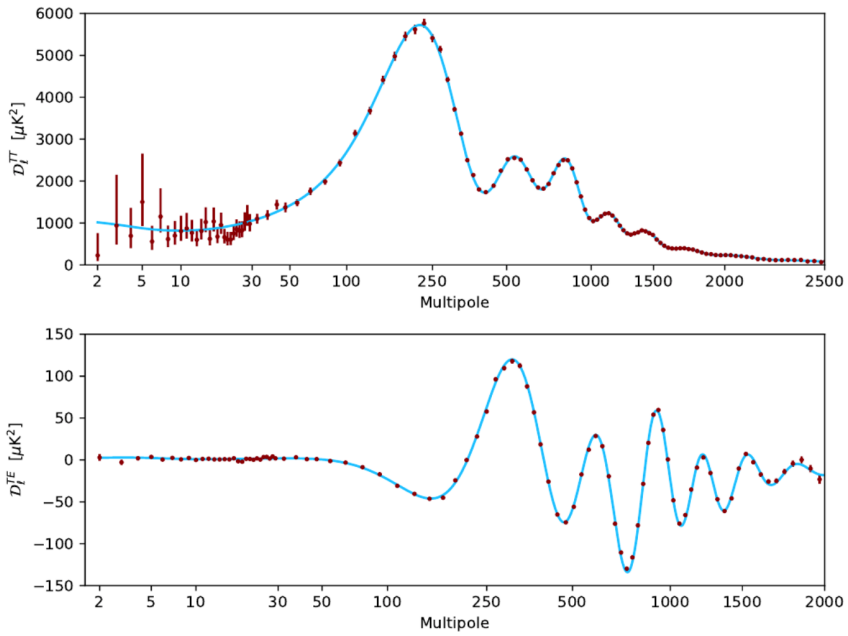

Figure 3.3: The Cosmic Microwave Background power spectrum measured by Planck [31].

3.2 Properties of Dark Matter

While Dark Matter itself has never been directly observed, many studies in the cosmological, astrophysical and particle scales have constrained many of its properties. In this section throughout this thesis, the following properties of Dark Matter will be discussed and justified.

3.2.1 Dark

Dark Matter got its name from its little to no interaction with light, compared to ordinary matter. Collision of the bullet cluster has also greatly constrained its interaction with itself It is taken that it will not interact with collider detectors. Its interaction with ordinary matter would be rare in the energy scale of the LHC.

3.2.2 Long Life Time

As Dark Matter is seen today in evidence across different scales (see Section 3.1). It is assumed to have a long life time since the age of the universe. Many theoretical models of Dark Matter require a Z_2 symmetry, such as the R parity of supersymmetry. This prevents Dark Matter particles from decaying into lighter SM objects. In most experimental searches today, it is be treated as something

that does not decay further into other detectable SM particles [32].

3.2.3 Interacts Gravitationally

Current evidence (see section 3.1) suggests that Dark Matter is massive, and thus interacts gravitationally. However, there is no consensus on the mass on the individual constituents of Dark Matter.

3.2.4 Cold

Current theoretical candidates of Dark Matter can be split into two camps: "cold" Dark Matter and "hot" Dark Matter. The former group suggests that Dark Matter is made of objects massive enough, therefore the velocity would be non-relativistic; the latter group suggest the opposite view. The Dark Matter candidates being searched for in the rest of the thesis will be assumed to be cold, as this property allows for its search in the LHC under certain signature. The justification for Dark Matter as a cold particle came analysis of galaxy formation and the process requires Dark Matter to be above a certain mass.

3.2.5 Low Self Interaction

Dark Matter is believed to have little to no self interaction. Mixed X-ray, optical and gravitational lensing studies on the merging galacy cluster 1E-657-65 has restricted its self interaction limit to below $\frac{\sigma}{m} =< 1.25 cm^2 g^{-1}$ (68% confidence) [33].

3.3 Candidates

There exist a wide range of candidates for what Dark Matter could be. Here, a few possible candidates for Dark Matter are outlined.

3.3.1 Sterile Neutrino

The SM does not predict that neutrinos have a mass, but this contradicts with experimental findings and is therefore a problem for the SM. By replacing right-handed neutrinos in the SM with gauge singlet fermions that have no interaction other than mixing with normal neutrinos. Sterile neutrino is formed by theoretical models. On tuning parameters such as its its interaction rate

with normal neutrinos, mass and mixing angle, sterile neutrino can be a possible candidate for Dark Matter, which can lead to a density of Dark Matter with stability consistent with the scale of the universe [34]. They are searched for in radiator experiments such as the Daya Bay [35, 36] and in scintillator experiments like DANSS [37].

3.3.2 Axion

Another existing problem in the SM is the strong CP problem, the problem is described in detail in Section 2.2.2. One natural solution to the problem is to introduce an additional symmetry called the Peccei-Quinn symmetry [38], which would lead to an mediator particle called the axion.

The axion proposed is a Dark Matter candidate, as it shares many properties with the known profile of Dark Matter including an exceptionally long life time. Recent experimental finding from the XENON1T experiment shows anomalies that could be signs of axions [39].

3.3.3 Weakly Interacting Massive Particle (WIMP)

A very attractive candidate for Dark Matter is called the weakly interacting massive particle(WIMP). It appears naturally with many Beyond-the-Standard-Model theories that aim to solve other physics problems, including theories of supersymmetry with R-parity and some extra dimensional theory. In the study of Dark Matter in cosmology, it is frequently assumed to be a thermal relic. Thermal relic Dark Matter is in thermal equilibrium with ordinary matter in the early universe. In thermal equilibrium with ordinary matter, it gets produced and annihilated at the same rate. There comes a point in the universe called "freezing out", where the expansion of the universe cools the particle bath and the temperature becomes lower than the energy required for Dark Matter to be produced given Dark Matter mass. Dark Matter production from ordinary matter thus ceased. As the universe further expands, it becomes more difficult for Dark Matter to find each other annihilated and form ordinary matter. Dark Matter abundance is locked at this point and remain unchanged until today. Figure 3.4 shows a plot that demonstrates how thermal relics work. Using this model and the current measured abundance of Dark Matter in our current universe, the self annihilation cross section of Dark Matter is $\langle \sigma \cdot v \rangle \simeq 3 \cdot 10^{26} cm^3 s^{-1}$. This annihilation cross section scale matches many prediction made in supersymmetry theories. Many Beyond-the-Standard-Model theories, such as SUSY, the Universal Extra Dimension Model, and the little Higgs all predict a particle with known Dark Matter properties and self-interaction rate of the same scale. This is known as the WIMP miracle [40].

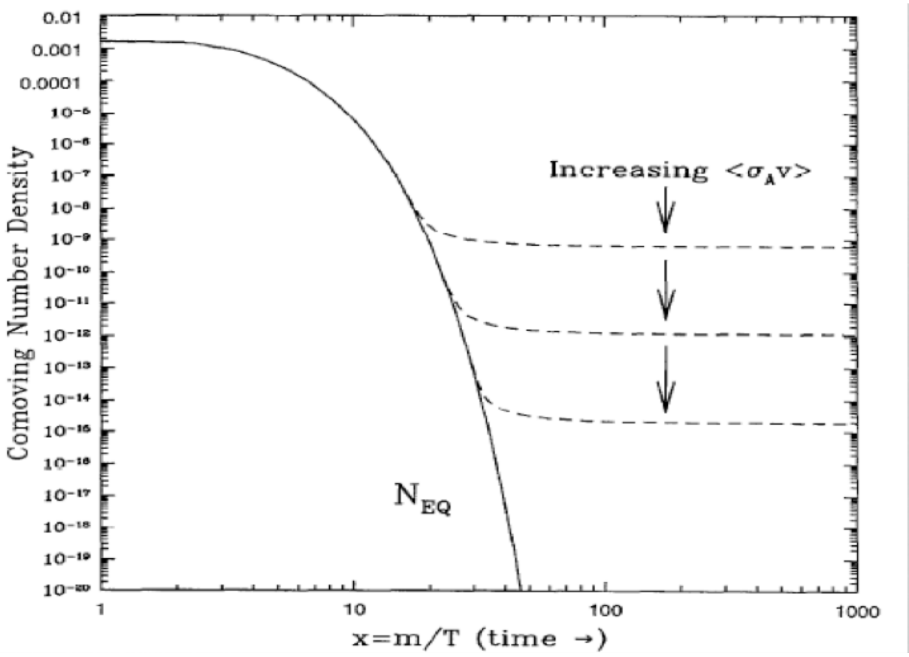

Figure 3.4: Solid line here shows the change in the densitiy of Dark Matter in an expanding unverse. In the early universe, the solid is horizontal, indicating the time when Dark Matter production and annihilation is equal. The line gradually fall with increase of time when production rate began to decrease with the universe expansion. Later as the universe further expands, the annihilation stops as well and Dark Matter gets freezes out to different density level with different assumed self interaction annihilation rates [41].

3.4 Experimental Search Overview

Traditionally the search for Dark Matter is split into different experimental categories sorted by the different detection methods from different Dark Matter/ordinary matter interactions.

3.4.1 Direct Detection

Dark Matter is believed to travel across the universe through the earth. Assuming weak interaction between Dark Matter and SM nucleons, Dark Matter can be detected directly with different target objects.

$$R \propto N\rho\chi\langle\sigma_\chi\rangle \tag{3.4}$$

Here, R is the interaction rate, N is the number of events ρ is the density of the target object, χ is the interaction area for each event decay and σ_χ is the interaction cross section.

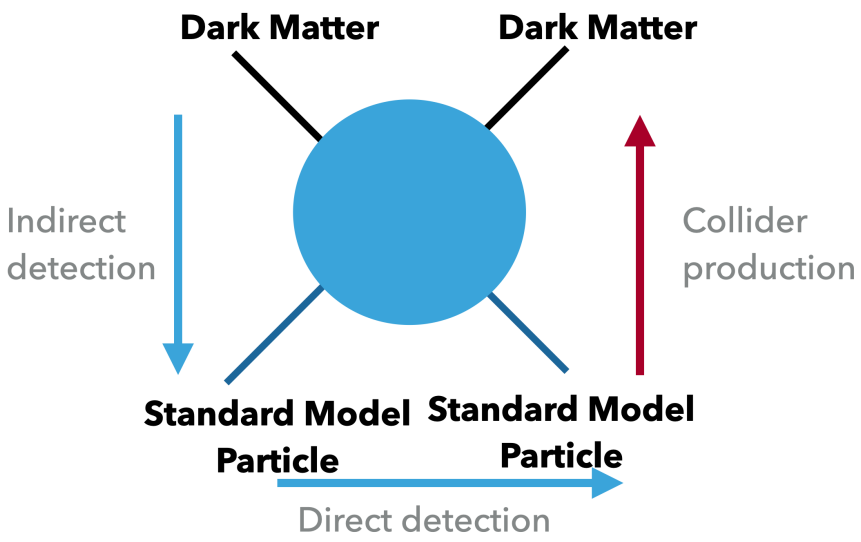

Figure 3.5: Schematic cartoon showing the different Dark Matter detection methods facilitated by different interactions thus signatures.

There are many experiments that use different interaction material and target different Dark Matter masses. Notable experiments include LZ [42], Xenon1T [39], SuperCDMS [43], CRESST [44] and DAMA [45].

As more experiments had excluded much of the theory model phasespace, many of the experiments now face the challenge of the "neutrino floor" in low mass Dark Matter searches, where the neutrino background in cosmic radiation begins to dominate signal regions.

3.4.2 Indirect Detection

Indirect detection looks for SM annihilation products of Dark Matter. It looks for interaction in places where matter is dense enough to interact, usually in center of galaxies and stars. Experiments include FermiLAT [46] and H.E.S.S. [47].

3.4.3 Collider Production

In colliders, Dark Matter can be studied by being directly produced from SM particles. As this will be the method that the rest of the thesis is based on, the theoretical models as well as the experimental signatures of Dark Matter in the LHC will be discussed in detailed in Section 3.5 and Section 3.6.

3.5 Theoretical Models in LHC Searches

While there exist a wide range of speculation on the identity of Dark Matter, LHC as a Dark Matter searching tool can only probe a unique set of Dark Matter candidates.

Different approaches are used to develop benchmark models when searching for Dark Matter at the LHC. The choice of model is a trade-off between simpicity, physics reinterpretability and experimental sensitivity. Sorting by an ascending degree of completeness, this section will review the different approaches and models of Dark Matter used at the LHC. Figure 3.6 shows the theoretical models used in the LHC sorting from its level of completeness.

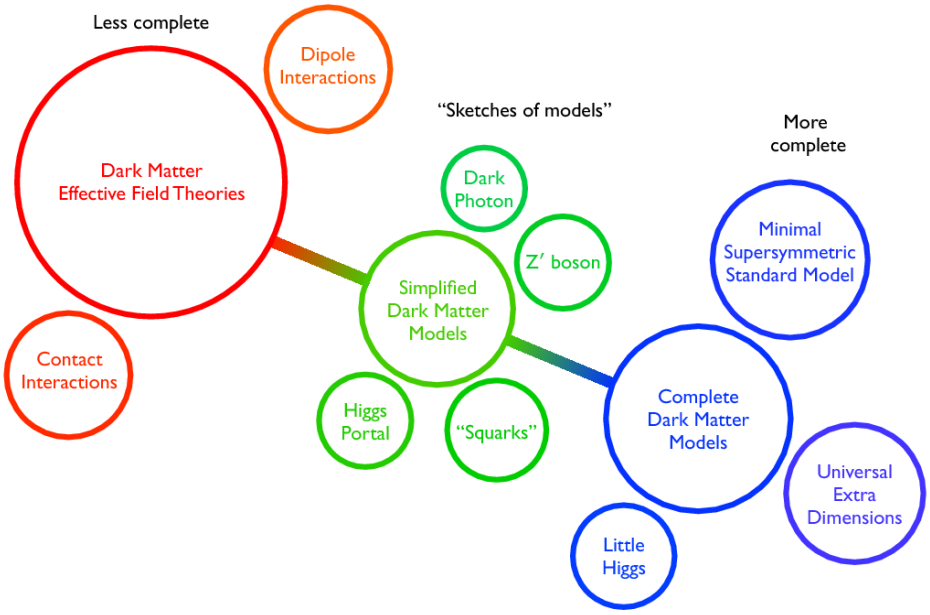

Figure 3.6: Colored Scheme showing Dark Matter modeling approach from more simplistic (left) to more complete models (right) [48].

3.5.1 Simple Portal Models

The simplest kind of models are simple extensions to the SM. In these models, Dark Matter is mediated either through the Higgs or the Z Boson. As the Z portal models are constrained by LEP and DD experiments (LUX, PandaX-II), Dark Matter that are mediated through a heavier version of Z boson (the $Z\prime$) and additional scalar are also searched for and are sometimes regarded as the simple portal models.

3.5.2 Effective Field Theory

The effective field theory (EFT) approach condenses a wide range of complete models their simplified versions by focusing on what is experimentally accessible. High mass mediator particles in complete theories act as a contact operator. High energy correction and details are integrated out for "effectiveness". All kinematically accessible observables are described by a Lorentz structure and a rate parameter.

This approach allow for measured experimental values to be directly converted to theory parameters. A wide range of complete models can be probed with a few clear experimental model search. However, the model has a singularity and is not valid for when the interaction momentum transfer is close to that of the mediator mass. In the LHC, Monte Carlo(MC) event generation, which is the standard computer simulation of collision events that are used to aid studies, a truncation method is used to bound the simulated Monte Carlo events below this singularity limit [49].

3.5.3 Simplified Model

The singularity problem in EFT can be resolved with a simplified model approach. In simplified model, the contact interaction in EFT is turned into mediator particle s-channel/t-channel exchanges. With the price of an increased number of parameters, simplified models can provide the full mechanics of a particle interaction with the additional details.

Simplified models of Dark Matter at the LHC do not break the global and gauge symmetries of SM, the Lagrangian terms are Lorentz invariant and predict at least a Dark Matter candidate that fullfills the properties requirements in the previous section.

Some simplified Dark Matter model used in the LHC include the Two-Higgs Doublet Model (2HDM) [50], where Higgs or a non-SM exotic Higgs could serve as a mediator to Dark Matter; as well as dark photon or kinetically mixed Z' Dark Matter models.

Other than these, simplified model in supersymmetry such as the Phenomenological Minimal Supersymmetric SM (pMSSM) [51], which reduces the over 100 parameters of the complete Minimal Supersymmetric SM to 19 parameters, predicts a natural Dark Matter candidate, neutralino.

In addition, other gauge or gravity mediated SUSY theory predicts the gravitino as a Dark Matter candidate.

3.5.4 Less-simplified models

Simplified models are able to capture common features in many Dark Matter models, but it neglects features from other models. As the LHC work towards expanding its search signatures, the less-simiplified models are becoming more popular. These include non-minimally flavor violating models, coannihilation models that include two or more kinds of Dark Matter particles, as well as multiple Higgs models where the additional exotic Higgs serves as a mediator between SM particles and Dark Matter. The signatures for these models are captured in Figure 3.7.

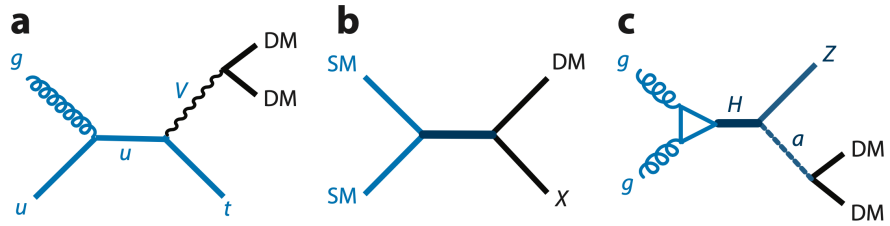

Figure 3.7: Figure here shows the signature for the less-simplified models which include the non-minimally flavor violating monotop signature, a possible signature from the coannihilation model, as well as an exotic Higgs signature [52].

A detailed list of models used at the LHC by both CMS and ATLAS can be found in [53].

3.5.5 The LHC Dark Matter Benchmark

The Dark Matter benchmark from the LHC uses the EFT approach (described in Section 3.5.2). It encompasses a wide range of Dark Matter models with its signature.

In the Dark Matter benchmark of the LHC, the SM is extented by an additional U(1) symmetry: it is assumed that Dark Matter along with some Stanard Model particles are all charged under this. A new gauge boson can thereby facilitate interaction between the SM and Dark Matter field.

The Dark Matter mediator can either be an axial vector or a vector. The corresponding lagrangians are:

$$\mathcal{L}_{vector} = g_q \sum_{q=u,d,s,c,b,t} Z'_\mu \bar{q}\gamma^\mu q + g_\chi Z'_\mu \bar{\chi}\gamma^\mu \chi \tag{3.5}$$

$$\mathcal{L}_{axialvector} = g_q \sum_{q=u,d,s,c,b,t} Z'_\mu \bar{q}\gamma^\mu \gamma^5 q + g_\chi Z'_\mu \bar{\chi}\gamma^\mu \gamma^5 \chi \tag{3.6}$$

Here, $\mathcal{L}_{vector}$ and $\mathcal{L}_{axialvector}$ represent the Lagrangian for the Dark Matter interaction, $Z\prime$ represents the field for the Dark Matter mediator; g_χ is the interaction strength, γ are the dirac matrices and q are the different quark fields[1].

Under this calculation the minimal parameters of the model is reduced to $g_q, g_\chi, m_\chi, M_{med}$. Similar argument can be made for lepton decays where the quark decays are replaced by leptons.

3.6 Experimental Signature in the LHC

This section review some common signatures of dark matter that are being searched for at the LHC.

3.6.1 Mono-X signature

This describes the type of Dark Matter search where an invisible Dark Matter particle is produced directly at the LHC and is "observed" in the detector as missing transverse momentum. Dark Matter is known to interact only very weakly with normal matter, and thus is assumed to not leave a trace in the LHC detector. When events are produced through proton-proton collision along the z-axis in the LHC, the momentum of all objects along the transverse plane to the z-axis is always zero. Therefore, when an event has missing transverse momentum recoiling against another visible object, the signature could possibly be Dark Matter. This class of analysis is named by the SM object that Dark Matter recoils against. Mono-jet, mono-Higgs, mono-Z are a few analyses done this way.

3.6.2 Di-object Signature

Dark Matter can also be searched for without the production of the Dark Matter particle. The simplified models that predicts Dark Matter in the mono-X analyses predicts effective mediator particle between SM particle with Dark Matter. These effective mediator particles can be directly searched for through via decay back into SM objects. As the process is distinct from any known SM particle processes, an excess of events beyond the known Standard Model prediction could be indicative of Dark Matter in the LHC. These di-object search include dijet, dilepton, diphoton searches. In recent years, new techniques such as the trigger-level-analysis and channels that have an additional initial state radiation objects are being pioneered. These result in a search phasespace much greater than the traditional program and greatly extended the of the richness of the LHC

[1] u, d, s, c, b, t represents up, down, strange, charm, bottom and top

serach program.

3.6.3 Supersymmetry Invisible Particles

There are a few natural candidate in SUSY that could match the profile of Dark Matter being searched for, they show up in detector signatures as missing transverse momentum. Many searches in SUSY that aims for missing tranverse momentum has more complicated decay chains with multiple particles compared to the signature presented in Section 3.6.1 So far, no searches on SUSY has found anything statistically significant, but the increased data size has led to new exploration in the electrowino phasespace.

3.6.4 Search for Long-Lived Particles

The LHC is also looking for a new set of decay channels as well as missing transverse momentum dark matter signatures through Long-Lived particles searches. These signatures are predicted by extensions to SUSY models [54]. Long-Lived particles can decay inside the tracking detector, or calorimeters and sometimes even outside of the main detectors. The observation of these particles are somtimes challenging due to the required dedicated triggers and specified reconstruction algorithms.

Chapter 4

The Large Hadron Collider And the ATLAS Detector

> *Please read carefully these precautions about the assembly.. When you finish assembling the product, please place it on a flat surface and make sure it is stable before use. Please also properly fix the anti-topple device, if included, in accordance with the assembly instructions. The product will keep longer by retightening the screws from time to time.*
>
> –IKEA, Assembly Instructions

All data used in this thesis is taken from the ATLAS experiment [55] of the Large Hadron Collider(LHC) [56] in the European Organization of Particle Physics(CERN).

CERN is the largest research organization on particle physics in the world. (See Figure 4.1 for a schematic map) The laboratory was built in the 1950s as a joint European effort to advance particle physics. It includes a total of 23 member states to date. Many major physics discoveries were made at CERN. Most notably, the discovery of the W, the Z boson [57], and the first man-made antihydrogen atom [57]. In 2012, a boson of mass 125 GeV/c^2 was discovered, it is believed that it matches the profile of the long sought after Higgs Boson particle [58], which gives an explanation to the origin of mass of matter in the universe. The site with 2660 on-site personnels and 12,400 users from over 70 countries also produced many technological derivatives outside of scientific discoveries. In particular, the World Wide Web was first built at CERN [59].

This chapter presents the hardware and software apparatus in the LHC at CERN used to collect and produce the datasets for the later analyses. The working and the layout of the LHC, the machine used to accelerate protons and monitor its collisions is presented in Section 4.1; the ATLAS detector, the apparatus used to collect proton-proton collision data is described in Section 4.2. Lastly, the

triggering chain: the hardware and software collecting strategy is presented in Section 4.3.

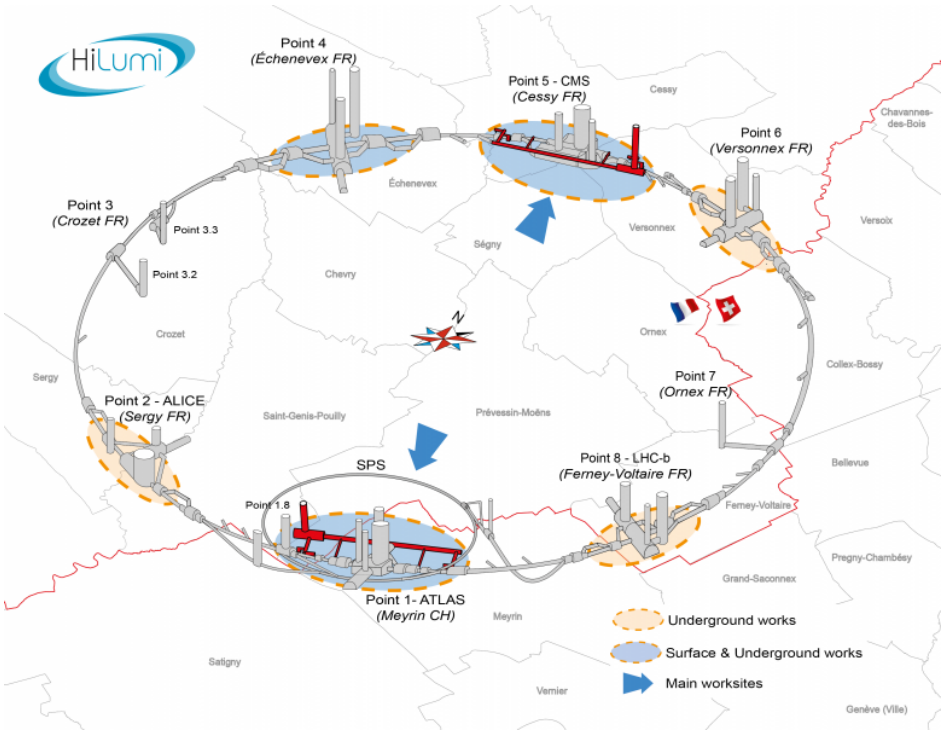

Figure 4.1: This figure shows where the CERN is located geographically, across the border between France and Switzerland [56].

4.1 The Large Hadron Collider

The LHC is located on the France-Switzerland border. Its main ring is a 27 kilometers tunnel that is 175 meters underground. It is mainly used to collide protons. Lead-lead collisions and proton-lead collisions are also done for a few weeks in each data-taking year.

The collider was a planned successor to the Large Electron-Positron (LEP)(209 GeV collision) and the Tevatron collider (up to 1.96TeV) in Fermilab. Since the last two experiments, the community converged on a consensus of an O(10)TeV scale proton collider with the main physics goal to probe electro-weak scale Higgs boson, beyond-the-Standard-Model physics, and further Standard Model measurement studies. The LHC was born.

The LHC reuses the same tunnel as the LEP experiment, with some major modifications were done to the tunnel for the upgrade: to achieve higher center-of-mass energy and to collide proton-proton instead of electron-positron, the angular velocity of the particle colliding would need to be raised. The existing magnet from the LEP experiment was therefore replaced to make way for more

powerful cryogenic-based super-conducting magnets to bend higher speed particles. In addition, as the LHC uses a proton-proton beam rather than an electron position in the LEP, an extra beam pipe was required. This is due to the fact that the proton beams collisions could not share the same beam pipe as the position-electron beams in the LEP. The radio frequency system is also modified in the upgrade to the LHC to allow for acceleration of the two separate beams in the LHC.

After the upgrade, the main ring of the LHC allows for particle collision to happen in four main intersection points. These four points are directly inside the four major experiments of ATLAS [55], CMS [60], LHCb [61] and ALICE [62].

ATLAS and CMS are general-purpose detectors, data collected from these experiments are used for studies including Standard Model measurement, Higgs property measurement as well as exotic and new physics searches. The similar but slightly different detector structure between the two experiment allow for crosschecks and validation of physics results. ALICE is optimized to study strong physics in the quark-gluon plasma generated from lead-lead collisions. LHCb is a forward detector that specializes in b(bottom quark)-physics measurement. Studies on the bottom quark measure the CP violation parameter. It could help better understand matter-antimatter asymmetry of the universe.

In addition to the four major experiments, the LHC currently hosts four more experiments. LHCf looks for forward particles that originate from cosmic radiation [63]. FASER is an experiment in search of long-lived exotic particles with a lifetime beyond the ATLAS detector [64]. MoEDAL, which sits in the cavern of LHCb, looks for the magnetic monopole or highly ionizing stable massive particles (SMP) [65]. TOTEM shares the CMS interaction point; it measures the total cross-section, diffraction process and elastic scattering processes of particles in the proton collisions [66].

The LHC is designed to operate at a maximum center-of-mass energy of 14 TeV. Protons that get collided at the different interaction points go through many stages before collisions.

In the following sections, some technical terms related to LHC operation will be discussed. Different parts of the LHC from proton production, proton acceleration to proton collision in the center of the ATLAS detector is also covered.

4.1.1 Luminosity

The instantaneous luminosity is a measure of the rate of events that can be produced under certain detector conditions. It is directly related to the event rate of different processes under production. The quantity is given as the following:

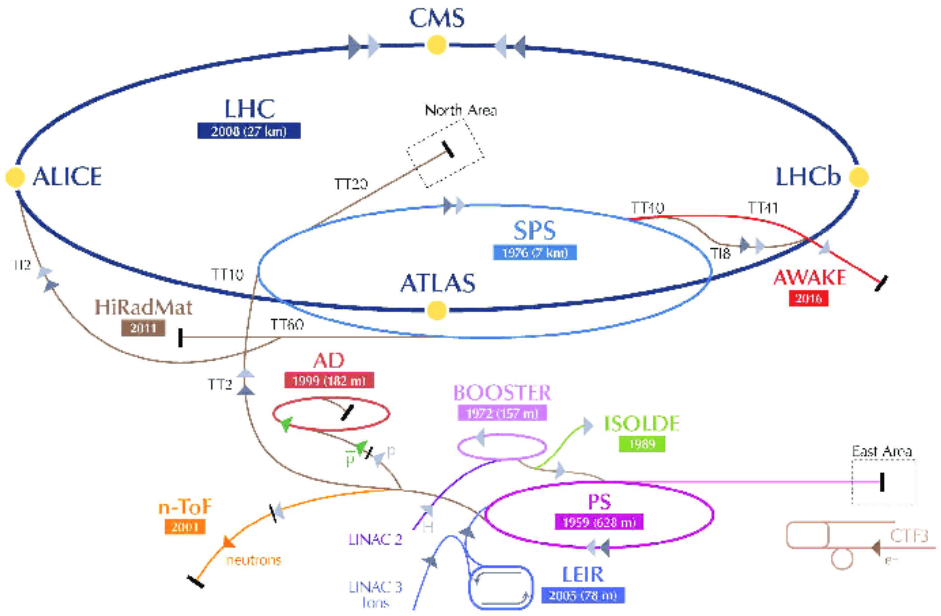

Figure 4.2: This figure shows the accelerator complex of CERN, featuring the experiments and injection chain of the LHC [67].

$$L = \frac{F \cdot N_p^2 n_b f_\lambda}{4\pi\epsilon\beta^*} \tag{4.1}$$

$$\rightarrow = \frac{N_{\text{proton in beam 1}} \cdot N_{\text{proton in beam 2}} \cdot \text{Beam Crossing frequency}}{\text{Beam overlap Area}} \tag{4.2}$$

In the formula above, N_p is the number of proton in each beam, n_b is the number of bunches per beam, f is the frequency of the beam traveling around the collider, and β is the beam cross-sectional size at the injection, ϵ is the beam emittance, F is the beam crossing angle.

The LHC was built to have a peak luminosity at L=$2 \cdot 10^{34} cm^{-2} s^{-1}$, but in most of Run II, it has a nominal value of $10^{34}\text{cm}^{-2}\text{s}^{-1}$.

While the instantaneous luminosity is a measure of LHC performance in operation, integrated luminosity, denoted by $\mathcal{L} = \int L dt$ is a measure of the amount of data taken over time.

While an increase in instantaneous luminosity increases the event rate in the experiment, it also increases the pile-up, which is multiple occurrences of interactions that happened simultaneously as the target events. Pile-up cleaning will therefore become an increasingly important task as the LHC instantaneous luminosity increases.

4.1.2 Proton Production

The protons that collide in the LHC came from hydrogen in gaseous form. The electrons are stripped out through grating by an ion source. Protons formed are grated to make sure they are in the same direction before being sent off to the injection chain for acceleration.

4.1.3 The Injection Chain

The acceleration of protons after their production is done through the injection chain. It mainly consists of a series of pre-acceleration steps through the different linear booster and booster rings. As the speed and energy of the particle are effectively restricted by both the accelerator ring size as well as magnet strength in a cyclotron accelerator, a dedicated series of smaller rings in ascending order in size are used to accelerate the beam to a higher energy level before the LHC ring.

The protons first go through a linear accelerator named LINAC2 to be accelerated to 50 MeV. After the acceleration, they enter a synchrotron ring called the Proton Synchrotron Booster(SPS). In the SPS, the protons are accelerated to 1.4 GeV at this stage. Subsequently, they are injected into the Proton Synchrotron(PS). The PS accelerates the protons further to 26 GeV and is injected into the Super Proton Synchrotron(SPS), the protons are then further accelerated to 450 GEV and passed onto the LHC ring in *proton bunches*.

These booster rings are existing structures from previous collider experiments [55].

4.1.4 The Radio Frequency Cavities

After the injection to the LHC, the protons will be further ramped up in energy. Located in IP4 of the LHC main ring, the radio frequency(RF) cavity of the LHC performs the acceleration of particles in the ring. The cavity oscillates its electric field at a fixed 400MHz rate, which accelerates the incoming well-timed protons. In Run II, protons that arrive in the LHC are accelerated from the 450 GeV injection energy to 6.5 TeV in 10 million loops around the LHC, which takes approximately 20 minutes. Other than accelerating protons, the cavity also modulates the protons' energy: the slowed protons are accelerated and fast one decelerated. They are grouped into proton bunches.

4.1.5 The Beam Dump

The beam dump of the LHC is located in IP6 of the ring. It is designed to abort the beam for when an issue occurred in the LHC to prevent further damage.

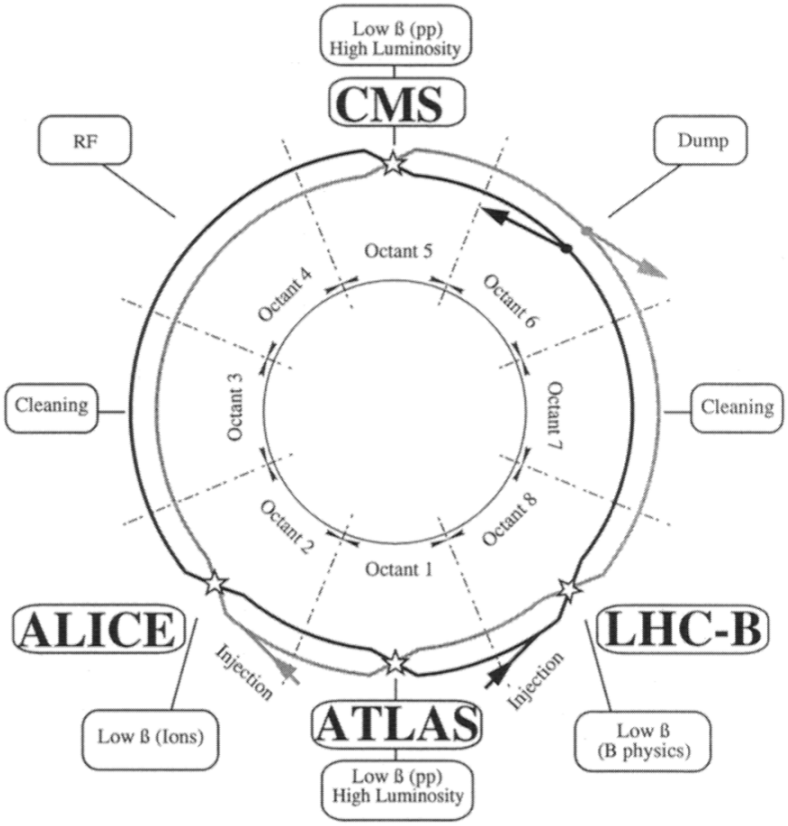

Figure 4.3: This figure shows the different parts of the two LHC rings along with its features [68].

4.1.6 The Magnets

The magnet systems in the LHC provide a way to control the proton beam after its injection from the SPS. The magnets of the LHC serves a couple of different purposes on the LHC: they bend the proton beams for them to stay on the circular cyclotron tunnels; they also focus and align the beam for collision for maximal interaction rate. Due to the high bending power needed, the main ring of the LHC uses NbTi superconducting magnets. A supporting cryostatics system cools the magnets down to 1.9K for the superconducting functionalities. The main dipole system is shown to be able to provide a magnetic field of up to 8.4T under this condition. There are a couple of different kinds of magnets along the LHC, each providing a different function in maintaining the beam for particle collision. The field quality can be summarized by the harmonic multipole analysis:

$$B_{\text{total}} = B_y + iB_x = B_1 \sum_n (b_n + ia_n)(Z/R_r)^{n-1} \tag{4.3}$$

where B_y is the dipole field in the y-direction, b_n and a_n is the multipole coefficients, Z is a complex

paramter that describes the coordinates of the magnet, R_r is the reference radius, the index of n, refers the to the poles of the magnet field, where n=1 refers to the dipole file, n=2 refers to the quadrupole field and so on.

The Main dipole magnets

The main magnet is a dipole magnet that bend the proton beams to make them stay on track in the circular tunnels. It can also be used to control the separation of the beam as it focuses and refocuses. The LHC has two beam pipes for each proton beam going in the opposite direction from the other. The Magnet has a twin-aperture system that allows it to bend both proton beams together. Figure 4.4 shows the cross-section of the dipole magnet.

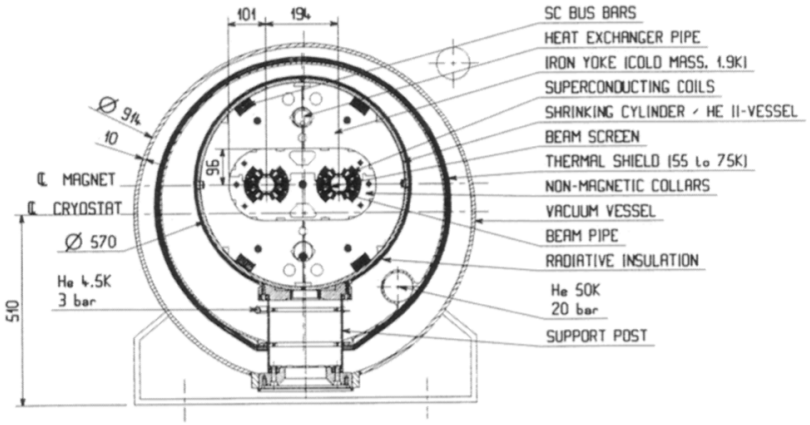

Figure 1: Dipole magnet cross-section

Figure 4.4: The cross-section of the dipole magnet [56].

The Quadrupole Magnet

The Quadrupole magnets are used in the LHC to focuses and defocuses the proton beams for collision. They are built in a way that is much like the main dipole, where single quadrupole magnet is capable of bending two proton beams. Figure 4.5 shows a cross-section of the quadrupole magnet.

The Sextupole and Dipole Corrector Magnet

In addition, there are corrector magnets that correct for the field error of the main magnets mentioned above. More design details can be found in the conceptual design report of the LHC [56].

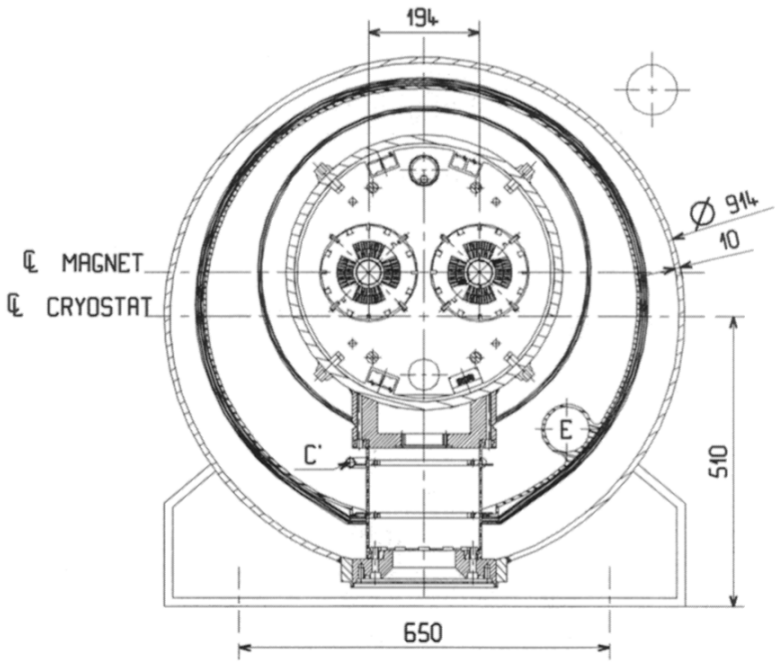

Figure 4.5: The cross-section of the quadrupole magnet [56].

4.2 The ATLAS Detector

The ATLAS detector is a general-purpose detector. It is the summation of a series of detector systems each produces different tracks to a particle. The ATLAS detector has a special emphasis on the muon system, as the dimuon final state was a main channel for the Higgs discovery. In the following sections, different parts of the detector will be discussed in detail.

The ATLAS coordinate system

The ATLAS detector uses a cylindrical coordinate system: Z-ϕ-η to describe the particles location after interactions. The z-axis runs along the beamline and starts at the origin (center and middle) of the detector. The x-y plane perpendicular to the z-axis described as the transverse plane is represented in the polar coordinate 4.7. The plane is described by two angles: ϕ is the 2π azimuthal angle on the x-y plane and the 1π polar θ angle with respect to the z axis is given in term of psuedorapidity, the term is Lorentz invariant and is its conversion to theta is given by Eq. 4.4. The δR quantity is used to describe the angular distance between particles, it is defined in Eq. 4.5 This quantity is approximately Lorentz invariant. Figure 4.7 shows the ATLAS coordinate system. Figure 4.8 shows the pseudorapidity(η) to angle conversion.

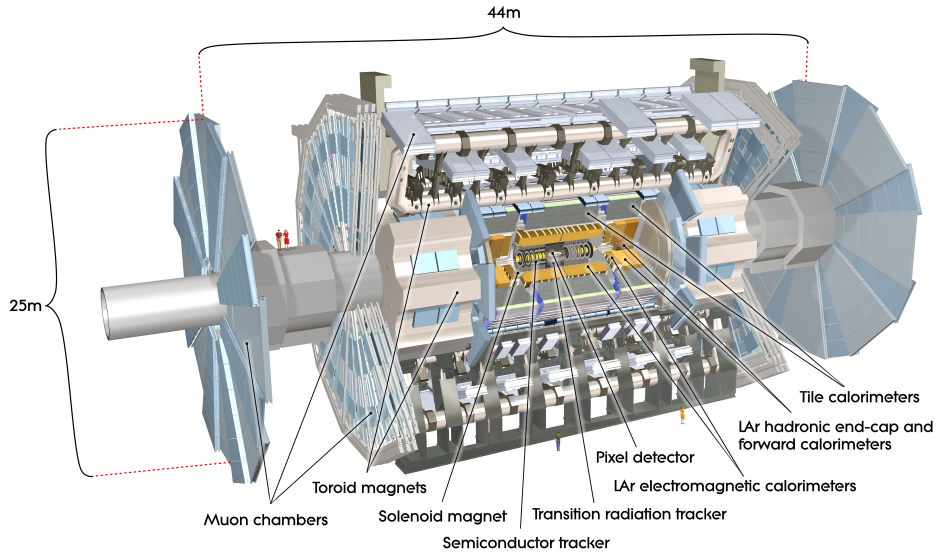

Figure 4.6: Computer generated image of the ATLAS detector[69]. Showing the different parts of the components involved.

$$\eta = \ln(\tan(\theta/2)) \tag{4.4}$$

$$\delta R = \sqrt{\delta\eta^2 + \delta\phi^2} \tag{4.5}$$

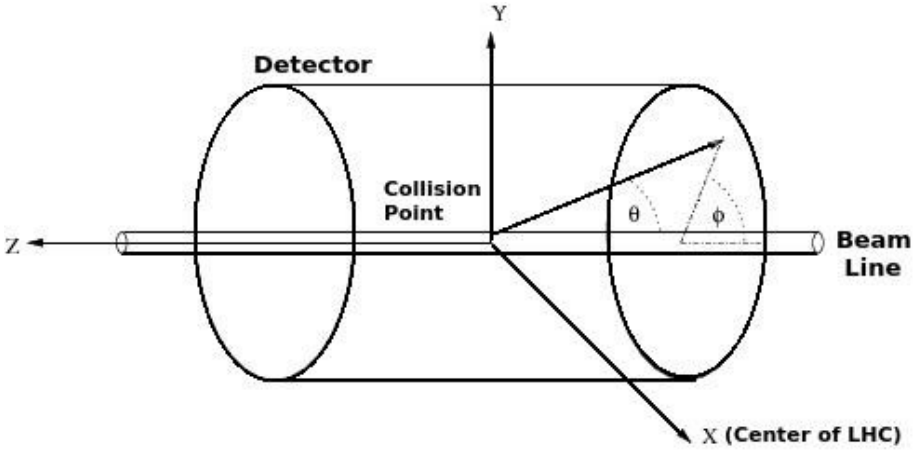

Figure 4.7: This figure displays the coordinate of the ATLAS detector system [70].

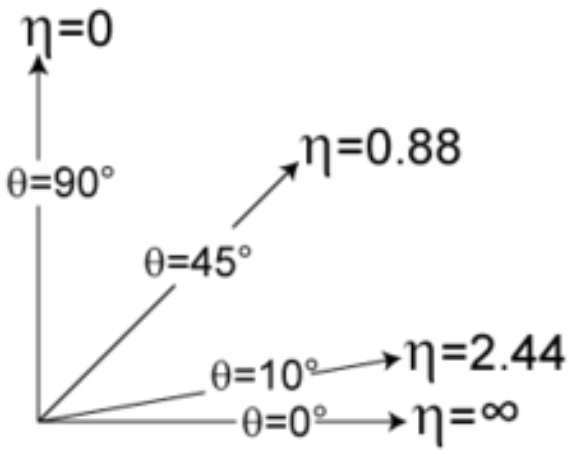

Figure 4.8: Pseudo-rapidity η to angle in degree conversion [71].

4.2.1 Inner Detector

The inner detector(ID) is the innermost part of the ATLAS detector. Its main function is to record charged particle trajectories. The tracks provide valuable information for the reconstruction of the primary vertices of particle interactions. All four parts of the ID are enclosed by a superconducting solenoid magnet of 2T aligned along the beamline, charged particles are curved into helical trajectories along the beamline. This is used for charge, mass and momentum calculation as well as particle identification.

The inner detector is made up of four different parts. From inside out, the Insertable B Layer, the Pixel detector, the Semi-Conductor Tracker(SCT) and the Transition Radiation Tracker(TRT). Its resolution is the highest in the innermost part of the detector and decreases outward. The following is a detailed description of the four parts of their coverage and detector mechanism.

Closest to the core of the detector is a very high-resolution insertable B layer(IBL). It was inserted after Run I to further extend the pixel detector coverage to $|\eta| < 2.9$. This helps with b-hadron identification through better vertex reconstruction.

Around the IBL is the Pixel detector. It is made of three layers of fine silicon pixels of spatial resolution of 10μ m in the r-ϕ direction and 115μ m in the z-direction. It provides a cylindrical coverage that covers up to $|\eta| < 2.5$. Electron-hole pairs are generated when charged particles passes through the silicon pixel. The signal is then read out through the applied electric field. Surrounding the pixel detector, there is a silicon microstrip detector called the Semi-Conductor Tracker (SCT). It is located in radii between 30-51 cm, which is made up of 4 layers of strip silicon sensor. Each SCT layer is made up of two overlapping sets of silicon strips at an angle with one another. The working mechanism of the detector is similar to that of the pixel detector, but the

resolution is slightly reduced to 17 μm in the r-ϕ plane and 580 μ m along the z-axis. The outermost part of the ID is called the Transition Radiation Tracker(TRT), made up of gas-filled straws. There are 70 layers in the barrel and 140 layers in each end cap covering up to $|\eta| < 2.0$. Each straw tube contains gas that can be ionized by charged particles, the electron formed in the process will then move toward the charged center of the straw to be read out for momentum, trajectory and charge calculation. The TRT also helps with particle identification, as charged particles alsoemit a photon and this probability is related to the Lorentz factor. Lower mass electrons emit more photons than charged hadrons. Therefore, this can be used to identify electrons over hadrons on top of track reconstruction. The TRT has a resolution of 130μ m in the r-ϕ plane.

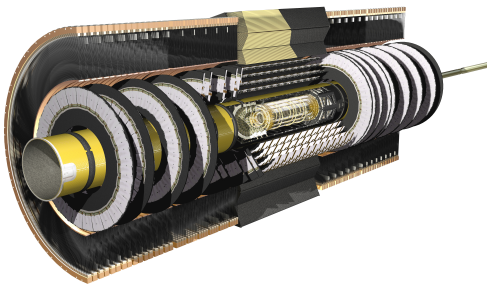

Figure 4.9: This image shows the computer generated image of the inner detector [72].

4.2.2 Calorimeter

The main function of the calorimeter is to provide energy measurement of particles. The ATLAS Calorimeter is split into two parts, sorted by the particle interaction method, The Electromagnetic-Calorimeter(ECal) utilizes the electromagnetic interaction and measures energy deposit in the form of electron and photon showers. The Hadronic Calorimeter uses strong hadronic interactions, energy is measured in the form of a hadronic shower in quarks and gluons. Both systems utilize a dense passive material for the particle showering and are sampled through a layer of sensitive active element for detection. Below, different components of the ECAL and the HCAL will be described in detail.

After tracking, the particle will first reach the ECAL. The first layer is the liquid-argon(LAr) electromagnetic(EM) calorimeter. The passive medium for showering is lead. The endcap portion covers $1.375 < |\eta| < 3.2$, and the barrel cover up to $|\eta| < 1.475$. The innermost layer has the greatest granularity of 0.003, the second layer has a resolution of 0.025 and the third layer is the most coarse.

The hadronic calorimeter(HCAL) measures hadron showering in the form of quarks and gluons.

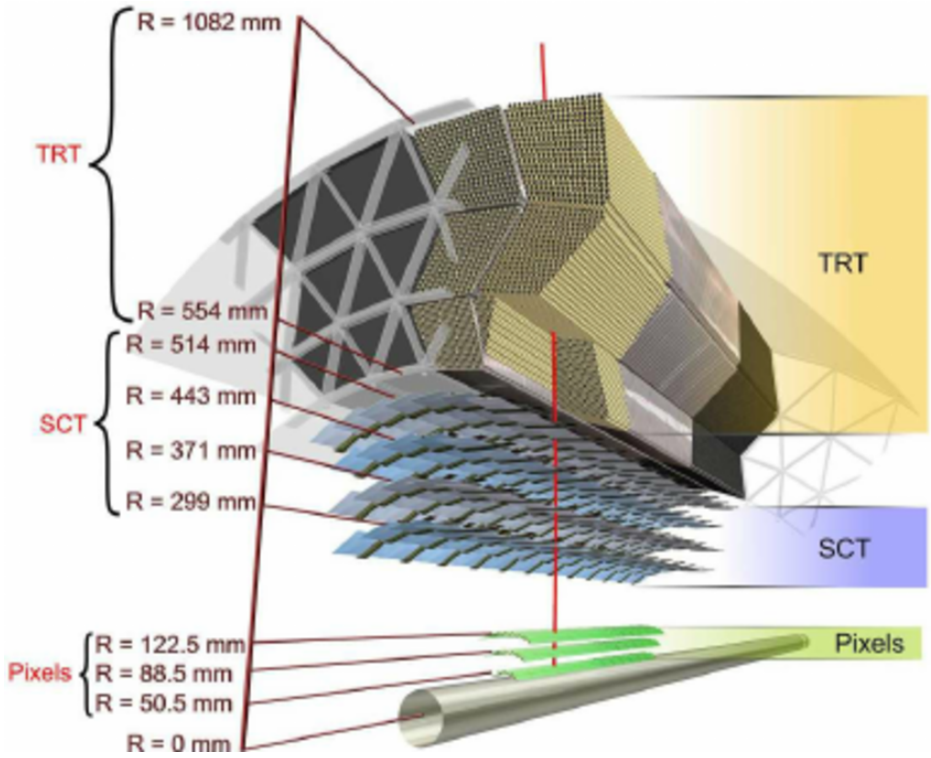

Figure 4.10: This image shows the computer generated image of the inner detector and its inner layout [72].

The barrel portion of it is made of a tile calorimeter. It uses steel as the passive element for showering and scintillating tiles as the readout active element.

The forward calorimeter end cap uses LAr for both the ECAL and HCAL, but copper-tungsten is used as the passive layer instead.

4.2.3 Muon Spectrometers

The muon spectrometer(MS) measures both the trajectory of muons and perform their triggering. The only type of particles that make it past the calorimeters and reach the muon spectrometer are either non-interacting particles, or they are the minimum ionizing particles, muons. Tracking and measurement of muons distinguish the particle from non-interacting particles, which include neutrinos or Beyond-the-Standard-Model physics candidates. The muon spectrometer system of ATLAS is surrounded by the superconducting toroid magnets, the barrel toroid provide up to 0.5 T between $1.6 < |\eta| < 2.7$, the end cap toroids provide up to 1T. The magnet bends the particles along the beamline into the end caps. For precision tracking, the muon system is made up of the Monitored Drift Tubes(MDTs) in both the barrel and the endcap region, in the forward region

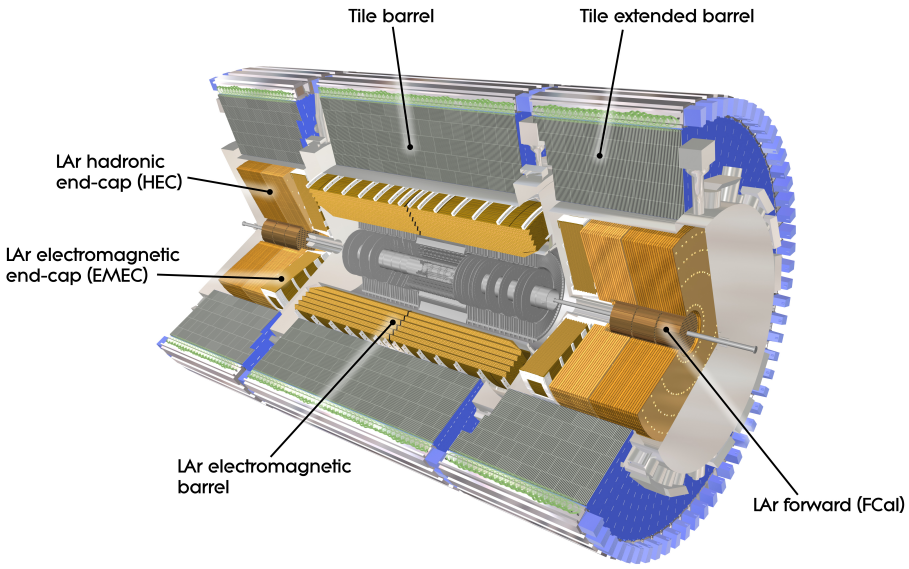

Figure 4.11: This image shows the computer generated image of the calorimeter and its inner layout [73].

there is a Cathode Strip Chamber(CSCs) in region $|\eta| > 2.7$ For triggering, it uses the Resistive Plate Chamber(RPC) in the barrel and the Thin Gap Chambers (TGCs) in the end cap for fast readout.

4.3 Data Acquisition of ATLAS

During Run II, the LHC performed proton-proton collision at $\sqrt{s}$ = 13 TeV at the instantaneous luminosity of $10^{34} cm^{-2} s^{-1}$. An approximate of 33.7 pp interaction per bunch crossing was delivered. At this collision rate, not all data could be processed and saved. The process of selecting experimentally interesting events is called "triggering". In Run II, triggering is administered and controlled by a central trigger processor which assigns different information from detectors to different part of the trigger computing system. There are two levels of triggering in ATLAS Run II, the low level hardware-based trigger is called L1 triggers, the second level software based high level triggering is called the High-level trigger(HLT). The L1 trigger filters through the input at 40 MHz to 100kHz. This is done by looking at energy deposits at the calorimeters that could be candidate leptons, jets, or photons. Muons are triggered by the hits that formed towers in the MS system. Events that pass through the L1 trigger will then be passed onto the HLT. The HLT further filters the 100kHz events received to 1kHz for writing to disk for offline analysis. The HLT is software-based. It further defines region-of-interest in detector and filter events that do not fit the trigger

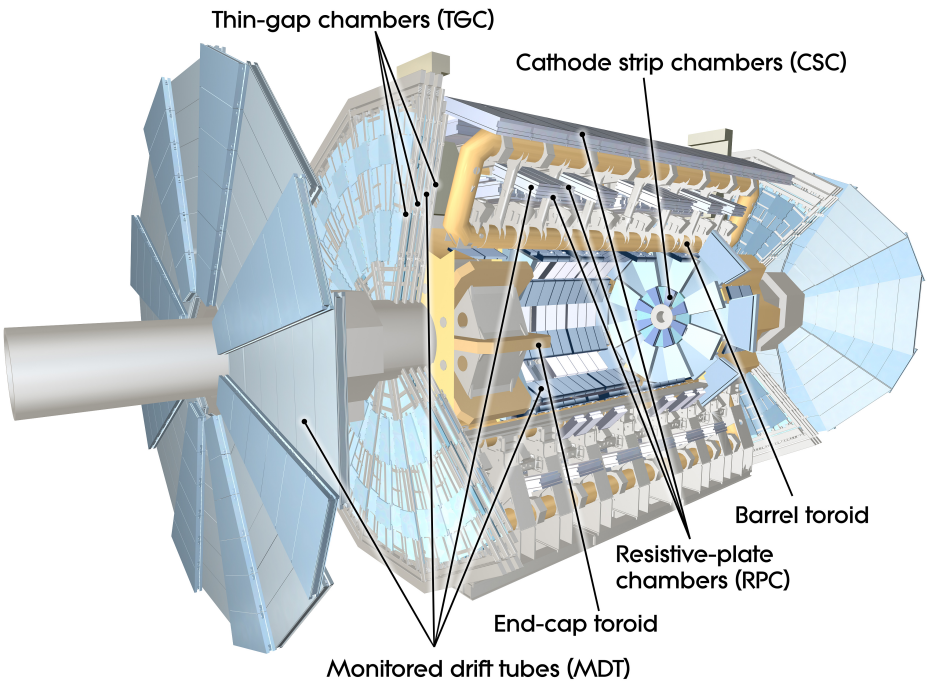

Figure 4.12: This image shows a computer generated image of the muon spectrometer [74].

selection criteria. High-level objects are created from the online information and an event loop is used to discard events that do not fulfill the trigger criteria. Events are saved to "trigger chains" for later analyses, they are sorted into different analysis derivations with basic criteria applied for different types of analyses.

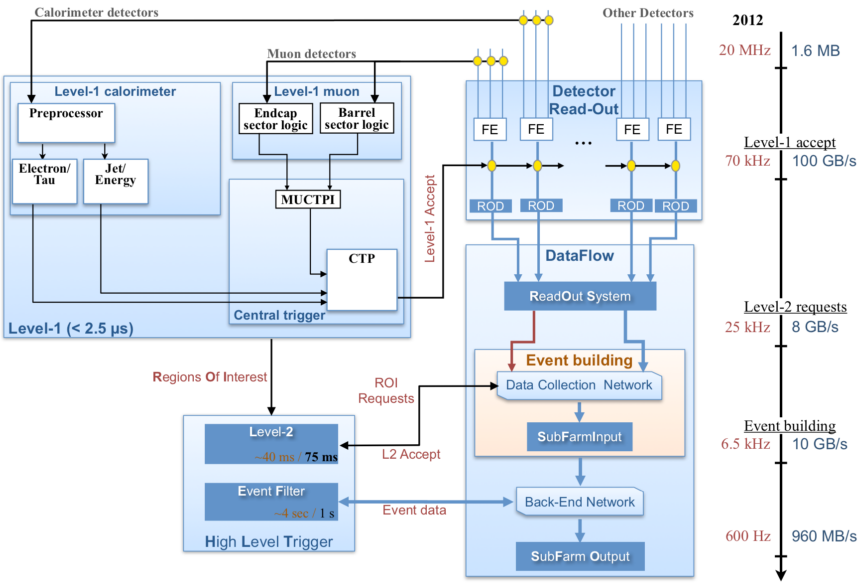

Figure 4.13: This image shows the schematic overview of the ATLAS triggering system [74].

Chapter 5

Common Analysis Items

First, you crack an egg into a small bowl.

–Unnamed Cookbook

After the collisions and interactions in the LHC, final state particles leave their mark on various detector components as electronic signals. These electronic signals are saved in hard disks and tapes. It takes various steps of reconstruction identification, cleaning and calibration before the raw electronic information becomes analysis-ready physics objects. The different interactions particles have on various detector components create different distinct signatures for their identifications. Figure 5.1 shows the different signatures that different particles leave on the ATLAS detector.

In this chapter, various analysis final state objects are described. In Section 5.1, detector tracks and vertex construction is covered. In Section 5.2, Section 5.3 and Section 5.4, the formation of muons, jets and photons from detector signal through their reconstruction, identification, isolation as well as calibration are discussed in detail.

5.1 Tracks and vertices

Charged particles leave trajectories in two distinct ATLAS sub-detector systems, namely the inner detector(ID) and some also reach the the muon system(MS). Details regarding the subdetector system can be found in Chapter 4.

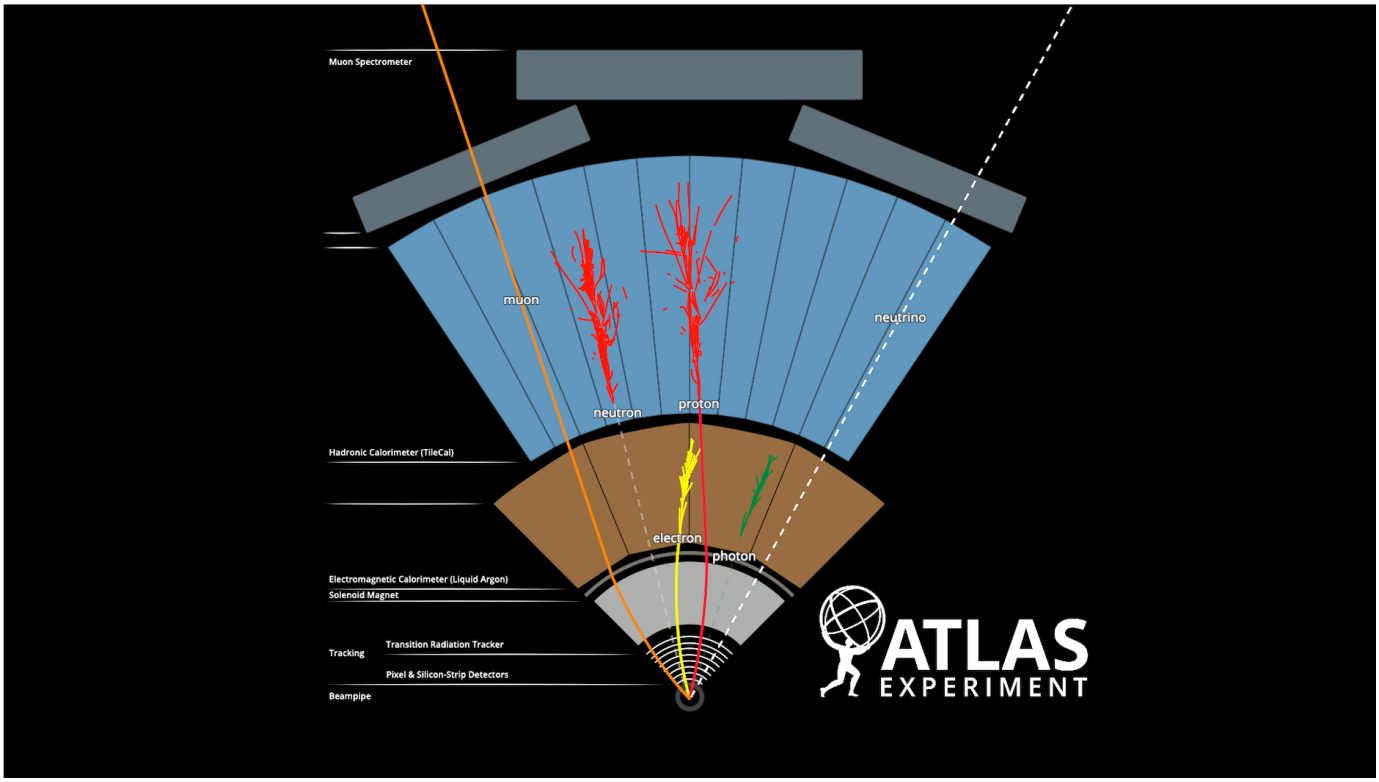

Figure 5.1: Particles displays distinct signatures [75].

5.1.1 ID Tracks

Hits is registered in an active detector element when a particle deposited enough energy to reach a predefined signal-to-noise(S/N) ratio. To reconstruct a track from detector raw hit information, coincidence measurements in multiple layers are first used to find a track seed. Then, a Kalman-filter is used to fit the tracks [76], irrelevant hits from pileup [1] are removed through the filter. Figure 5.2 shows a schematic diagram for a track.

5.1.2 Vertices

Once tracks are formed in the inner detector, primary vertices can be constructed from the track directions and their intersection points. Vertexing picks out tracks and hits that are associated with a single interaction. It is helpful in discriminating event-of-interest tracks from pileup tracks. Effective vertexing is of great importance to event reconstruction, especially in more recent LHC runs, where the higher luminosity has resulted in additional in-time and out-of-time pileups.

[1] Pileups are hits and tracks that result from multiple collisions other than the primary collision. In-time pileups are hit and tracks that came from interactions during the same collision event, out-of-time pileups are hits and tracks comes from collisions of different event.

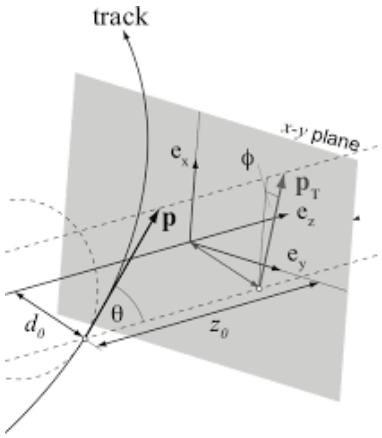

Figure 5.2: Schematic view of how the parameters associated with track creation in ATLAS.

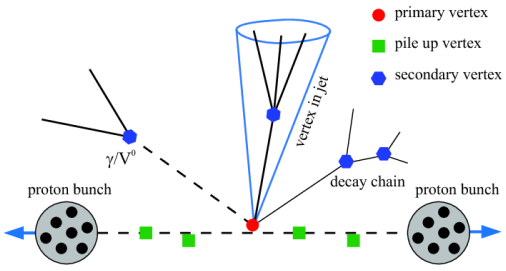

Figure 5.3: Schematic view showing vertexing in ATLAS[77].

Vertexing consists of a couple of different steps: First, a vertex seed is found by filtering the points where most interactions are found. Then, tracks consistent with the chosen vertex seed are put into a group. After that, the vertex position and the associated error of the vertex is found by an adaptive vertex fitting algorithm [76]. Lastly, the unused tracks are used for the next vertex creation. The process then repeats until no tracks remain.

The vertex with the highest P_T particles originated from it is considered the hard-primary vertex of the event, the others are considered the pileup primary vertices. Somtimes particles produced from the primary vertex decays further, the interaction points where the further decay occur are known as the secondary vertices.

Particle formation from detector hit information in the following sections relies on the tracks and primary vertex reconstruction above.

5.2 Muons

Muons in ATLAS are formed from both the tracks and primary vertex information described in the above section. Muon reconstruction mainly relies on ID and MS information, while information from the calorimeter is sometimes also used for low P_T muons. There are four different muon reconstruction strategies, as different transverse momentum(P_T) ranges and detector hit locations leave distrinct muon signatures. From these four reconstruction strategies, four muon working points, which are muons set in events chosen with pre-defined criteria, are derived [78].

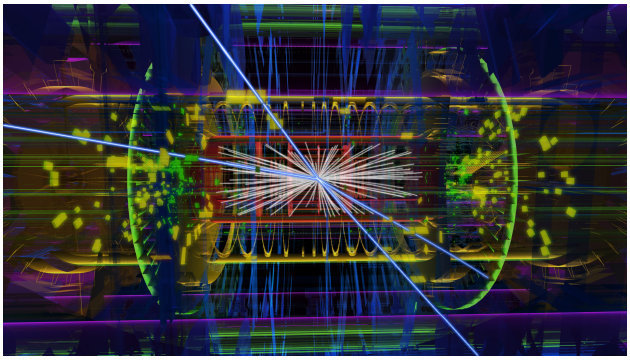

Figure 5.4: Visualization of a four muons event in the ATLAS detector[79]. The four muons are visualized as blue tracks that travel from the primary interaction point through the inner dectector, the calorimeter and the muon system to beyond the detector.

5.2.1 Muon Reconstruction

Reconstruction of muons is performed in the following way: tracks are found in one part of the detector through pattern finding of hits in the ID/MS chambers. At least two matching segments from different subdetector parts are needed to form a track candidate. From the track candidate formed, global χ^2 fits are performed, outliers from the fit is dropped and hits along the fitted track is added. Though they all share a common principle, various detailed reconstruction strategies are used for muons in different P_T ranges and detector locations to maximize reconstruction efficiencies [80].

- **Combined muon(CB)** This strategy is optimal for the muons that are detected in both the ID and the MS. It applies for muons found in both the barrel and end-cap region of the detector. Tracks are constructed from each of the ID and the MS. A global refit is done to remove outliers to improve the fit quality. This is first done by an outside-in approach where the tracks in MS are matched with tracks in the ID. Combined muons are also complemented by the inside-out muons: It looks for MS hits that can be associated with ID tracks and recovers muons that don't make it to the MS completely.

- **Segment-tagged muons(ST)** This method is used to identify lower P_T muons that do not travel to the MS. If a track in the ID can be matched to at least one track segment in the MDT in the barrel or CSC in the end-cap, it will be selected as a segment-tagged muon.

- **Calorimeter-tagged muon(CT)** This reconstruction method is used for even lower P_T muons that do not have enough energy reach the MS. Muons between 15 GeV < P_T < 100GeV are formed from matching a track in ID with energy deposits in the calorimeter that match the minimum-ionizing particle. This is optimized for barrel muons of $|\eta| < 0.1$.

- **Extrapolated muon(ME)** This reconstruction strategy is designed for muons that are very forward and are buried under noise from pileup. Muon tracks in the MS with a loose compatibility to the originating IP are accepted as ME muons. This strategy extends the acceptance of muons in the forward region from $2.5 < |\eta| < 2.7$. As there is no ID coverage in this region, other methods are not applicable.

5.2.2 Muon Identification

In ATLAS, the muon of interest are the muons that comes from the hard primary vertex decay. Muons formed this way are known as "prompt muons". "Non-Prompt" muons came from the semileptonic decay from jet fragmentations. Muon identification is a set of selection criteria applied to the candidate muons to cut out "non-prompted" muons from light hadron decays that would result in in-flight detector production of muons. In different analyses, depending on the signal type, several muon identification working points are used.

A couple of criteria are used for muon identification: $q/p_{\text{significance}}$, ρ' and χ^2_{norm}. They are defined as [80]:

Discrimination Criteria

- **q/p significance**

$$q/p_{\text{significance}} = |(q/p)^{ID} - (q/p)^{MS}|/\sqrt{\sigma^{MS}_{P_T} + \sigma^{ID}_{P_T}} \tag{5.1}$$

This is the absolute value of the difference between the charges and the P_T measurement divided by the sum of error in the P_T measurement of both the ID and MS. q is the charge, and p is the momentum of the particle. It is expected that the value is smaller for prompt muons as the particle will have similar q/p ratio in both the ID and the MS if muon was created in the primary vertices rather than jet fragmentation later on.

- ρ'

$$\rho' = |P_T^{MS} - P_T^{ID}|/P_T^{\text{Combined}} \tag{5.2}$$

This is the absolute value of the difference between the P_T of the MS and the ID divided by the combined P_T of the muon candidate. A smaller value indicate a better match between the ID muon and the MS muon candidate.

- χ^2_{norm}

This is the χ^2 of the fit from the combined muon track from both the ID and MS. A smaller value shows that the ID and MS muon track candidates have the same direction and is therefore more likely to originate from a "prompt muon".

These selection criteria for the muon groups above result in five different working points.

Muon Working Points

- **MEDIUM**
This is the most commonly used working point. q/p significance < 7. It accepts only the CB and IO muons.

- **LOOSE**
The loose working point accepts all the muons that pass the medium working point. It also accepts low-P_T muons, including IO muons with P_T lower than 7GeV. Some ST and CT muons are also accepted under certain circumstances [80]

- **TIGHT**
This working point accepts a subset of the medium working point muons. In addition, they are required to have a normalized χ^2 of less than 8. The requirement on q/p compatibility and ρ' varied and depends on η and P_T of the muon. Details can be found in [80].

- **HIGH** P_T
This working point only accept muons that also pass the medium working point requirement. Owing to their high P_T, the reconstruction can be done with the MS alone for a higher resolution.

- **LOW** P_T
The Low-p_T working point includes all of the muons in the medium working point, it's identical to the medium working point muon set above P_T =18GeV. But this working point also includes muons with lower P_T that does not make it to the middle of the MS, this working point includes muons down to 3 GeV.

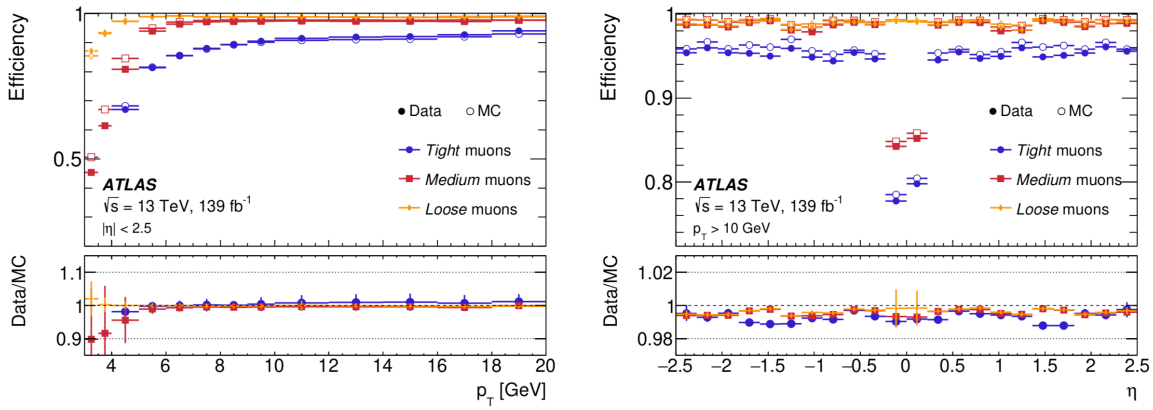

Figure 5.5: This figure shows the reconstruction and identification efficiencies in different variable range in different working points[78].

5.2.3 Muon Isolation

Following identification, muon isolation is performed. Other "non-prompt" muons that resulted from heavy hadron decay before reaching the inner detector. They would not have been cut out from the identification step. Since in comparison, "prompt muons" usually result in back-to-back isolated higher-P_T muons, the relatively high associated neighboring hits from "non-prompt" heavy flavor muons can be used as criteria for discrimination. The step performed is known as muon isolation. Depending on the muon energy, two different variables are used for muon isolation. One is the track-based isolation and other is calorimeter-based isolation.

Isolation Variables

The parameters used in the isolation criteria are defined as the following:

- $P_T^{\text{varcone size}}$
  The track-based isolation variable, $P_T^{varcone\ size}$ are the sum of the P_T of all the tracks in a variable-sized cone. The variable-sized cone(varcone) is defined as below.

$$\delta R = min(\frac{10}{P_T^{\mu}[\text{GeV}]}, \delta R_{\text{varcone size}}) \tag{5.3}$$

  The term is P_T dependent, the larger the P_T, the smaller the cone.

- $E_T^{\text{topocone size}}$
  A calorimeter based parameter $E_T^{\text{topocone size}}$ is defined as the sum of the energy deposit in a

δR size topo cone.

Different working points are developed for balancing "non-prompt" rejection, "prompt" acceptance and the isolation performance when in close proximity to other objects. The working points are defined with respect to different variables. Details can be found in [81].

Table 5.1: Definitions of the muon isolation Working points [81].

Isolation WP	Definition	Track $p_T$requirement
*PflowLoose**	$(p_T^{\text{varcone30}} + 0.4 \cdot E_{\text{T}}^{\text{neflow20}}) < 0.16 \cdot p_T^{\mu}$	$p_T > 500$ MeV
*PflowTight**	$(p_T^{\text{varcone30}} + 0.4 \cdot E_{\text{T}}^{\text{neflow20}}) < 0.045 \cdot p_T^{\mu}$	
*Loose**	$p_T^{\text{varcone30}} < 0.15 \cdot p_T^{\mu}$, $E_{\text{T}}^{\text{topocone20}} < 0.3 \cdot p_T^{\mu}$	$p_T > 1$ GeV
*Tight**	$p_T^{\text{varcone30}} < 0.04 \cdot p_T^{\mu}$, $E_{\text{T}}^{\text{topocone20}} < 0.15 \cdot p_T^{\mu}$	
HighPtTrackOnly	$p_T^{\text{cone20}} < 1.25$ GeV	$p_T > 1$ GeV
*TightTrackOnly**	$p_T^{\text{varcone30}} < 0.06 \cdot p_T^{\mu}$	
PLBDTLoose (PLBDTTight)	$p_T^{\text{varcone30}} < \max(1.8 \text{ GeV}, 0.15 \cdot p_T^{\mu})$ BDT cut to mimic *TightTrackOnly* (*Tight*) efficiency	$p_T > 1$ GeV

5.2.4 Muon Calibration

The Monte Carlo simulation is often imperfect in its parton showering and detector simulation. The imperfection results in difference in data and MC given the same underlying process. This makes understanding the tree level process from the data represent difficult. Given this, a calibration factor is derived from comparing the MC to data using some known physics process J/Ψ to $\mu\mu$ and Z to $\mu\mu$. The calibration is done on the P_T of the muon. The calibration is dependent on the detector angle, and the formula for P_T correction is summarized as below, where the constants are derived from the data and the simulated samples.

$$P_T^{\text{Cor,Det}} = \frac{P_T^{\text{MC, Det}} + \sum_{n=0}^{1} S_n^{\text{Det}}\eta,\phi(P_T^{\text{MC, Det}})^n}{1 + \sum_{m=0}^{2} \delta r_m^{\text{Det}}(\eta,\phi)(P_T^{(}\text{MC, Det})^{(m-1)} g_m} \tag{5.4}$$

Here $P_T^{\text{MC, Det}}$ is the uncorrected transverse momentum, g_m is a unit Gausssian distribution, $\delta r_m^{\text{Det}}(\eta,\phi)$ and $S_n^{\text{Det}}(\eta,\phi)$ are the momentum resolution smearing and scale correction resolution. Det in the equation is short for "Detector, which could be ID or MS. The S_1^{Det} term corrects for inaccuraty in the description of the magnetic field, whereas the S_0^{Det} corrects for the inaccuracy in the simulation of energy loss in the calorimeter.

The correction is then applied to the combined muon in the following way:

$$P_T^{\text{Cor, CB}} = f \cdot P_T^{\text{Cor, ID}} + (1 - f) \cdot P_T^{\text{Cor, MS}} \tag{5.5}$$

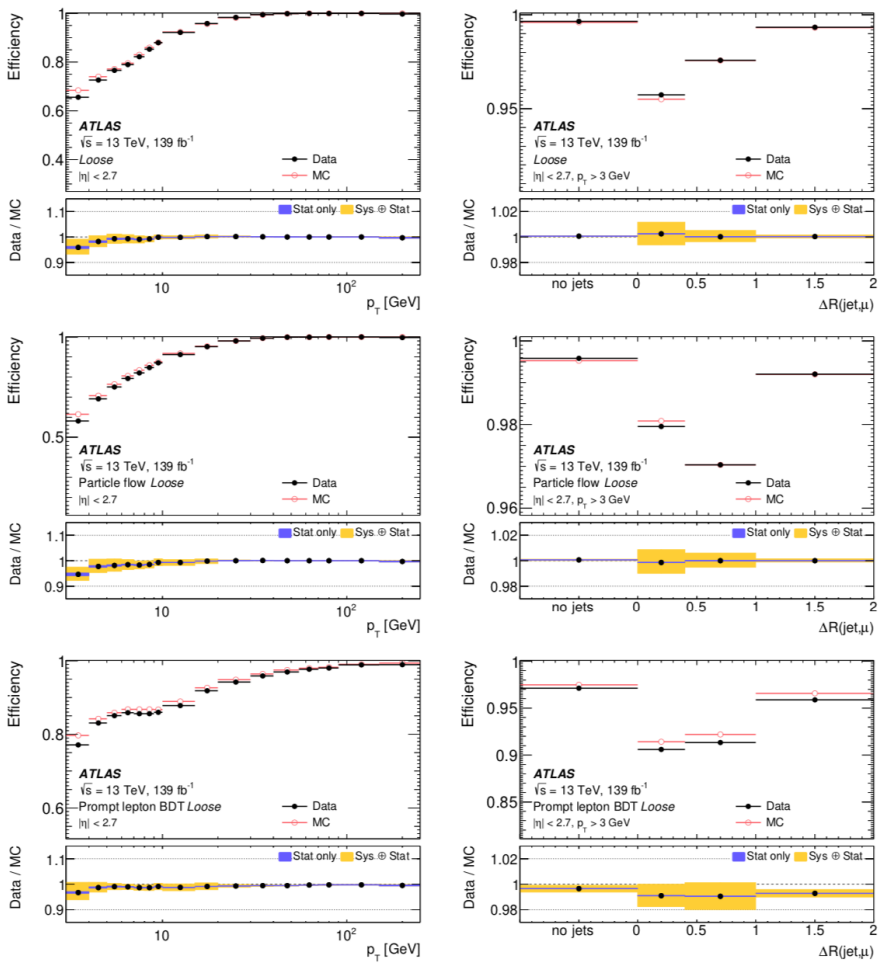

Figure 5.6: This figure shows the isolation efficiency in different variable range in different working point[78].

The weight f in the above is obtained from MC simulation. $P_T^{\text{Cor, CB}}$ and $P_T^{\text{Cor,ID}}$ are the corrected transverse momentum in CB and MS respectively.

5.3 Jets

Colored charge particles interact under the strong force. This includes quarks and gluons. Under the strong force, the energy potential of these color charges increases with their distance apart from each other. The increased potential leads to extra quark and gluon formation as energy and mass is one and the same. This effect is known as parton showering. The color confinement of the strong force result in further hadronization of the showered products. Showering lead to a cascade of energy deposits in the detector. The jet algorithms aims to reverse the process, it reconstructs

the physics properties of the the original primary quark/gluon from the resulting energy deposits. Figure 5.7 is a visualization of an ATLAS event with two high p_T jets.

The following is a schematic understanding of how jet finding is achieved.

• **Jet showering**

Quark/gluon formed → Parton Showering → Hadronization → Detector Energy Deposit

• **Jet Reconstruction**

Energy Deposit on Detector → Topo-cell Clustering → Topo-Clusters → Jet-Finding Algorithm → Jet

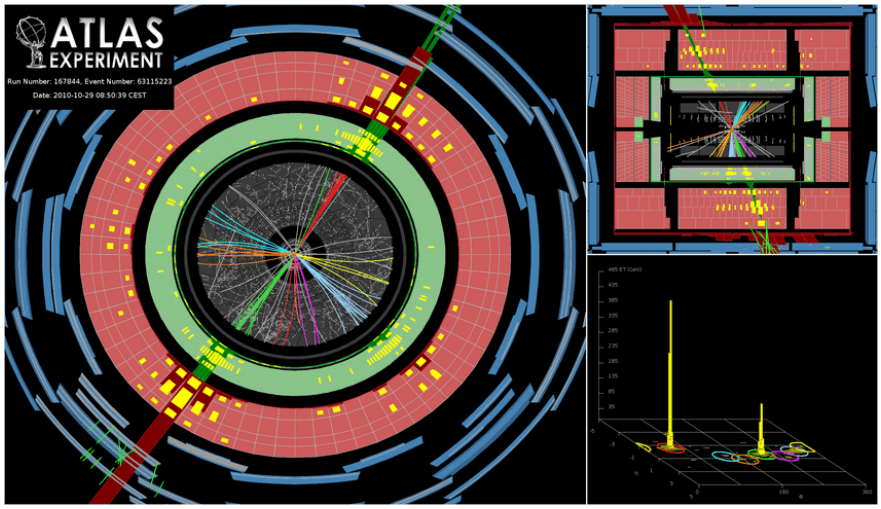

Figure 5.7: An simulation ATLAS event containing two high p_T jet event [82].

Topo-cell clustering

This step clusters the lowest level calorimeter cells energy deposits into "topological clusters", which are cluster of cell deposit with high signal-to-noise (S/N) ratio collected from proximity in the detector. ATLAS uses a 3-D clustering algorithm and it is described as the foolowing:

First, a seed cell with a high S/N ratio above a 4 is found. Then, cells neighboring the seed cells in the in 3 dimensions above S/N 2 are collected along with the seed cell to the topocluster. Lastly, a final set of cells that surround the second set of collected cells above S/N 0 are added to the cluster.

Jet Finding algorithm

Jet finding algorithm aims to identify all the deposits that can be traced back to the original hadronic particle. An important feature for a jet finding algorithm is that it needs to be infra-red and collinear(IRC) safe. In an IRC safe algorithm, soft and small angle radiation that showers from the jet will not change the kinematics of the jet. This requirement avoids the divergence in probability calculations that would lead to infinities when jet splitting happens.

All of the main ATLAS jet finding algorithms make use of the following quantities:

$$d_{ij} = min(k_{ti}^{2p}, k_{tj}^{2p})\frac{\Delta_{ij}^2}{R^2} \tag{5.6}$$

$$d_{iB} = k_{ti}^{2p} \tag{5.7}$$

Here, B is the beam, R is the angular distance, $\Delta_{ij}^2 = (y_i - y_j)^2 + (\phi_i - \phi_j)$, k_{ti}, y_i, and ϕ_i are the transverse momentum, rapidity and azimuth angle of particle i. p is a parameter on the energy scale [83]. d_{ij} and d_{iB} are the distance between particle i and j and distance between i and B respectively.

The algorithm clusters the topoclusters with the smallest distance together 5.6, until no topoclusters are left. p is taken to be -1 for the anti-KT jet finding algorithm; 1 for the KT algorithm and 0 for C/A(in addition, in C/A, $d_{iB} = 1$). The Anti-KT algorithm chooses to merge high transverse momentum objects with one another, and the KT algorithm merges low transverse momentum with one another. The C/A algorithm only weights on distance.

The current ATLAS standard jet finding algorithm is the Anti-KT algorithm. It is an IRC safe algorithm. The algorithm is also not susceptible to underlying events and pile-up as the other two.

5.3.1 Jet calibration

After jets are formed, they need to be calibrated to reflect the direction, momentum and energy of the originated quarks or gluons. The jets are required to be calibrated. In ATLAS, jets energy is measured out in both the EM calorimeter and the hadronic calorimeter. The jet finding algorithm operates in the EM scale(as distance in the strong force is energy scale dependent). Jet energy correction needs to be performed before the object can be used for analysis to remove pile up and correct for direction. The jet calibration takes the following steps as shown in Figure 5.8.

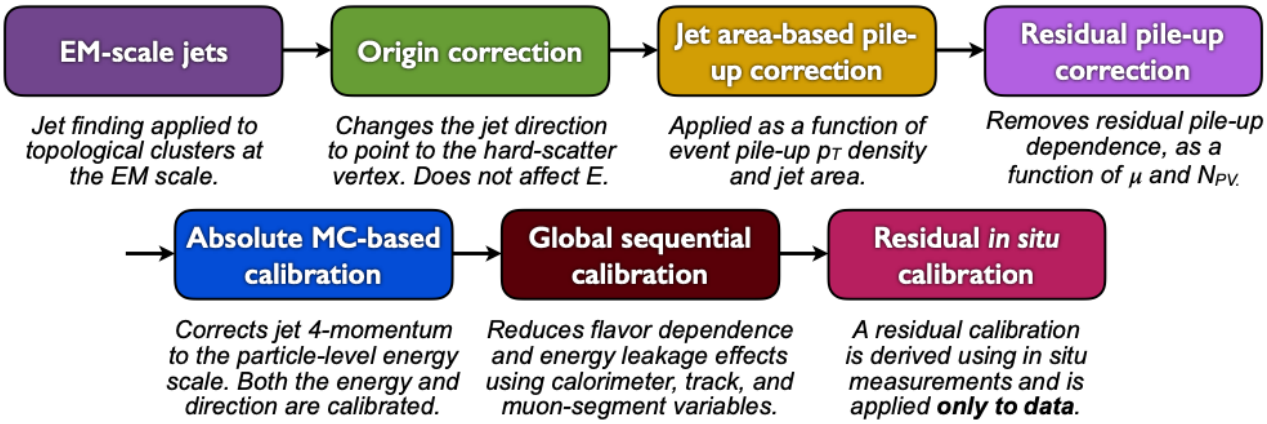

Figure 5.8: The steps of calibration performed on the jet objects.[75]. The Jet area is the area of the jet in angular distance for pile-up correction, μ is the interaction rate per bunchcross and N_PV is the number of primary vertices. The paritcle level scale is the measurement obtained with both the tracker and the calorimeter, energy leakage is the out of cone deposit in the detector that belongs to the original quark/gluon.

5.4 Photon

Photons in ATLAS are reconstructed from clusters in the EM Calorimeter sometimes paired with tracks in the tracker. Photons and electrons shares a similar reconstruction algorithm. Like muons and jets, photons are first reconstructed, identified, isolated and lastly calibrated before being used for analysis.

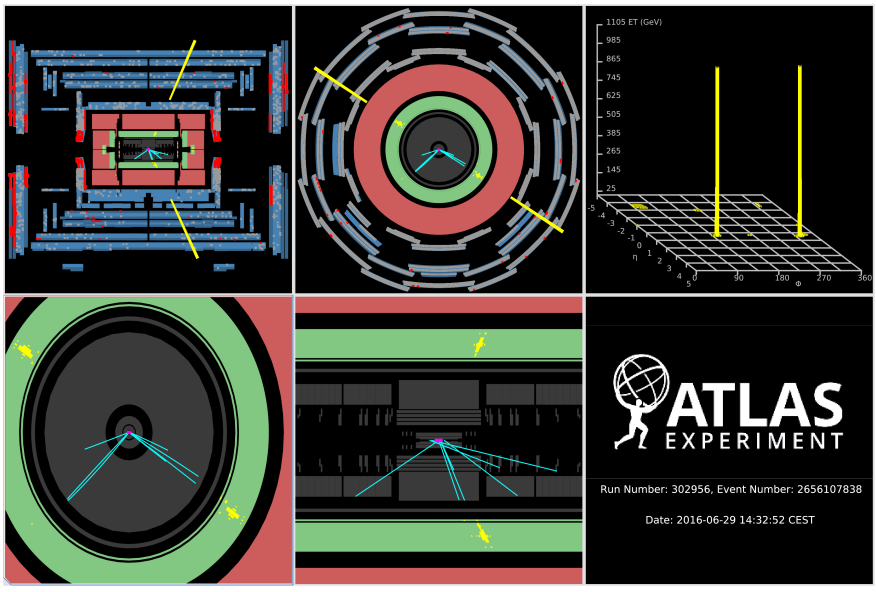

Figure 5.9: An ATLAS event display that contain two photons [84].

5.4.1 Photon Reconstructionn

Photons interact with the EM calorimeter. They shower and leave deposits in the active material. The first step to photon reconstruction is the finding of a seed cell for clustering. A sliding window of $\delta\eta \times \delta\phi = 0.025 \times 0.0245$ is used to scan for a clustering seed with energy deposit above 2.5 GeV. Neighboring hits are added to the seed to form a cluster through the clustering algorithm [85]. These cluster are matched by tracks in the inner detector. These tracks are used for vertex construction. If no vertex or tracks are matched, they are unconverted photons, otherwise, they are considered converted photons. Converted photons are photons that originates from electrons.

5.4.2 Photon Identification

Like muons, not all photons candidates are photons generated from the primary vertex. "Prompt" photons, that came the primary process are of interest in the analysis (dijetISR) worked on. A main source of"non-prompt" photons on ATLAS came from jets decay. Photon identification are mainly placed on shower shapes in the calorimeters [86].

There are two photon working points, the loose working point uses information from the the calorimeter. The tight working point uses information from the calorimeter strips and has different requirements for uncoverted and converted photon for optimal classfication power. Details can be found in [86].

5.4.3 Photon Isolation

Photon isolation is a strategy that is effective in identifying the prompt photons from the "non-prompt" photons that are produced along other objects. The isolation is a cut on the energy or transverse momentum in δR cone size around the photon candidate. The isolation variable for the calorimeter and tracker are calculated separately [86].

5.4.4 Photon Calibration

Photons in ATLAS takes the following steps to be calibrated to correct the estimation of energy deposited in the calorimeter, to correct for the relative energy scale in the different layers of the EM calorimeter, correct for the non-uniformities in the calorimeter response affecting the data and to provide an overall adjustment [86]. First, the photon energy is estimated from the deposits in the calorimeter by a multivariate regression algorithm trained on simulated events on data. Later, correction is then done on the energy scale in the different layers of the EM calorimeter from Higgs

to $\mu\mu$ data, the correction on the calorimeter layers are then applied to the photons calibrated. After that, geometric correction is done on the data to correct for the non-uniformity in the detector in the boundaries of the calorimeter modules. Lastly, an overall adjustment on the energy scale is done in the data [86].

Chapter 6

The Standard Analysis Method for Resonance Finding

But the truth can be re-found; most often it has already been written elsewhere.

–Jacques Lacan, Ecrits

6.1 Introduction

Both analyses presented in this thesis fall into the resonance search category, which are analyses that look for bumps like excesses on top of smooth backgrounds. The method is simple in its experimental signature, as can be seen in Figure 6.1 and theoretical calculation. Many particles have been discovered in this way before, which include the J/Ψ [87] [88], the Υ [89], Z [91], and the Higgs boson. The method has great potential in making future discoveries. This chapter describes the analysis methods used in performing the analyses covered in Chapter 7 and Chapter 8.

These analyses perform searches in the resonance mass variable(the target signal spectrum). The variable came from the addition of the 4-vector of the two candidate final state particles.

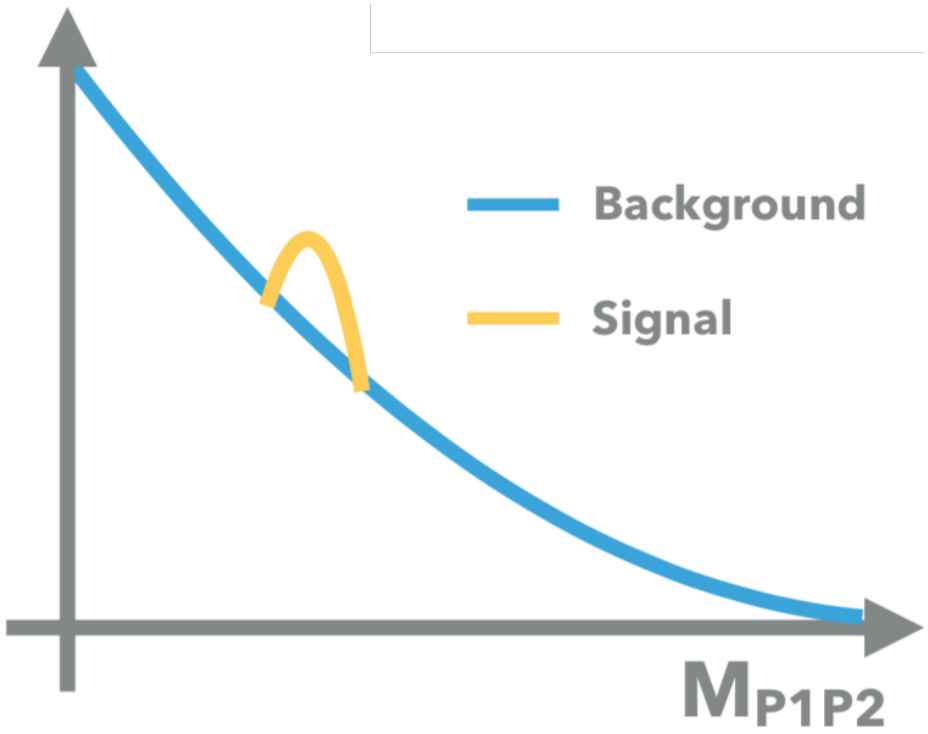

Figure 6.1: This cartoon illustrates a typical resonance finding experimental signature in the resonance mass variable.

The chapter below provides a recipe for a resonance finding analysis: Monte Carlo generation(MC) is used to aid statistical procedure formulation. Its generations are detailed in Section 6.2. Proper data preparation required for both the data and the MC before statistical analysis is discussed in Section 6.3. The background estimation method and their verification tests are given in Section 6.4. The search for resonances as excesses is quantified statistically. Two separate statistical statements, one on excess finding, and the other one on signal strength upper limit setting are discussed in Section 6.5.

6.2 Simulated Physics Events(Monte Carlo)

Simulated physics events(Monte Carlo) are used to design the cuts which optimize the selection, verifying the validity of the data-driven background estimation strategies as well as deriving the different systematic uncertainties(E.G. energy resolution uncertainty) present in the experiment. An event generator used by ATLAS is PYTHIA [92], which is used to simulate the proton-proton collision, the tree-level generation, the hadronization, the fragmentation as well as the showering. Other than PYTHIA, the PowHeg generator [93] and NLOJet++ [94] are also used. The detector effect is simulated by GEANT4 [95].

6.3 Data Preparation

The data of the analyses discussed in this chapter originate from collision data. It is collected from the ATLAS detector and its triggering hardware and software discussed in Chapter 4. The data collected as energy deposits and tracks are analyzed and collected analysis objects as discussed in Chapter 5. After that, the dataset goes through several more steps in data preparation before getting analyzed for resonance finding in the chapter: the following is a short outline of how data are being prepared for the analyses.

First trigger chains addition is studied, balancing both events collected and signal sensitivity of the dataset studied. After that, the data is processed with the optimal analysis object working points applied, then, event cuts are introduced to maximize the signal sensitivity while reducing the background events. As the resolution of the data collected from detector is constrained by detector resolution, a binned approach is taken. The binning is selected based on studies on the detector resolution and signal sensitivity consideration. (Details are described in Section 6.3.1). Finally, a cross-check that compares the data and MC is performed variable regions other than the target signal spectrum. An agreement between MC and data ensures both the previous steps in data preparation are executed correctly and the MC modelling is close enough to data descriptions. After all the data preparation steps are completed, a target signal spectrum is available to be analyzed statistically for resonances.

6.3.1 Binning Strategy

The binning is optimized through the mass resolution of the target spectrum. Since mass resolution describe the maximal sensitivity seen in the target spectrum, binnning is often chosen to be the resolution. This avoid the lost of information, and allow for targetted signal to be searched for the the bump like shape with sufficient sensitivity. The mass resolution is found through MC studies. As its main contributor is the detector response, it can be studied through by performing a Gaussian fit on the $m^{reco} - m^{truth}$ on MC sample, where $reco$ is reconstructed event from GEANT4, and $truth$ is the truth events showering and detector reconstruction from the same event. A Gaussian fit is performed to find the mean (μ) and the width(σ). The width found for the particular reconstructed mass is the resolution at that mass.

6.4 Background Modeling

After the dataset has been prepared, the spectrum is ready to be analyzed to search for resonances. In order to analyze statistically whether there is an excess of events beyond the Standard Model

prediction, a reliable prediction of the Standard Model events in the signal region along with its statistical error is needed. The step to estimate background Standard Model events is known as background modeling. Many considerations go into background modeling for analysis: accuracy, availability, size of the estimation error and ease of implementation. In ATLAS, the following methods are recommended for background modeling in order of descending preference: First, the background estimation can be found by the MC generation of the events when the simulation is reliable and inexpensive for data generation. Second, in cases where the MC generated is low in event count but reliable in shape, an alternative estimation could be executed by scaling up the template(sample generated from MC not in full statistics) from MC. In the case of the two analyses presented in this thesis, neither are there enough MC events nor are the shape of the MC event physically reliable. Thus, another class of methods of background estimation needs to be explored, all relying on the "smoothness" feature of the background events. These include the fit function method, the expanded sliding window fit method(SWiFT) and the Gaussian Process method [96]. In the following section, the fit function method, the SWiFT method and the Gaussian Process method are discussed.

6.4.1 Fit Functions/Global Fit

A class of fit functions are used to describe the distribution of the reconstructed mass due to smooth background. The most commonly used forms are cited as the following [97]. The selected fit functions are all resistant to capturing localized excess.

- **Polynomial**

$$f(m) = a_0 + a_1 m + a_2 m^2 + ... \tag{6.1}$$

  Here, m is the resonance mass, and a_i are the different parameters.

- **Power Laws**

$$f(m) = a_0 m^b \tag{6.2}$$

- **Exponentials**

$$f(m) = a_0 e^{-b_0 m} + a_1 e^{-b_1 m} + ... \tag{6.3}$$

From the above foundation, a list of historic fit functions has been developed over the years [98].

$$f(m) = \frac{p_0}{m^{p_1}} e^{-(p_2 m + p_3 m^2)} \tag{6.4}$$

See [99] for details.

$$f(m) = \frac{p_0}{m^{p_1}}(1 - \frac{m}{\sqrt{s}})p_2 \tag{6.5}$$

See [100] for details.

$$f(m) = \frac{p_0}{m^{p_1}}(1 - \frac{m}{\sqrt{s}}+)p_2 \tag{6.6}$$

See [101] for details.

$$f(m) = p_0(1-x)_1^p x^{p_2+p_3 ln(x)} \tag{6.7}$$

See [102] for details.

$$f(m) = (1-x)^{p_0} x^{p1+p2ln(x)} \tag{6.8}$$

See [103] for details.

In these fit functions, m is the resonance mass, p are the parameters, and x is defined to be $\frac{m}{\sqrt{s}}$.

Cross-validation

K-fold cross validation is often used to ensure the fit function is chosen correctly. In the procedure, the original dataset is divided into k different equal event size subsets through a random draw from the original dataset. Each of these subsets is tested by the candidate fit function and validated on the validation set. The best fit is chosen by averaging the p-value of the fit test statististic, χ^2/NDF. The best fit is defined to have a p-value of the closest to 0.5.

While the fit function is relatively easy to implement, it is highly restrictive for complicated background shapes since it is low in flexibility [97]. Making the background modelling on data inaccurate. When the increased luminosity of the LHC dataset leads to difficulties in fitting the background accurately, SWiFT and Gaussian Process are developed for the challenge.

6.4.2 Sliding window fit(SWiFT)

When the simple fit function failed to model the data, SWiFT can increase the fit flexibility and the degree of freedom by fitting multiple narrower windows rather than the entire spectrum. The SWiFT window fitting procedure is summarized as below:

1. A global fit is performed in the overall spectrum. Only when the overall χ^2 p-value is below 0.01, SWiFT is attempted. Otherwise, the procedure ends in this step and a global fit method will be used.

2. The SWiFT fit will start with the maximum sized window, which is the number of bins of the entire spectrum minus one. The window scan starts from the lowest mass region along the spectrum. A fit is performed in the window. This estimates the spectrum up to the middle point of the window.

3. The window moves up by one bin along the resonance mass spectrum. Another fit is performed. The prediction up to the middle of the window is piece-wise appended to the prediction in step 2.

4. Step 3 is repeated, until the end of the spectrum is reached. The final fit is checked against the threshold p-value of the χ^2. If the fit χ^2 is below the designated threshold, the background estimation ends. Otherwise, the window size is further reduced by one bin, and step 2 and 3 are repeated until either a fit with a Bumphunter p-value 0.01 is found or the minimum window size is reached. The minimum window size is defined by the signal injection test discussed below.

While the SWiFT can provide extra flexibility to the fit for better accuracy, it is also prone to becoming too flexible. Signal present in the data could be estimated as part of the background model. This would lead to diminished signal sensitivity. To provide the most accurate background prediction while balancing signal sensitivity, SWiFT always aims to use the largest window possible that can still accurately describe the background.

To aid the use of the largest window possible, the SWiFT window size is not selected until the data is unblinded. A carefully designed unblinding procedure is required to select the optimal window size for the estimation. Figure 6.2 shows a sample unblinding procedure, as used in the dijetISR resolved analysis presented in Chapter 7.

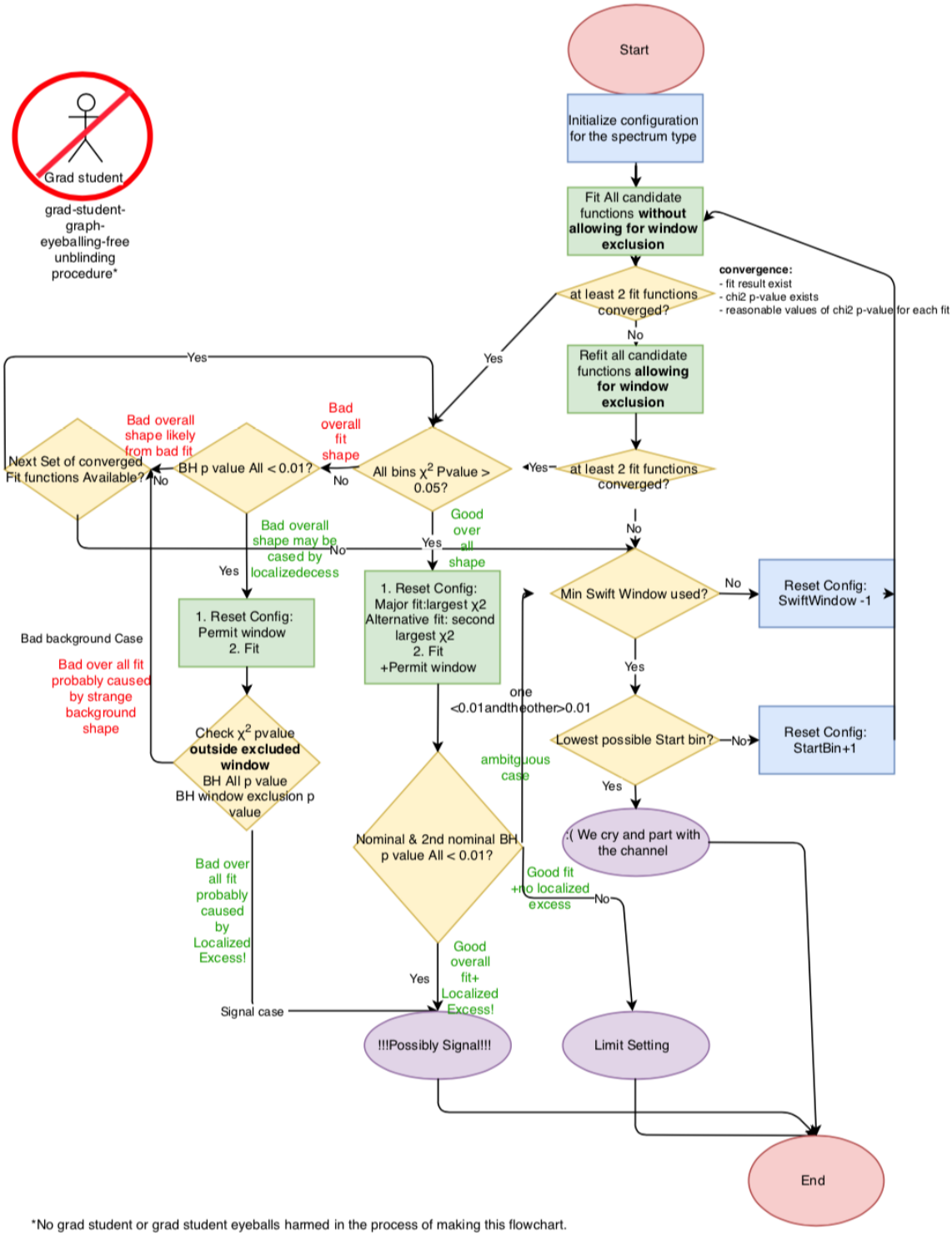

Figure 6.2: This figure shows a doodle on the procedure on the unblinding using SWiFT.

6.4.3 Gaussian Process

A Gaussian Process is a "collection of random variables, any finite number of which have a joint Gaussian distribution" [104]. Gaussian process background prediction is performed through Bayesian inference, where the data point provided improves the prediction in a probability distribution. The mean function of the final probability distribution is taken to be the estimate. Unlike the above fit function-based method, Gaussian Process predicts an infinite number of functional forms, constrained by a kernel(See Section 6.4.3), which defines the bin-to-bin covariance.

Gaussian process can naturally be applied to the background estimation of a spectrum since the bin event count the resonance mass distribution are approximatedly a Gaussian distribution in each bin: the prediction in every bin is a Poisson distribution due to its counting experiment nature. Poissonian distributions can be approximately described as a Gaussian Distribution through the Central Limit Theorem [105]. The Gaussian process allows for more flexibility in the functions compared to the above two methods, as can be shown here in this covariance matrix diagram:

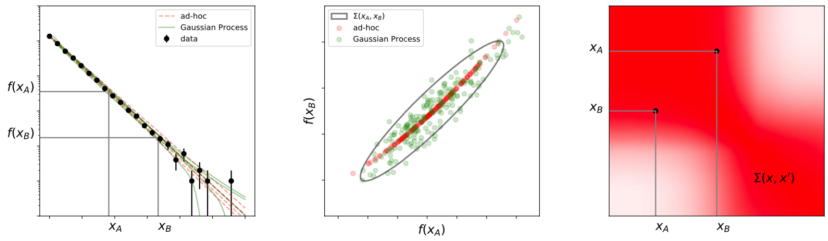

Figure 6.3: These figure shows that the Gaussian process fit is able to provide more flexibility than the standard fit function method. The Red line in the first panel shows results from the fit function method and the green line shows the extra flexibility gained by Gaussian Process. The second pane shows that the possible value of the fit functions are relatively constricted (in red) compared to the Gaussian Process prediction (green) when the prediction are sampled at point X_A and X_B. The black line shows the covariance matrix. The third pane shows the Covariant matrix of the kernel, where X_A and X_B are labeled. [96].

Gaussian Process: Regression

The Gaussian process background prediction result in a joint probability distribution on the count in each bin. The mean function of this probability distribution is the background estimation prediction. The covariance matrix from it is the GP prediction uncertainty.

- **The Mean Function**

$$\mu(x_*|y) = \mu(x_*) + K(x_*, x)[K(x, x) + \sigma^2(x)I]^{-1}(y - \mu(x)) \tag{6.9}$$

Here, $\mu(x_*|y)$ is the mean function posterior prediction of of point x_*, given known data point x and y, K is the kernel, I is the diagonal matrix, σ is the white noise term in each bin. $\mu(x_*)$ is the prior probability distribution mean. x is a vector of the input mass point, and $x^{'}$ are the same points in a 2d matrix. y is the corresponding data count in each mass point x. x' is the vector of same points as x in a 2d matrix. x_* is the vector of the points where the background prediction are evaluated.

- **The Covariance Function**

$$\sum(x_*, x_*^{'}) = K(x_*, x) - ((K(x_*, x^{'}) + \sigma^2 I)^{-1)}[K(x, x^{'})] \tag{6.10}$$

Here, the covariance is defined for x_* and $x_*^{'}$.

Gaussian Process: the Kernel

From Eq. 6.10, kernel is directly related to the covariance function in Gaussian Process. Various kernels are used for different analysis backgrounds with distinct features. A specific example to the dijet spectrum is demonstrated in [96]. A more general example is given as below:

- **Background Kernel**

The background kernel is the addition of the Radial Basis kernel function plus the white noise kernel.

$$K_{bkg}(x, x^{'}) = A_1 * exp(-\frac{||x - x^{'}||}{2\sigma_1^2}) * + K_{noise} \tag{6.11}$$

Here, A_1 is the amplitude hyperparameter that describes the size of the kernel, σ_1 is the lengthscale parameter. The noise kernel is a constant diagonal kernel:

$$K_{noise}(x_i, x_j) = \begin{cases} \text{noise level} & \text{if } x_i == x_j, \\ \\ 0 & \text{otherwise.} \end{cases} \tag{6.12}$$

- **Signal Kernel**

The signal kernel is a square centered exponetial kernel

$$K(x_i, x_j) = A_2 \cdot exp(-(x - m)^2/(2 \cdot \sigma_2^2)) \cdot exp(-((x^{'} - m)^2/(2 \cdot \sigma_2^2))) + K_{noise} \tag{6.13}$$

Here, A_2 is the amplitude of the signal kernel, m is the value where the kernel peaked on, and σ_2 is the lengthscale of the signal kernel.

Of all the hyperparameters, the lengthscales(σ_1 and σ_2) are given special attention as its value descirbes how much neighboring points affect prediction at any given point. It is prone to take on a low value and overfit the data being predicted. Their special treatment are described in the following sections.

Gaussian Process: Hyperparameter Optimization

Kernels are parametetrized by hyperparameters. Hyperparameters are higher level parameters that controls and aid the learning of the process through input of data. The lengthscale hyperparameter, with its special nature, has a lower bound, found through the signal injection test described in [97]. Other hyperparameters are not bounded. The minimization of the hyperparameters is performed through a scalar conjugate gradient search. To avoid reaching a local minimum, the initial values of the hyperparameters are chosen through a grid. The minimized hyperparameter are compared to the other sets with different initial values. The set of hyperparameters with the overall lowest negative log likelihood is chosen to be the optimal hyperparameters.

$$-\ln(L) = -\frac{1}{2}ln|\sum| - (y-\mu(x)) - \frac{n}{2}\ln(2\pi) \tag{6.14}$$

6.5 Statistics Testing

Statistical testing is the quantification of the significance of any observed excess and the signal sensitivity exclusion presented in the data.

There are two distinct statistics tests in a typical resonance search analysis. The two tests will be referred to as "the search" and the "limit setting". Details are described in the following sections.

6.5.1 The Search

The search aims to look for model independent statistical excesses present in data. This test is implemented in comparison to the null hypothesis, where it is defined to be the Standard Model prediction. The search is implemented in a frequentist manner through the Bumphunter method [106]. This section describes the statistics principle behind this test and details the Bumphunting procedure.

The Search: The Statistics Principles

The probability of having made a measurement in each bin can be described by a probability distribution. As each measurement is considered an independent event in a fixed data-taking period and physical variable value. The probability distribution takes the Poissonian probability distribution form:

$$P(x = k|\lambda) = \frac{\lambda^k e^{-\lambda}}{k!} \tag{6.15}$$

Here, λ is the expected value of the measured quantity k, x is the quality being measured, e is Euler's number.

The test is implemented in a frequentist manner. It compares the observation outcome x with a fixed critical value α of a probability distribution. The distribution is generated from pseudoexperiments. Psuedoexperiments are sample distributions drawn from the the Poissonian probability distribution of each bin. Test statistics can be calculated for each of these distribution. The value used to reject or accept the null hypothesis is quantity that is compared in relation to α called the p-value.

$$P(x \ni w|H_0) <= \alpha \tag{6.16}$$

Here, H_0 is the null hypothesis, and α is the critical value below which an excess will be quoted. The value is usually taken to be 0.01 for the Bumphunter experiment. It corresponds to a probability of 1%. x is the observed value. w is all possible outcomes.

The Search: Test Statistics

The test statistic is a function of the observable x, that describes the agreement between data and the model. The p-value in 6.16 can be rewritten as:

$$p = P(T >= t_0|H_0) \tag{6.17}$$

Here, H_0 is the null hypothesis, t_0 is the test statistic above a certain test value, and T is the observed test statistic.

Equation 6.17 evaluate the p-value of the observed value. T is a function of the observed x in the window. It's the probability of the observed test statistics obtaining a value at least as extreme as

t_0. A small p-value refects a poor agreeement between the observed T value and the hypotheis H_0.

Various test statistics are available to quantify the level of agreement between an observation and a hypothesis. If the test is concerned with overall agreement between data and the model, the χ^2 test or the log-likelihood of the Poissonian distribution are fitting candidates.

The Bumphunter test statistic instead to quantifies localized excess. The test statistic is defined in a window and calculated for the bins within. It is a more powerful test for the kind of deviation expected in resonance hunting.

In a window defined from bin number m to n, the observed data and prediction can be given as the following:

$$d = \sum_{i=m}^{n} d_i \tag{6.18}$$

$$b = \sum_{i=m}^{n} b_i \tag{6.19}$$

Here d is the total number of events in the window observed, where d_i is the count in each of the bins from m to n. Here b is the total number of events in the window predicted, where b_i is the event count in each of the bins from m to n.

Assuming the observed counts in each bin follow a Poissonian distribution, the test statistic is:

$$t^{\mathrm{BH}} = \begin{cases} \sum_{n=0}^{d} \frac{b^n}{n!} e^{-b} & \text{for } d < b \\ \sum_{n=d}^{\infty} \frac{b^n}{n!} e^{-b} & \text{for } b \leq d \end{cases} \tag{6.20}$$

The above expression can be represented by the Gamma function(γ):

$$t^{\mathrm{BH}} = \begin{cases} 1 - \gamma(d+1, b) & \text{for } d < b \\ \gamma(d, b) & \text{for } b \leq d. \end{cases} \tag{6.21}$$

The p-value of the Bumphunter test statistic is evaluated for every windows from two-bin wide to half the spectrum(t^{BH}). The overall Bumphunter test statistic is defined by the to be the log of the smallest p-value calculated from the smallest p-value window, and can be represented as the following(t^{BH}_{min}):

$$t^{\mathrm{BH}}_{min} = -\ln(t^{\mathrm{BH}}_{\mathrm{min}}) \tag{6.22}$$

Significance Z and the p-value can be calculated from this test statistic in Eq. 6.17 and thereby provide the probability that the SM hypothesis could have generated data this unlikely or more.

The Search: The Bumphunting Procedure

The Bumphunting procedure is defined to look for excesses as defined by the Bumphunter statistics [98].

1. First a background model fit is performed. (See Section 6.4). The χ^2 of the fit is verified to have a p-value > 0.01. Otherwise, the fit will be revised or moved to an alternative method.

2. If the background fit passes the χ^2 test, the Bumphunting test can begin. In all defined windows, Bumphunter test statistic and their p-values are calculated. If the overall Bumphunter test statistic has a p-value above 0.01, the procedure stops, no excess is found. Alternatively, if any one of the windows has $p < 0.01$, the window most discrepant window (the window with the lowest p-value) is removed, and the fit is reperformed. If the new fit with the window removed has a p-value above 0.01, it shows the discrepancy is completely contained in the window removed.

3. After reperforming the fit with the window removed, if an overall Bumphunter statistics p-value is found to be over 0.01, the procedure stops. A local discrepancy may have been discovered in the removed window. Otherwise, if the newly discovered most discrepant window is adjacent to the window removed, it demonstrates that the signal peak may still be outside of the window, one more bin of window exclusion will be added to the removed window. If the newly discovered most discrepant window is not adjacent to the window removed, one bin of each side is added to the original removed window. The fit is re-performed with the new window removed. This step is repeated until either the p-value of the fit with the removed window has a p-value above 0.01, or no additional window could be added to the exclusion because all bins has been added to the removal window.

Summarizing from the above, three end results are possible in the search test:

1. If no window is excluded and the fit has a Bumphunter p-value statistics above 0.01. No excess is found.

2. If there is one excluded window and a background fit with a Bumphunter statistics p-value of above 0.01. An excess up to a certain significane is quoted.

3. In all other scenarios, more tests are required. The background model fit could be problematic and need further testing.

6.6 Limit Setting

The limit setting can be performed in two different ways, the Bayesian statistical way and the frequentist way. While the interpretation and implication of the results made with the different methods are different, the results produced are designed to be comparable across different analyses.

The Bayesian method is used for the dijetISR analysis(Chapter 7) and the frequentist method is used for the dimuon analysis(Chapter 8). A summarized formuation of the frequentist limit is given as below.

6.6.1 Frequentist Limits

The following subsection describes the test statistics used for the limit setting. A formulation of the traditional frequentist calculation is presented. The Asimov approximation method used to approximate the frequentist limit from a representative dataset is described, which is the ATLAS standard, and it saves computing resources. The formulae for the limit calculation using this method are given. Adaptation with the Gaussian Process is also discussed.

Frequentist Limits: The Test Statistics

The probability distribution of the observable x in each bin of the histogram can be given by a Poissonian probability distribution. This probability distribution is a function of many parameters, including the signal strength, and other systematic uncertainty parameters, for example, the variation in luminsoity. As these variable are not the target parameter where limit is set, they are known as the nuissance paramters. From the Poissonian distribution, its likelihood function can be parameterized as such, with the predicted signal event and background events made explicit:

$$L(\mu,\theta) = \prod_{i=0}^{N} \frac{(\mu \cdot s_j + b_j)^{n_j}}{n_j!} e^{(-\mu \cdot s_j + b_j)} \prod_{k=1}^{M} \frac{u_k}{m_k!} e^{(-u_k)} \tag{6.23}$$

Here, L is the likelihood product from the target distribution multiplied by systematic parameter distributions, μ is the signal strength, s_j is the number of expected signal events in the jth bin, b_j is the number of expected background events in the jth bin, n_j is the number of observed events in each bin; N is the total number of bins. The likelihood is also affected by variations in other parameters, which include sysmstatic uncertainty terms such as imprecise luminosity measurement or energy correction uncertainties. These are not the targeted signal strength and are often known as the nuissance parameters. here, u_k is the predicted value by the model, and m_k is the observed

value.

The most probable value of the parameters are those that maximize the likelihood function. However, since in limit setting, the only parameter we are interested in learning about is the signal strength, the influence from the unknown true value of the nuisance parameters can be taken into account or eliminated. As optimizing the true likelihood is often computationally expensive, a "profiled likelihood" function is constructed. This quantity, when maximized, gives the same effect as maximizing the true likelihood.

$$\lambda(\mu) = \frac{L(\mu, \hat{\hat{\theta}})}{L(\hat{\mu}, \hat{\theta})} \tag{6.24}$$

Here, $\hat{\hat{\mu}}$ ands $\hat{\hat{\theta}}$ are the values that maximizes L for μ specified. the denominator is the maximized unconditional likelihood function, where $\hat{\mu}$ and $\hat{\theta}$ are the parameter values that would maximize the unconditional likelihood function regardless of specific μ values.

To aid the optimization process, it is usually the negative log of the profiled likelihood that is used for the limits calculation:

$$q_\mu = -2 \ln \frac{L(\mu, \hat{\hat{\theta}})}{L(\hat{\mu}, \hat{\theta})} \tag{6.25}$$

The Frequentist Limits: The Limits Formulae

The formulae for the limits calculation is given below:

- **The Observed 95% Upper Limit**

$$\mu_{up/lo} = \hat{\mu} + -\sigma \Phi^{-1}(1 - \alpha/2) \tag{6.26}$$

  here, μ is the signal strength, up/lo is the upper or the lower 5% confidence limit.

- **The Expected Median Limit**

$$\text{med}[\mu_{up}|\mu'] = \mu' + \sigma \Phi^{-1}(1 - \alpha) \tag{6.27}$$

  here, μ' is the expected signal strength.

  here, med is the median of the observed limits.

- **The Expected Limits Significance**

$$\text{band}_{N\sigma} = \mu' + \sigma(\Phi(1-\alpha) + -N) \tag{6.28}$$

Here, μ is the signal strength being considered, α is the significance associated with 95% confidence and the median significance respectively, Φ is the cumulative Gaussian distribution where the observed p-value lies.

Note that the calculation of the denominator in 6.23 is CPU-intensive, and can be approximated.

The Frequentist Limits: The Asymptotic distribution

From the Wald theorem, the test statistic can be approximated:

$$-2\ln(\lambda(\mu)) = \frac{(\mu-\hat{\mu})^2}{\sigma^2} + O(1/\sqrt{N}) \tag{6.29}$$

Here, μ is the observed value, whereas the $\hat{\mu}$ is the expected strength that would maximize the likelihood, σ is the expected spread in the distribution.

If the terms in O are neglected, the test statistic will then asymtotically follow a non-central chi-square distribution, derivation is in [107]:

$$f(q_\mu) = \frac{1}{2\sqrt{q_\mu}}\frac{1}{\sqrt{2\pi}}[exp(-\frac{1}{2}(\sqrt{q_\mu}+\sqrt{\Lambda}) + exp(-\frac{1}{2}(\sqrt{q_\mu-\sqrt{\Lambda}})^2)] \tag{6.30}$$

Here, Λ is the non-centrality term, it can be shown that it can be estimated to be:

$$\Lambda = 2\ln(\lambda_A(\mu)) \tag{6.31}$$

Where λ_A is the likelihood calculated from the asymtotic distribution. A detailed proof can be found in [107].

Frequentist Limit: The Asimov dataset

The finding of $\hat{\mu}$ in the denominator in 6.25 is CPU intensive. The dataset is large with many dimensions. The Asimov dataset reduces the calculation here by showing that $\hat{\mu}$ can be approximated by μ', the expected value of the strength parameter. From this, CPU intensive calculation of the

p-value can be avoided. Significance and thus the upper limit and the observed limit fluctuation can be reduced to simple formulae that only require calculations from the representative Asimov dataset. A proof is given in the following section, and the formulae used for the upper limit and expected limit calculation in this thesis are included in the end.

Below are the results quoted from [107], a detailed derivation can be found there.

- **The Test Statistics Distribution**

$$F(t_\mu|\mu) = 2\Phi(\sqrt{t_\mu}) - 1 \tag{6.32}$$

  Here F is the distribution of the statistics, t_μ is the test statistic at the given μ value of the distribution.

- **The P-value of a Hypothesized μ for an Observed Value t_μ**

$$p_\mu = 1 - F(t_\mu|\mu) = 2(1 - \Phi(\sqrt{(t_\mu)})) \tag{6.33}$$

- **The Significance**

$$Z_\mu = \Phi^{-1}(1 - p_\mu) = \Phi^{-1}(2\Phi(\sqrt{t_\mu}) - 1) \tag{6.34}$$

From this calculation, the limit calculation in the above Section 6.6 can be utilized for a limit calculation.

Frequentist Limits: Gaussian Process Adaptations

The Gaussian process has been shown to be able to be incorporated within the Asimov method of frequentist limit setting [96]. In Figure 6.4, the likelihood ratio in the Gaussian process 6.35 is a proxy for the profile likelihood ratio used in the Asimov limit. The likelihood came from the 6.14 in the Gaussian Process section above. It can be seen that it approximately follows the χ^2 distribution, satisfying a requirement that follows from the Wald approximation that allows for the Asimov approximation of limits.

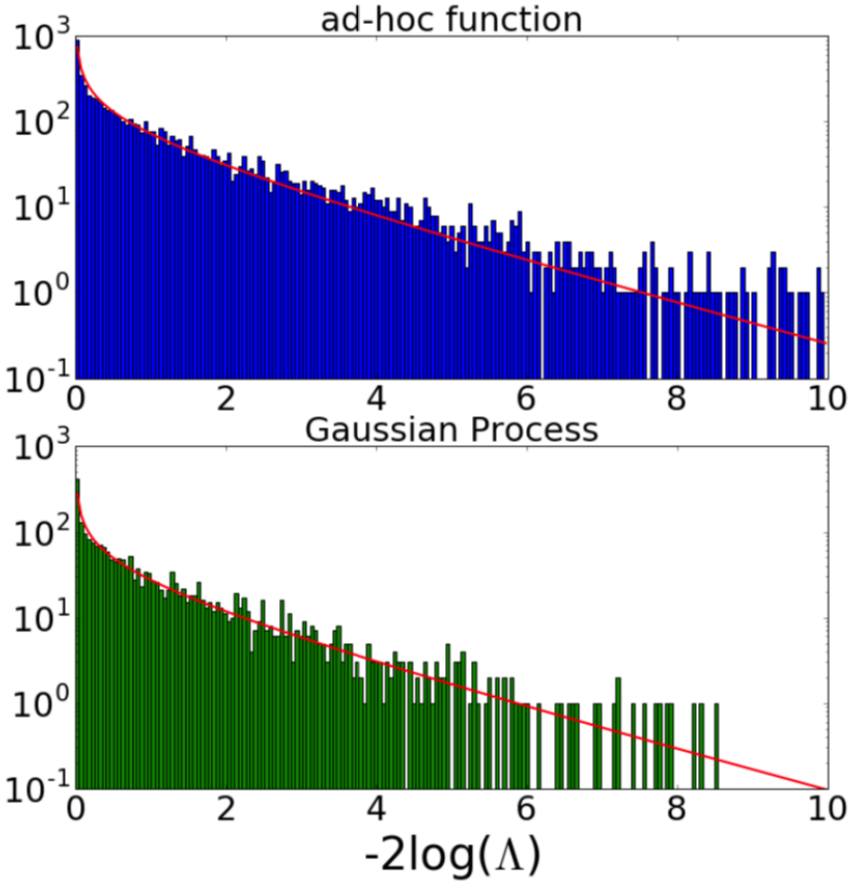

Figure 6.4: This figure shows the negative log of the Λ which is an approximation of the measure of the profiled likelihood ratio defined in 6.24. The top part is the distribution for background only pseudo-experiments, whereas the bottom is the background and signal distribution. They show a reasonable agreement to the χ^2 fit, a required condition for the Asimov approximation for a frequentist limit setting [96].

A new test statistic for Gaussian Process that is parametrized by the kernel hyperparameters is used instead for limit setting:

$$-ln(\Lambda), \text{ where } \Lambda = \frac{L_{\text{GP signal + bkg fit}}(\mu, \hat{\hat{\theta}})}{L_{\text{GP bkg fit}}(\hat{\mu}, \hat{\theta})}) \tag{6.35}$$

Here, $\ln(\Lambda)$ is the new test statisitics used for the limit setting L is the likelihood defined in Eq. 6.14. The numerator is the likelihood with both the background and signal kernel, whereas the denominator is likelihood with just the background kernel.

With the above procedure in place, actual data from analysis is ready to be analyzed for resonance

in the dijetISR and dimuon channels.

Chapter 7

Search for Resonances in the Resolved Dijet Final State with an Initial State Radiation

It is our perpetual dissatisfaction with ourselves that causes us to approach the world as a space of possibility that has the power to awaken our attention and make us marvel at its vibrant details.

— Mari Ruti, A World of Fragile Things: Psychoanalysis and the Art of Living

This chapter is heavily based on work previously published [108]in collaboration with ATLAS.

7.1 Introduction

Searches for resonant enhancements of the dijet invariant mass distribution (m_{jj}) are an essential part of the LHC physics programme. New particles with sizeable couplings to quarks and gluons are predicted by many models, such as those including resonances with additional couplings to dark-matter particles [109, 110].

Searches for dijet resonances with masses of several hundreds of GeV to just above 1 TeV have been carried out at lower-energy colliders [111, 112, 113, 114, 115] and at the LHC, which has also extended search sensitivities into the multi-TeV mass range [116, 117, 118, 119, 120, 121, 122, 123, 124, 125, 126, 127, 128, 129, 130]. Despite using higher integrated luminosities than earlier colliders, these LHC searches have been limited at lower masses by a large multi-jet background. Multi-jet events are produced at such high rates that fully recording every event would saturate

the online data selection (called *trigger*) and data acquisition systems. To avoid this, minimum transverse momentum ($p_{\mathrm{T}}^{\mathrm{min}}$) thresholds are imposed on triggers collecting events with at least one jet (called single-jet triggers). These thresholds create a lower bound on the sensitivity of searches at a mass of approximately $m_{\mathrm{jj}} \approx 2p_{\mathrm{T}}^{\mathrm{min}}$, where $p_{\mathrm{T}}^{\mathrm{min}}$ is typically several hundred GeV. Consequently, searches for dijet resonances at the LHC have poor sensitivity for masses below 1 TeV, and set limits on the couplings of the resonance to quarks in this light-resonance region which are weaker than limits in heavy-resonance regions [131]. Nevertheless, despite the difficulty of recording events containing light resonances, they remain a viable search target at the LHC, both from a model-agnostic point of view [132] and, for example, in models of spin-dependent interactions of quarks with dark matter [109, 110].

Recently, ATLAS and CMS have published searches for low-mass dijet resonances using several complementary strategies to avoid trigger limitations. For $m_{\mathrm{jj}} > 450\,\mathrm{GeV}$, the most stringent limits are set by searches recording only partial event information [128, 129].

Another search avenue is opened by data in which a light resonance is boosted in the transverse direction via recoil against a high-p_{T} photon [133, 134]. Requiring a high-$p_T$photon in the final state reduces signal acceptance but allows efficient recording of events with lower dijet masses. At even lower resonance masses, the decay products of the resonance will merge into a single large-radius jet. Searches for this event signature have been used to set limits on resonant dijet production at both ATLAS [135] and CMS [136, 137]. However, these searches become less sensitive above 200 GeV–350 GeV, when the decay products fall outside the large-radius jet cone.

This chapter presents a new search for resonances in events containing a dijet and a high-$p_T$photon in the final state, using proton–proton (pp) collisions recorded at a centre-of-mass energy $\sqrt{s}$ = 13 TeV and corresponding to an integrated luminosity up to 79.8 (ifb). The search targets a dijet mass range of 225 GeV–1.1 TeV. This range covers masses below the range accessible using single-jet triggers or partial-event data and above the mass range where the resonance decay products merge. The search is performed using samples of events selected either with or without criteria designed to identify jets originating from bottom quarks (*b-jets*). Searching in a subset of the data selected with b-jet identification criteria enhances sensitivity to resonances which preferentially decay into bottom quarks. This search probes masses above 225 GeV, obtaining results complementary to the reach of previous dijet searches at a centre-of-mass energy of $\sqrt{s}$ = 13 TeV: below approximately 600 GeV, previous ATLAS di-b-jet searches lose sensitivity [138], while the range of the CMS boosted di-b-jet search [137] is limited to a mass region up to 350 GeV. Another complementary CMS search for resonances with masses above 325 GeV decaying to b-jets at a centre-of-mass energy of $\sqrt{s}$ = 8 TeV is described in Ref. [139].

7.2 Data samples and event selection

The result presented in this chapter is based on data collected in pp collisions at $\sqrt{s}$ = 13 TeV during 2015–2017. The signal consists of events with two jets from the decay of a new particle, and an additional photon, radiated off one of the colliding partons.

Data were collected via either a single-photon trigger or a combined trigger requiring additional jets, to allow a lower $p_T$requirement on the photon. The data collected with the single-photon trigger are used to search for resonances with masses from 225 GeV to 450 GeV, while the data collected with the combined trigger are used to search for resonances with masses from 450 GeV to 1.1 TeV.

The single-photon trigger requires at least one photon candidate with $E^{\gamma}_{\mathrm{T,\,trig}} > 140\,\mathrm{GeV}$, where $E^{\gamma}_{\mathrm{T,\,trig}}$ is the photon transverse energy as reconstructed by the software-based trigger. The combined trigger requires a photon and two additional jet candidates, each with $p_{\mathrm{T}} > 50\,\mathrm{GeV}$. The combined trigger requires $E^{\gamma}_{\mathrm{T,\,trig}} > 75\,\mathrm{GeV}$ for the 2016 data, increasing to $E^{\gamma}_{\mathrm{T,\,trig}} > 85\,\mathrm{GeV}$ for the 2017 data. This trigger was not active during the 2015 data-taking period. As a consequence, the single-photon trigger recorded 79.8 (ifb) of data and the combined trigger recorded 76.6 (ifb) of data. Both triggers are fully efficient within uncertainties in the kinematic regimes used for this analysis.

After recording the data, a subset of collision events consistent with the signal are selected to populate m_{jj} distributions for subsequent analysis. A brief description of the reconstruction methods is given below together with the event selection.

In all of the events selected for analysis, all components of the detector are required to be operating correctly. In addition, all events are required to have a reconstructed primary vertex [140], defined as a vertex with at least two reconstructed tracks, each with $p_T > 500$ MeV.

Photon candidates are reconstructed from clusters of energy deposits in the electromagnetic calorimeter [141]. The energy of the candidate is corrected by applying energy scale factors measured with $Z \to e^+e^-$ decays [142].

The trajectory of the photon is reconstructed using the longitudinal segmentation of the calorimeters along the shower axis (shower depth) and a constraint from the average collision point of the proton beams. Candidates are restricted to the region $|\eta| < 2.37$, excluding the transition region $1.37 < |\eta| < 1.52$ between the barrel and endcap calorimeters to ensure that they arise from well-calibrated regions of the calorimeter. An additional requirement is applied on the transverse energy of the photon candidate after reconstruction, which is required to have $E^{\gamma}_{\mathrm{T}} > 95\,\mathrm{GeV}$, where E^{γ}_{T} is the transverse energy of the photon candidate after reconstruction.

Quality requirements are applied to the photon candidates to reject events containing misreconstructed photons arising from instrumental problems or from non-collision backgrounds. Further *tight* identification requirements are applied to reduce contamination from π^0 or other neutral hadrons decaying into two photons [141]. The photon identification is based on the profile of the energy deposits in the first and second layers of the electromagnetic calorimeter. In addition to the tight identification requirement, candidates must meet *tight isolation* criteria using calorimeter and tracking information, requiring that they be separated from nearby event activity [143, 144]. Converted photon candidates matched to one track or a pair of tracks passing inner-detector quality requirements [141] and satisfying tight identification and isolation criteria are also considered. Any pair of matching tracks must form a vertex that is consistent with originating from a massless particle.

Jets are reconstructed using the anti-k_t algorithm [145, 146] with radius parameter $R = 0.4$ from clusters of energy deposits in the calorimeters [147]. Quality requirements are applied to remove events containing spurious jets from detector noise and out-of-time energy deposits in the calorimeter from cosmic rays or other non-collision sources [148]. Jet energies are calibrated to the scale of the constituent particles of the jet and corrected for the presence of multiple simultaneous (pile-up) interactions [149, 150].

After reconstruction, jets with transverse momentum $p_{\mathrm{T}}^{\mathrm{jet}} > 25\,\mathrm{GeV}$ and rapidity $|\eta^{\mathrm{jet}}| < 2.8$ are considered. To suppress pile-up contributions, jets with $p_{\mathrm{T}}^{\mathrm{jet}} < 60\,\mathrm{GeV}$ and $|\eta^{\mathrm{jet}}| < 2.4$ are required to originate from the primary interaction vertex with the highest summed p_T^2 of associated tracks. If a jet and a photon candidate are within $\Delta R = 0.4$, the jet candidate is removed.

These requirements retain approximately 30% of a typical signal sample.

Jets which likely contain b-hadrons are identified (b-tagged) with the DL1 flavour tagger [151]. Tracks are selected in a cone around the jet axis, using a radius which shrinks with increasing $p_{\mathrm{T}}^{\mathrm{jet}}$. The selected tracks are used as input to algorithms which attempt to reconstruct a b-hadron decay chain. The resulting information is passed to a neural network which assigns a b-jet probability to each jet. To account for mismodelling in simulated b-hadron decays, a comparison of the discrimination power of this network in data and Monte Carlo simulation is performed and correction factors are applied to simulation to reproduce the data [152]. Jets are considered b-taggedwhen the DL1 score exceeds a threshold consistent with a 77% b-hadron identification efficiency on a benchmark $t\bar{t}$ sample. At this threshold, only 0.7% light-flavour jets and 25% charm-jets are retained.

Events which contain at least one photon candidate and two jets are selected using the above criteria and separated into four categories for further analysis. Two of the categories are constructed with flavour-inclusive criteria, for which b-tagging results are ignored. One of these two categories contains events recorded via the single-photon trigger, and the other category contains events recorded via the combined trigger. To ensure the trigger is fully efficient, events in the single-photon-

trigger category are required to have a photon with $E_{\mathrm{T}}^{\gamma} > 150\,\mathrm{GeV}$ and events in the combined-trigger category are required to have a photon with $E_{\mathrm{T}}^{\gamma} > 95\,\mathrm{GeV}$ and two jets with $p_{\mathrm{T}}^{\mathrm{jet}} > 65\,\mathrm{GeV}$. The remaining two categories consist of events selected as in the flavour-inclusive categories, except that the two highest-$p_{\mathrm{T}}^{\mathrm{jet}}$ jets must satisfy the b-tagging criteria and have $|\eta^{\mathrm{jet}}| < 2.5$ to ensure that they fall within the acceptance of the tracking detectors.

Dijet production at the LHC occurs largely via t-channel processes, leading to jet pairs with high absolute values of $y^* = (y_1 - y_2)/2$, where y_1 and y_2 are the rapidities of the highest-p_T (leading) and second-highest-p_T (subleading) jet, respectively. On the other hand, heavy particles tend to decay more isotropically, with the two jets having lower $|y^*|$ values. Therefore, $|y^*| < 0.75$ is required for all four categories. This selection rejects up to 80% of the multi-jet background events while accepting up to 80% of the signal events discussed below. A further selection is applied to select events above a given invariant mass depending on the trigger, $m_{\mathrm{jj}} > 169$ GeV for the single-photon trigger and $m_{\mathrm{jj}} > 335$ GeV for the combined trigger. This is so that the background can be described by a smoothly falling analytic function satisfying the goodness-of-fit criteria described in 7.3.

Table 7.1: Event selections used to construct each of the four event categories, as described in the text.

Criterion	Single-photon trigger	Combined trigger
Number of jets	$n_{\mathrm{jets}} \geq 2$	
Number of photons	$n_{\gamma} \geq 1$	
Leading photon	$E_{\mathrm{T}}^{\gamma} > 150$ GeV	$E_{\mathrm{T}}^{\gamma} > 95$ GeV
Leading, subleading jet	$p_{\mathrm{T}}^{\mathrm{jet}} > 25$ GeV	$p_{\mathrm{T}}^{\mathrm{jet}} > 65$ GeV
Centrality	$\lvert y^* \rvert = \lvert y_1 - y_2 \rvert / 2 < 0.75$	
Invariant mass	$m_{\mathrm{jj}} > 169$ GeV	$m_{\mathrm{jj}} > 335$ GeV
Criterion (applied to each trigger selection)	**Inclusive**	**b-tagged**
Jet $\lvert\eta\rvert$	$\lvert\eta^{\mathrm{jet}}\rvert < 2.8$	$\lvert\eta^{\mathrm{jet}}\rvert < 2.5$
b-tagging	–	$n_{b\text{-tag}} \geq 2$

The above selections, summarised in Table 7.1, yield 2,522,549 and 15,557 events acquired by the single-photon trigger for the flavour-inclusive and b-taggedcategories, respectively. They yield 1,520,114 and 9,015 events acquired by the combined trigger in the corresponding categories.

The distributions of m_{jj} for events in each of the four categories are shown in Fig. 7.1. Hypothetical signals with $m_{Z'} = 250\,\mathrm{GeV}$ and $m_{Z'} = 550\,\mathrm{GeV}$, as further discussed in Section 7.5, are overlaid.

At the largest dijet masses considered, the combined-trigger categories provide greater sensitivity to signals than the single-photon-trigger categories due to their greater signal acceptance. The sensitivity is defined as $S/\sqrt{B}$, where S and B are the number of signal and background events in the simulation samples described in Section 7.5. At the smallest dijet masses considered, the jet p_T

thresholds of the combined trigger cause those categories to lose efficiency for signals and bias the m_{jj} distributions of the background processes. Therefore, to optimise the search across a wide range of signal masses, the invariant mass spectra selected using the combined-trigger categories are used in the search for signal masses above 450 GeV, while the spectra obtained with the single-photon trigger are used for lower masses.

7.3 Background estimation

To estimate the Standard Model contributions to the distributions in Fig. 7.1, smooth functions are fit to the data. The dijet searches of the CDF, CMS, and ATLAS experiments [114, 116, 119, 123, 125, 125, 123, 115, 128] have successfully modelled dijet mass distributions in hadron colliders using a single function over the entire mass range considered in those searches. This approach is not suitable when data constrain the fit too tightly for a single function to reliably model both ends of the distribution simultaneously. Here, a more flexible technique is adopted, similar to that used in recent ATLAS dijet resonance searches [130, 129]. In this technique, a single fit using a given function over the entire mass distribution is replaced by many successive fits. For each bin of the mass distribution, the same function is used to fit a broad mass range centred on the bin, and the background prediction for that bin is taken to be the value of the fitted function in the centre of the range. The process is repeated for each bin of the mass distribution and the results are combined to form a background prediction covering the entire distribution. For invariant masses higher than the m_{jj} range used for the search (above 1.1 TeV), the window is allowed to extend beyond the range as long as data is available.

A set of parametric functions are considered for these fits:

$$f(x) = p_1 x^{-p_2} \mathrm{e}^{-p_3 x - p_4 x^2} \tag{7.1}$$

or

$$f(x) = p_1 (1-x)^{p_2} x^{p_3 + p_4 \ln x + p_5 (\ln x)^2}, \tag{7.2}$$

where $x = m_{\mathrm{jj}}/\sqrt{s}$ and p_i are free parameters determined by fitting the m_{jj} distribution. In addition to the five-parameter function in Eq. (7.2), a four-parameter variant with $p_5 = 0$ and a three-parameter variant with $p_5 = p_4 = 0$ are also considered. The width of the mass range used for the individual fits was optimised to retain the broadest possible range while maintaining a χ^2 p-value above 0.05 in regions of the distribution that do not contain narrow excesses, where excesses are

identified using the BumpHunter algorithm described in the next section. The sliding window procedure cannot be extended beyond the lower edge of the m_{jj} range used in each signal selection. Therefore, until the optimal number of bins is reached on each side of a given bin center, the start of the window is fixed to the lower edge of the spectrum and the fitted functional form is evaluated for each bin in turn. This procedure allows for a stable background estimate while maintaining sensitivity to signals localised in the m_{jj} distribution. Tests performed by adding sample signals to smooth pseudo-data distributions confirmed that this approach can find signals of width-to-mass ratios up to 15%, with sensitivity increasing for narrower signals. The ranges of the individual fits vary from 750 GeV in the narrowest case to 1600 GeV in the widest case. A signal with a 15% width-to-mass ratio constrained by the narrowest fit would have an absolute width of 163 GeV, or less than one quarter of the fit range.

Monte Carlo samples of background containing a photon with associated jets were simulated using Sherpa 2.1.1 [153], generated in several bins of photon transverse momentum at the particle level (termed as E_{T}^{γ} for this paragraph), from 35 GeV up to energies where backgrounds become negligible in data, at approximately 4 TeV. The matrix elements, calculated at next-to-leading order (NLO) with up to three partons for $E_{\mathrm{T}}^{\gamma} < 70$ GeV or four partons for higher E_{T}^{γ}, were merged with the Sherpa parton shower [154] using the ME+PS@LO prescription [155]. The CT10 set of parton distribution functions (PDF) [156] was used in conjunction with the dedicated parton shower tuning developed by the Sherpa authors. These samples, alone and in combination with the signal samples discussed below, were used to validate the background model obtained with the above mentioned method, and they were also used to verify that the fitting procedure is robust against false positive signals. Additionally, the simulated samples were used to calculate the fractional dijet mass resolution, which was found to be in the range 8%–3% for the masses of 225 GeV up to 1.1 TeV considered in this search.

7.4 Search results

Fig. 7.1 shows the results of fitting each of the observed distributions, as described in Section 7.3. For each distribution, the function among those in Eqs. (7.1) and (7.2) and their variants which yields the highest χ^2 p-value (shown in the figure), in absence of localized excesses, is chosen as the primary function for the fitting method. The function with the lowest χ^2 p-value which still results in a p-value larger than 0.05 is chosen as an alternative function. The primary and alternative functions for each of the four search categories are shown in Table 7.2. The alternative function is used to estimate the systematic uncertainty of the background prediction due to the choice of function, as described below.

The statistical significance of any localised excess in each m_{jj} distribution is quantified using the

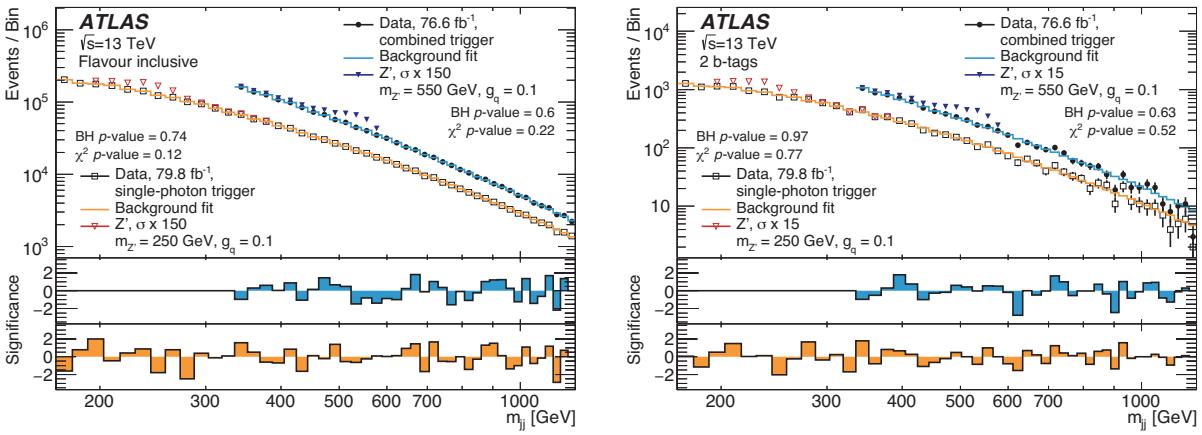

(a) (b)

Figure 7.1: Dijet mass distributions for the a flavour-inclusive and b b-taggedcategories. In both figures, the distribution for the sample collected using the combined trigger with $E_{\mathrm{T}}^{\gamma} > 95\,\mathrm{GeV}$ and two $p_{\mathrm{T}}^{\mathrm{jet}} > 25\,\mathrm{GeV}$ jets (filled circles) and the distribution for the sample collected using the single-photon trigger with $E_{\mathrm{T}}^{\gamma} > 150\,\mathrm{GeV}$ (open squares) are shown separately. The solid lines indicate the background estimated from the fitting method described in the text. Also shown are the p-values both by a χ^2 comparison of data to background estimate and by BumpHunter (BH). The solid and empty triangles represent a Z' injected signal with $g_{\mathrm{q}} = 0.1$, masses of 550 and 250 GeV, respectively, where the theory-cross section is multiplied by the factor shown in the legend. The bottom panels show the significances of bin-by-bin differences between the data and the fits for the combined trigger (middle) and single-photon trigger (bottom). These Gaussian significances are calculated from the Poisson probability, considering only statistical uncertainties on the data.

Table 7.2: Summary of functions used for background fits to each category. The five-parameter function (5 par.) is given in Eq. (7.2). The four-parameter variant (4 par.) sets $p_5 = 0$, while the three-parameter variant (3 par) sets $p_5 = p_4 = 0$.

Fit	Flavour-inclusive, single γ trigger	Flavour-inclusive, combined trigger	b-tagged, single γ trigger	b-tagged, combined trigger.
Primary fit (χ^2 p-value)	Eq. (7.2), 5 par. (0.11)	Eq. (7.2), 4 par. (0.23)	Eq. (7.2), 4 par. (0.75)	Eq. (7.2), 3 par. (0.53)
Alternative fit (χ^2 p-value)	Eq. (7.2), 4 par. (0.07)	Eq. (7.1) (0.20)	Eq. (7.2), 3 par. (0.75)	Eq. (7.2), 5 par. (0.44)

BumpHunter (BH) algorithm [157, 158]. The algorithm compares the binned m_{jj} distribution of the data with the fitted background estimate, considering mass intervals centered in each bin location and with widths of variable size from two bins up to half the mass range used for the search (169 or 335 GeV to 1.1 TeV, for the single and combined trigger respectively).

The statistical significance of the outcome is evaluated using the ensemble of possible outcomes by applying the algorithm to many pseudo-data samples drawn randomly from the background fit. Without including systematic uncertainties, the BumpHunter p-value – the probability that fluctuations of the background model would produce an excess at least as significant as the one observed in the data, anywhere in the distribution – is $p > 0.5$ for all distributions. Thus, there is no evidence of a localised contribution to the mass distribution from new phenomena.

7.5 Limit setting

Limits are set on the possible contributions to the m_{jj} distributions from two kinds of resonant signal processes. As a specific benchmark signal, a leptophobic Z' resonance is simulated as in Refs. [110, 125]. The Z' resonance has axial-vector couplings to quarks and to a fermion dark-matter candidate. The coupling of the Z' to quarks, g_{q}, is set to be universal in quark flavour. The mass of the dark-matter fermion is set to a value much heavier than the Z', such that the decay width to dark matter is zero. The total width $\Gamma_{Z'}$ is computed as the minimum width allowed given the coupling and mass $m_{Z'}$; this width is 3.6%–4.2% of the mass for $m_{Z'}$ = 0.25–0.95 TeV and $g_{\mathrm{q}} = 0.3$. The interference between the Z' in this benchmark model and the Standard Model Z boson is assumed to be negligible. A set of event samples were generated at leading order with $m_{Z'}$ values in the range 0.25–1.5 TeV and with $g_{\mathrm{q}} = 0.3$ using MadGraph5_aMC@NLO 2.2.3 [159]; the NNPDF3.0 LO PDF set [160] was used in conjunction with Pythia 8.186 [161] and the A14 set of tuned parameters [162]. For these samples, the acceptances of the kinematic selections in the flavour-inclusive categories range from 1% to 2.5%, increasing with signal mass, for the sample collected by the combined trigger and from 4% to 10% for the sample collected by the single-photon trigger. For the b-taggedcategories, the kinematic acceptance is defined relative to the full flavour-inclusive generated samples, leading to acceptance values of 0.2%–0.4% and 0.7%–1.6% for the combined and single-photon trigger, respectively. The reconstruction efficiencies range from 74% to 80% for the flavour-inclusive categories and from 40% to 48% for the b-taggedcategories, decreasing with increasing signal mass.

Limits are set on the considered new-physics contributions to the m_{jj} distributions using a Bayesian method. A constant prior is used for the signal cross-section and Gaussian priors for nuisance parameters corresponding to systematic uncertainties. The expected limits are calculated using pseudo-experiments generated from the background-only component of a signal-plus-background

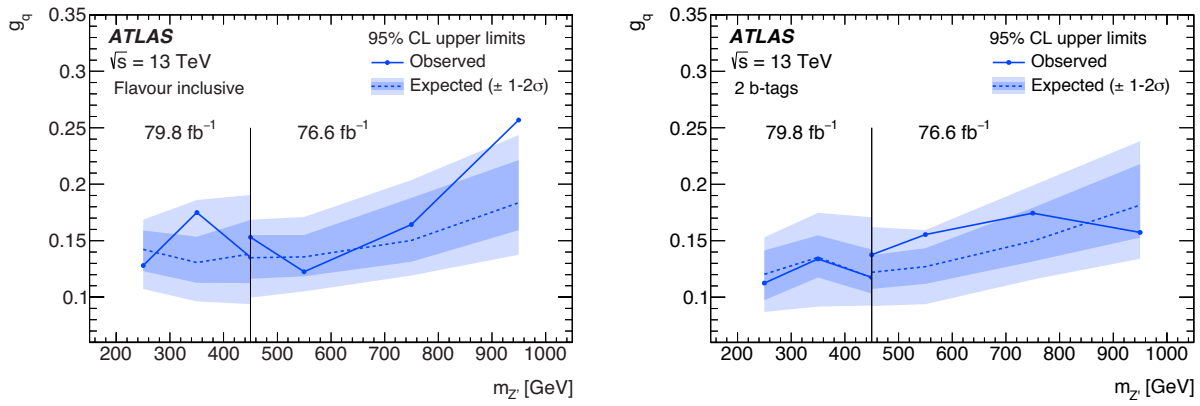

(a) (b)

Figure 7.2: Excluded values of the coupling between a Z' and quarks, at 95% CL, as a function of $m_{Z'}$, from a the flavour-inclusive and b the b-taggedcategories. Below 450 GeV the distribution of events selected by the single-photon trigger is used for hypothesis testing, while above 450 GeV the combined trigger is used.

fit to the data, using the same fitting ranges and functions selected as the best model in the search phase. Signal hypotheses at discrete mass values are used to set 95% credibility-level (CL) upper limits on the cross-section times acceptance [120]. The limits are obtained for a discrete set of points in the g_{q}–$m_{Z'}$ plane, shown in Fig. 7.2.

A more generic set of limits is shown in Fig. 7.3. These limits apply to the visible cross-section from a Gaussian-shape contribution to the m_{jj} distribution, where the visible cross-section is defined as the product of the production cross-section, the detector acceptance, the reconstruction efficiency, and the branching ratio, $\sigma \times A \times \epsilon \times \mathcal{B}$. The Gaussian-shape contributions have mass m_{G} and widths that span from the detector mass resolution, denoted "Res." in the figure, ranging from 8% to 3% for the mass range considered, for an intrinsically narrow resonance, up to 15% of the mean of the Gaussian mass distribution.

Both the choice of fit function and statistical fluctuations in the m_{jj} distribution can contribute to uncertainties in the background model. To account for the fit function choice, the largest difference between fits among the variants of Eq. (7.1) and Eq. (7.2) that obtain a p-value above 0.05, is taken as a systematic uncertainty. The uncertainty related to statistical fluctuations in the background model is computed via Poisson fluctuations around the values of the nominal background model. The uncertainty of the prediction in each m_{jj} bin is taken to be the standard deviation of the predictions from all random samples.

The reconstructed signal mass distributions are affected by additional uncertainties related to the simulation of detector effects. The jet energy scale uncertainty is applied to the Z' mass distributions using a four-principal-component method [150, 163, 164], leading to an average 2% shift of the peak

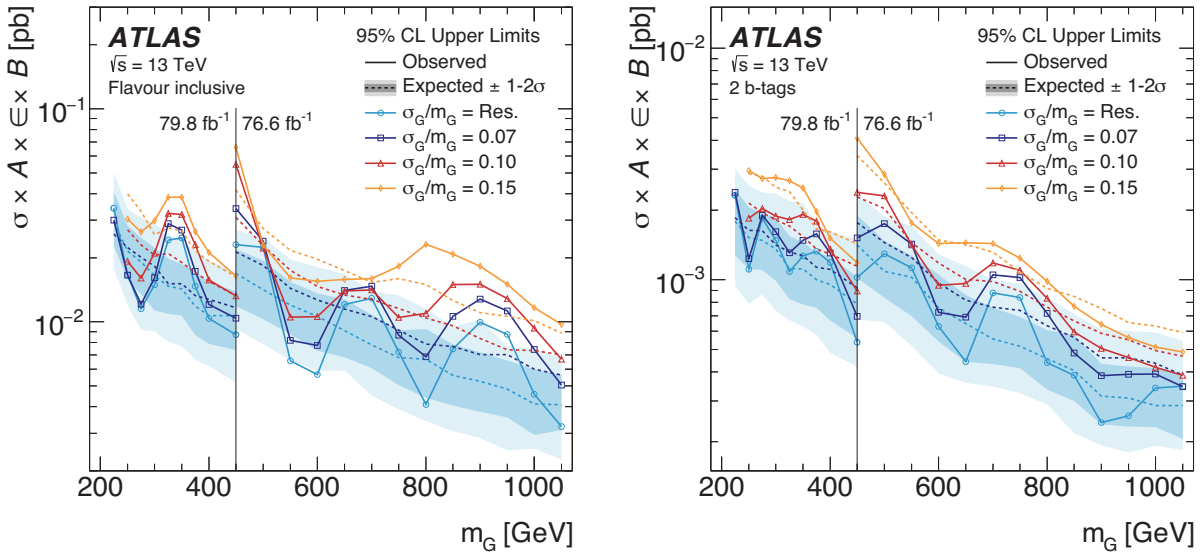

(a) (b)

Figure 7.3: Upper limits on Gaussian-shape contributions to the dijet mass distributions from a the flavour-inclusive and b the b-taggedcategories. The curve denoted "Res." represents the limit on intrinsically narrow contributions with Gaussian mass resolution ranging from 8% to 3% for the mass range considered. Below 450 GeV, the distribution of events selected by the single-photon trigger is used for hypothesis testing, while above 450 GeV the combined trigger category is used. While the vertical axis is shared between the two selections, the signal acceptance is not the same below and above the line, and this results in different limits for the 450 GeV resonance mass point. Thus the two sets of limit points correspond to two different interpretations of the product of cross-section, acceptance, efficiency, and branching ratio, $\sigma \times A \times \epsilon \times \mathcal{B}$.

value for each mass distribution. For the Gaussian-shape signal models, this average 2% shift is taken as the uncertainty of the mean of each Gaussian distribution. In the case of the b-tagged categories, uncertainties of the b-tagging efficiency are the dominant uncertainties in each mass distribution. To account for these uncertainties, the contribution of each simulated event to a given mass distribution is reweighted by 5%–15% for each jet, depending on its p_{T} [152].

The remaining uncertainties are modelled by scaling each simulated distribution by 3% to account for jet energy resolution in all categories [150], 2% for photon identification uncertainties in the single-photon-trigger categories and 1.4% in the combined-trigger categories [141], 3% to account for efficiencies of the combined trigger, and 1% for PDF-related uncertainties (only applied to the mass distributions of Z' signals).

All these uncertainties are included in the reported limits; further uncertainties of the theoretical cross-section for the Z' model are not considered.

The uncertainty of the combined 2015–2017 integrated luminosity is derived following a methodology similar to that detailed in Ref. [165] and using the LUCID-2 detector for the baseline luminosity measurements in 2017 [166]. The estimates for the individual datasets are combined and applied as a single scaling parameter with a value of 2% for the single-photon-trigger categories and 2.3% for the combined-trigger categories.

7.6 Conclusion

Dijet resonances with a width up to 15% of the mass, produced in association with a photon, were searched for in up to 79.8 (ifb) of LHC pp collisions recorded by the ATLAS experiment at $\sqrt{s}$ = 13 TeV. The observed m_{jj} distribution in the mass range 169 GeV < m_{jj} < 1100 GeV can be described by a fit with smooth functions without contributions from such resonances.

In the absence of a statistically significant excess, limits are set on two models: Z' axial-vector dark-matter mediators and Gaussian-shape signal contributions. All mediator masses within the analysis range are excluded for a coupling value of g_{q} = 0.25 and above, with the exclusion limit near a coupling of g_{q} = 0.15 for most of the mass range. The b-taggedcategories yield Z' limits comparable to the flavour-inclusive categories, assuming that the Z' decays equally into all quark flavours, and provide model-independent limits that can be reinterpreted in terms of resonances decaying preferentially into b-quarks. For narrow Gaussian-shape structures with a width-to-mass ratio of 7%, the flavour-inclusive categories exclude visible cross-sections above 12 fb for a mass of 400 GeV and above 5.1 fb for a mass of 1050 GeV. When wider signals with a width-to-mass ratio of 15% are considered, the exclusion limits are weaker at the lower mass values, with visible cross-sections above 21 fb excluded for a mass of 400 GeV and those above 9.7 fb excluded for a

mass of 1050 GeV.

These results significantly extend the constraints by ATLAS and other experiments at lower centre-of-mass energies on hadronically decaying resonances with masses as low as 225 GeV and up to 1100 GeV.

Chapter 8

The Resonance Search on the Dimuon Signature

A truth is not something that is constructed in a garden of roses."

— Alain Badiou, In Praise of Love

8.1 Introduction

Owing to its unprecedented high energy, the Run 1 and early Run 2 of ATLAS have long focused on the high mass resonances searches that were not accessible to any other previous experiments. This approach has left the relatively low mass resonances that are competitive in sensitivity unexplored. In the resonance search for particles which decays into two leptons, in particular, the resonance mass region above the Z boson peak has been searched since the beginning of Run 1 [167] [168]. However, the mass region below the Z mass peak remains uncovered to this date. Novel particles with an LHC scale observable coupling are predicted by different theoretical models, some of them are related to the dark matter models explored in Chapter 3.

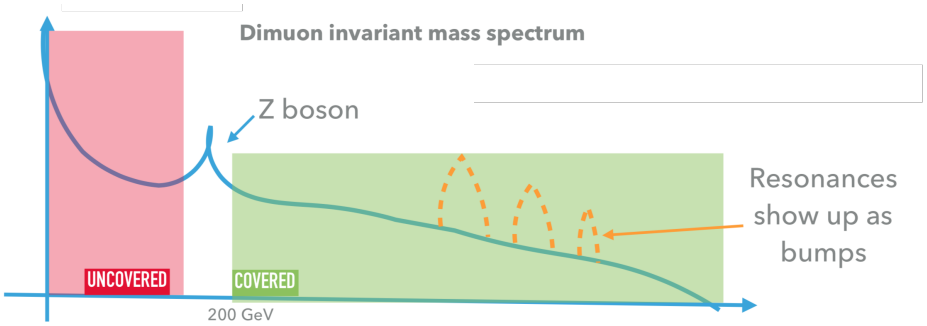

Figure 8.1: This cartoon illstrate the target signal region of the analysis and how it has not been covered by the previous high-mass dilepton analysis.

This study shares many similar motivations as the analysis presented in Chapter 7, in which the dark matter mediator Z' is projected to decay into two jets. In this analysis, dark matter mediator Z' also couples to leptons. Since ATLAS collides protons, there are fewer background events which produce lepton than those which produce jets, allowing ATLAS to retain events with leptons above a lower transverse momentum threshold. To avoid the quarkonium background between 4-10 GeV and the Z boson in 80 GeV, this analysis searches for resonances in the 10-68 GeV range.

This chapter presents an ongoing analysis of ATLAS. Most of the strategies have been finalized and the analysis is on its way to being unblinded. The data preparation, trigger chain, event, and object calibration that is completed and validated for the analysis is presented in Section 6.3. The full statistical strategies, which utilize Gaussian Process as the background estimation method, are covered in Section 8.5. The analysis utilizes data from the proton–proton collision in ATLAS recorded at a center-of-mass energy of $\sqrt{s}$ = 13 TeV up to 139 fb^{-1} of integrated luminosity. The projected result is interesting to the theoretical community for the dark matter mediator reinterpretation as well as its constraint on signatures of many other possible models, which include quantum blackholes [169] and Z* [170]. The result of this study is complementary to the higher mass dilepton search and is assumed to have limits comparable to the CMS [171] and LHCb [172] results. This work also references previous studies performed in [103].

8.2 The Search Channels

In the LHC, not all collision events are stored due to the limitation in processing bandwidth. Triggering is the processing and storage of selective events (See Chapter 4 for more details). Triggering introduces distortions in the distributions of the kinematic quantities. An example is the muon P_T requirement in triggering, which produces a trigger turn-on feature in the search region as seen in the red inclusive histogram in Figure 8.2. Non-physical features in the background can lead to

difficulty in background modeling. Given this, in the dimuon analysis, two different search channels are employed. In the 40-68 GeV region, the inclusive dimuon signal as shown in 8.3 is searched for. In the 10-40 GeV of the analysis, an initial state radiation(ISR) signal as shown in 8.4 is hunted. Figure 8.2 feature the background distributions of these two search range highlighted in blue. In the boosted channel, an additional cut of dimuon $P_T > 14GeV$ is applied to the dataset. This cut produces a smooth background and retains a signal efficiency of above 90% using the ISR signal. This strategy is effective in producing a background that can be modeled and maximizing the search sensitivity. This two-channel treatment was first proposed in Ref [103]. Changes have been made to accommodate the increase in the center-of-mass energy of the analysis.

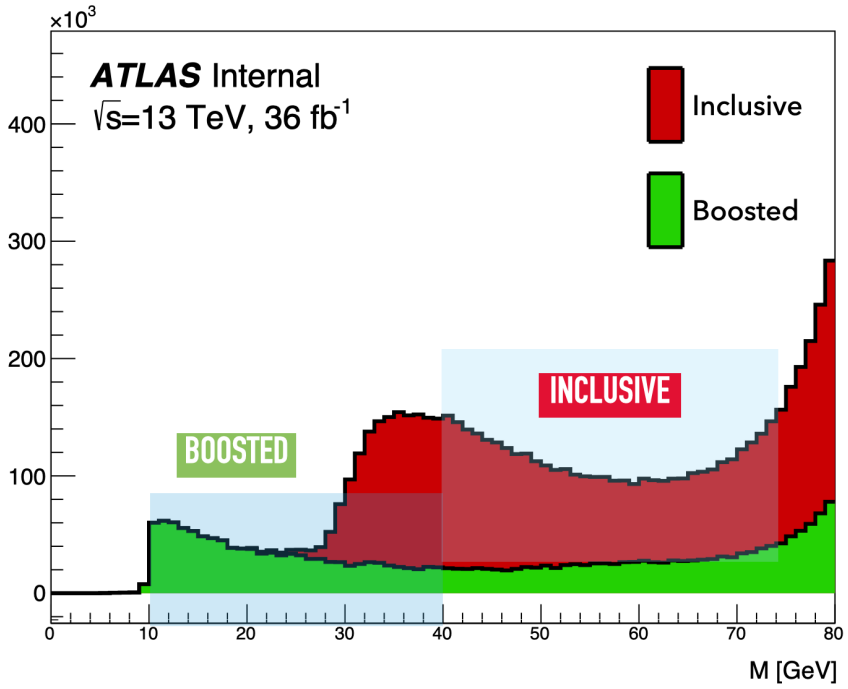

Figure 8.2: This figure shows feature from trigger turn on in the inclusive dimuon channel that results in a bump in 35 GeV(Red) . Utilizing a minimal dimuon P_T cut in the boosted channel made it possible to recover a smooth background in the lower mass region from 10-45 GeV(Green). Samples used here are MC16a ATLAS full simulation listed in section 8.2.

8.3 Signal Theoretical Model

The analysis uses the dark matter LHC benchmark model and dark photon model outlined in Section 3.5.5 of Chapter 3. Limit setting on generic Gaussian shapes of various width will enable ease for reinterpreations for other models. Figure 8.3 and Figure 8.4 show the Feynman diagrams of the signal used for the analysis. The signal MC is generated through ATLAS full simulation:

the tree level event is generated through Madgraph5_aMC@NLO [173]; the parton showering is simulated through Pythia8 [174] and detector effect is modeled with Geant4 [175]. See Chapter 5 for details.

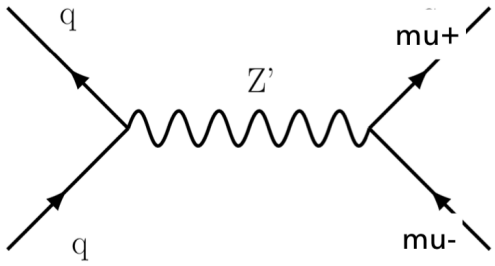

Figure 8.3: This figure shows the Feynman diagram of the inclusive dimuon signal as the signal for the analysis.

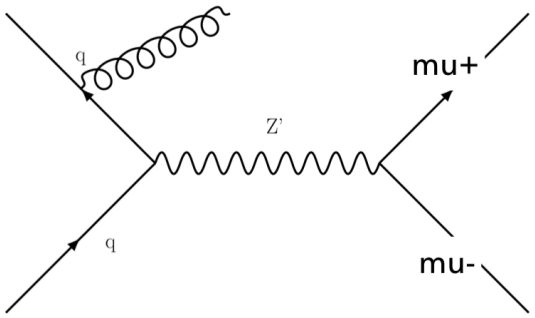

Figure 8.4: This figure shows the Feynman diagram of the dimuon ISR signal for the boosted channel of the analysis.

8.3.1 Trigger Chain

Triggering is the selective storage of events due to limiting processing and storage bandwidth. Details on the ATLAS triggering system can be found in Chapter 4. Triggering streams each have different cuts and they are tailored for different purposes. Using multiple trigger streams with careful re-weighting could maximize the signal trigger efficiency through the use of multiple streams. In the dimuon analysis, three trigger streams are employed for this reason.

Table 8.1: The table shows the trigger used for the dataset.

Type	**Period**	**Trigger Chain**	**Level 1**	$p_T^{\text{cut offline}}$ **(GeV)**
Isolation Single Muon	2015	HLT_mu26_iloose_L1mu15	MU15	27
	2016-2018	HLT_mu26_ivarmedium	MU20	
Non-Isolated Single Muon	2015-2018	*HLT_mu50*	MU20	27
Symmetric Dimuon	2015	HLT_2mu10	2MU10	15, 15
	2015-2018	HLT_2mu14	2MU10	
Assymetric Dimuon	2015	HLT_mu18_mu8noL1	MU15	24, 10
	2016-2018	HLT_mu22_mu8noL1	MU20	

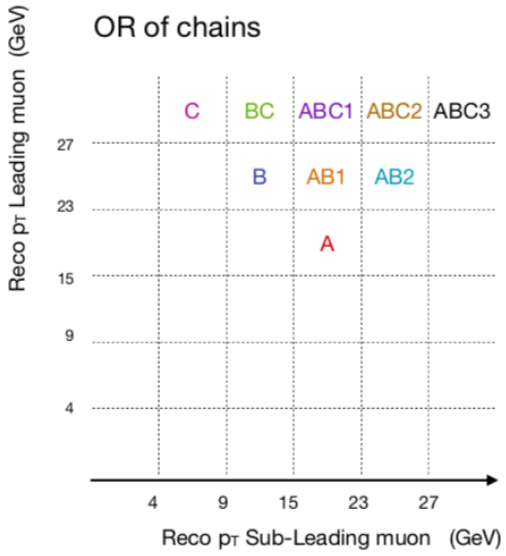

Figure 8.5: This cartoon illustrates the trigger used for the different trigger region: A indicates HLT_2mu14; B represents HLT_mu22_mu8noL1; C shows HLT_mu26_ivarmedium.

8.4 Data preparation

The final result of the strategies presented in this chapter is collected from proton-proton collision data during the ATLAS Run 2 period at a center-of-mass energy of $\sqrt{13}$ TeV from 2016-2018. The preliminary strategy of this chapter is generated from ATLAS full simulation Monte Carlo, besides the $Z > \mu\mu$ sample used. Due to the processś low statistics in the ATLAS full simulation, a full-size $Z > \mu\mu$ sample is created through a fast Sherpa and PYTHIA8 combination generation. Section 8.4.1 details the superfast event generation. The MC are used for signal sensitivity test, the binning studies as well as the finalizing the background Gaussian Process hyper-parameters in this analysis before applying them to data.

8.4.1 Samples Used for the Analysis

The following are the samples used for the analysis. The largest background contribution in this analysis is the $Z > \mu\mu$ process; the second-largest contribution originates from $Z > \tau\tau$. Other processes, including the t-channel $t\bar{t}$ decay, diboson decay as well as top decay contribute a considerable amount to the background events.

Fast Simulation $Z > \mu\mu$ Samples

Due to the low statistics in the primary background sample in $Z > \mu\mu$, fast generation relying on Pythia8 and a smearing function for the detector effect has been used to emulate imperfect resolution of the detector. Four of the superfast statistics as been used, each using a different pdf set for the generator tuning. The nominal set uses the ATLAS A14 NNPDF2.3LO; the down variation and up variation uses the variation tune parameters Var3C described in Ref [162]; whereas the η variation uses ATLAS A15 NNPDF2.3 along with QCD and QED NLO. More details on the fast simulation are given in Ref [176].

Table 8.2: The table shows the Monte Carlo background dataset used for the analysis.

MC Type	**DSID**	**Generator Used**
Z > $\mu\mu$	364100 - 364113 , 364198-364203	Fast Simulation through PYTHIA
Z > $\tau\tau$	364128 - 364141 , 364210-364215	Sherpa
$t\bar{t}$	410472	Sherpa
Diboson	364253 - 364255 , 363355 - 363360 ; 363489 ; 364250 ; 364288 - 364290	Sherpa
Top decay	410644 - 410645 , 410658 - 410659 ; 410648 - 410649	Powheg+Pythia8
$W+$ jets$\mu\nu$	364156 - 364169	Sherpa
$b\bar{b}$	363833	Pythia8b
$c\bar{c}$	363834	Pythia8b

In the analysis, studies on signal sensitivity found that muons of the **MEDIUM** working point and the **FixedCutPFlowLoose** isolation working point (Defined in Chapter 5) will provide the maximal muon performance and signal sensitivity. Two muons of at least 4 GeV in transverse momentum and $|\eta| < 2.5$ are required for each event. An additional $P_T > 14$ GeV cut is applied to events in the boosted channel.

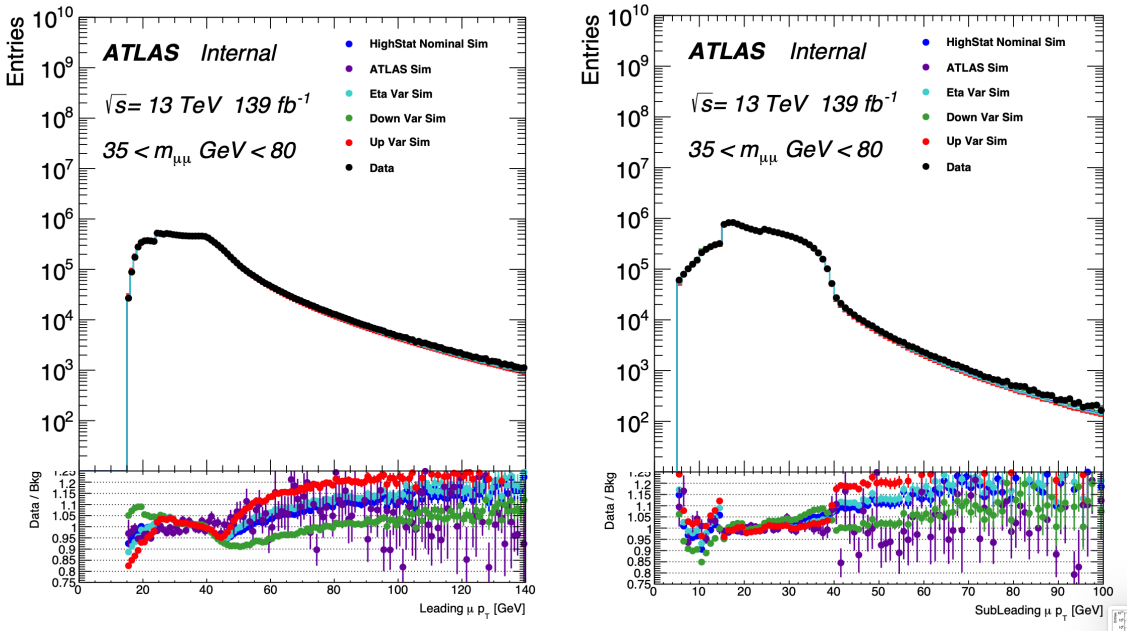

Figure 8.6: These plots shows the leading muon transverse momentum distribution and the subleading muon transverse momentum distribution with the super fast simulation. The MC samples here include Z > $\mu\mu$, Z > $\tau\tau$, $t\bar{t}$, Diboson, top quark decay and $b\bar{b}$ and $c\bar{c}$. the bottom pane shows the data to MC ratio.

8.4.2 Dimuon Mass Spectrum Resolution

To define the binning of the dimuon mass distribution in the signal region, the dimuon mass resolution is studied. The following study is performed on the Z > $\mu\mu$. Details on the procedure can be found in Chapter 6 in Section 6.3.1.

Fit of a Gaussian pdf to the distributio of the difference between the true and reconstructed dimuon resonance mass ($m_{\mu\mu_{Truth}} - m_{\mu\mu Reco}$) is performed. From the fit, the width of the Gaussian is obtained, as shown in Figure 8.7. It is taken to be the detector resolution in the dimuon mass distribution. The bin-by-bin resolution result is shown in Figure 8.8.

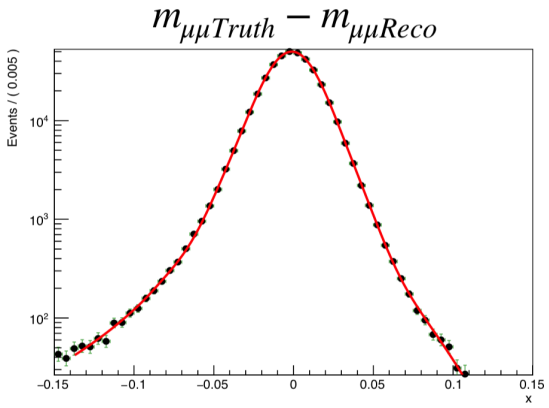

Figure 8.7: Fit of a Gaussian pdf to the distribution of the difference between the true and reconstructed dimuon resonance mass.

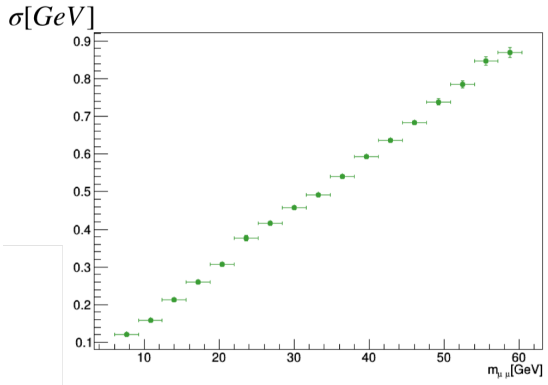

Figure 8.8: The fit shown in Figure 8.7 is repeated in bins of the reconstructed dimuon resonance mass. Shown is the fitted width in each bin, with statistical uncertainties. The width-to-mass resolution $\sigma_{m_{\mu\mu}}/m_{\mu\mu}$ is found to be close to 1.5%.

8.4.3 Binning Strategy

Using the resolution of the study from the last section and the mass distribution given in the theoretical signal section, the overall binning is chosen to be 0.25 GeV, close to the resolution at the center of the spectrum. The choice is made mostly due to uniform binning simplified the fitting procedure considerably. The choice also ensures most of the signals searched for are at least 2 bins wide to reduce the probability of capturing a signal from statistical fluctuation only seen in one bin.

8.5 Background Fitting with Gaussian Process

As the fully simulated ATLAS MC for the background processes listed in table 8.2 is neither reliable in shape nor enough in the count. This is due to imperfect shower and hadronization process modelling in the simulation, and a cap on the computing resource that can be spent on MC full simulation on ATLAS. The effect can be seen in the data/mc comparison in Figure 8.6. The background fitting of the dimuon analysis therefore relies on a data-driven approach. The kernel hyper-parameter is studied on MC variations that aims to include all variation that may be presented in data. Details on data-driven approaches for smooth background estimation is presented in Section 6.4 of Chapter 6. The approach used by the dimuon analysis is the Gaussian Process approach outlined in Section 6.4.3 of Chapter 6. Only details specific to the analysis and results are described here.

8.5.1 The Kernel

In Gaussian Process, the mean function prediction and the covariance function on the prediction variance are determined by the kernel function. The Gaussian Process background and signal kernels used for this particular analysis method are given in Eq. 8.1 and Eq. 8.2.

- **Background Kernel** - *"Radial Basis Function + White Noise Kernel"*

$$K_{bkg}(x, x') = A_1 * exp(-\frac{||x - x'||}{2\sigma_1^2}) \tag{8.1}$$

  Here, A_1 is the amplitude hyperparameter that describes the size of the kernel, σ_1 is the lengthscale parameter.

- **Signal Kernel** - *"Exponential Center Kernel + White Noise Kernel "*

$$K(x_i, x_j) = A_2 \cdot exp(-(x - m)^2/(2 \cdot \sigma_2^2)) \cdot exp(-((x' - m)^2/(2 \cdot \sigma_2^2))) \tag{8.2}$$

Here, A_2 is the amplitude of the signal kernel, m is the mass location of the signal peak, and σ_2 is the lengthscale of the signal kernel.

Test for the Background Kernel

Although there are noticeable difference between the data and MC, it is believed that the MC along with its different tune variation could still give a good general understandning of what the data

shape may look like at unblinding. Verification tests are performed to ensure the background MC can be described by the background kernel. The procedure is described as the following:

To ensure the fit is not biased by the statistical fluctuation, the fit on the spectrum is compared to the fits in the toy distributions. Toy distributions are created from drawing the Poissonian distribution in each bin. 10,000 new toy distributions are formed. Each is fitted with the Gaussian Process background kernel and test statistics defined in Section6.5.1 are calculated for each fit. The p-value is calculated from that, by comparing the fit test statistics against the distribution of the test statistic in pseudo-experiments which describe typical statistical fluctuation from the background as described by simulated samples. (See Eq. 6.17). Results in Figure 8.9 that all three test statistics tested the p-value is above 0.01 and that the kernel captures features in background distribution well.

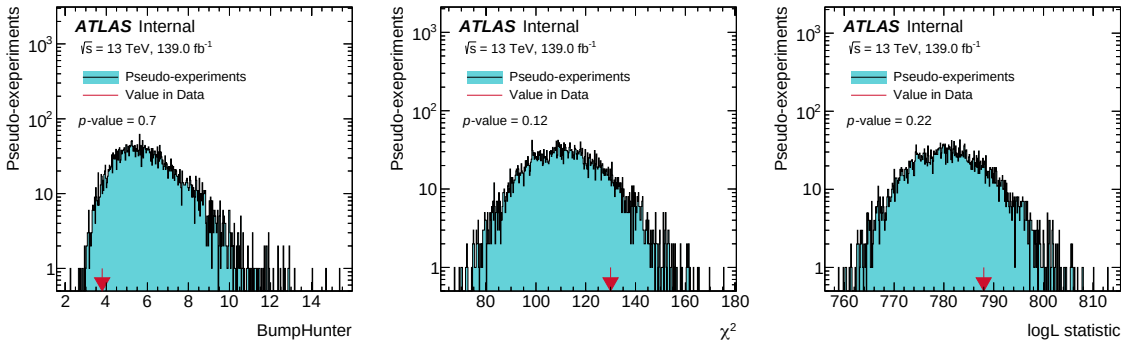

Figure 8.9: These plots illustrate the test statistics of the fit on MC compared against the fit on the pseudoexperiment from MC.

8.5.2 Hyperparameter Optimization

The detailed steps to the hyper-parameter optimization can be found in Section 6.4.3 of Chapter 6. The lower bound on the lengthscale of the background kernel and the signal kernel are finalized from the signal injection test result in Section 8.5.4 and Section 8.4.3 respectively. The other hyper-parameters are allowed to float. They are optimized with the scaled conjugate gradient algorithm.

In the dimuon analysis, the background kernel fits are performed on several distinct variation of the fast simulation MC(See Section 8.4.1 to ensure the selected hyper-parameters and lengthscale are flexible enough for the variation possibly present in the final data. Figure 8.10 shows fitting results in the inclusive region of the MC using the background kernel listed in 8.4.1. The results show that the lengthscale lower-bound chosen from the signal injection test is flexible enough to provide accurate prediction to MC variations.

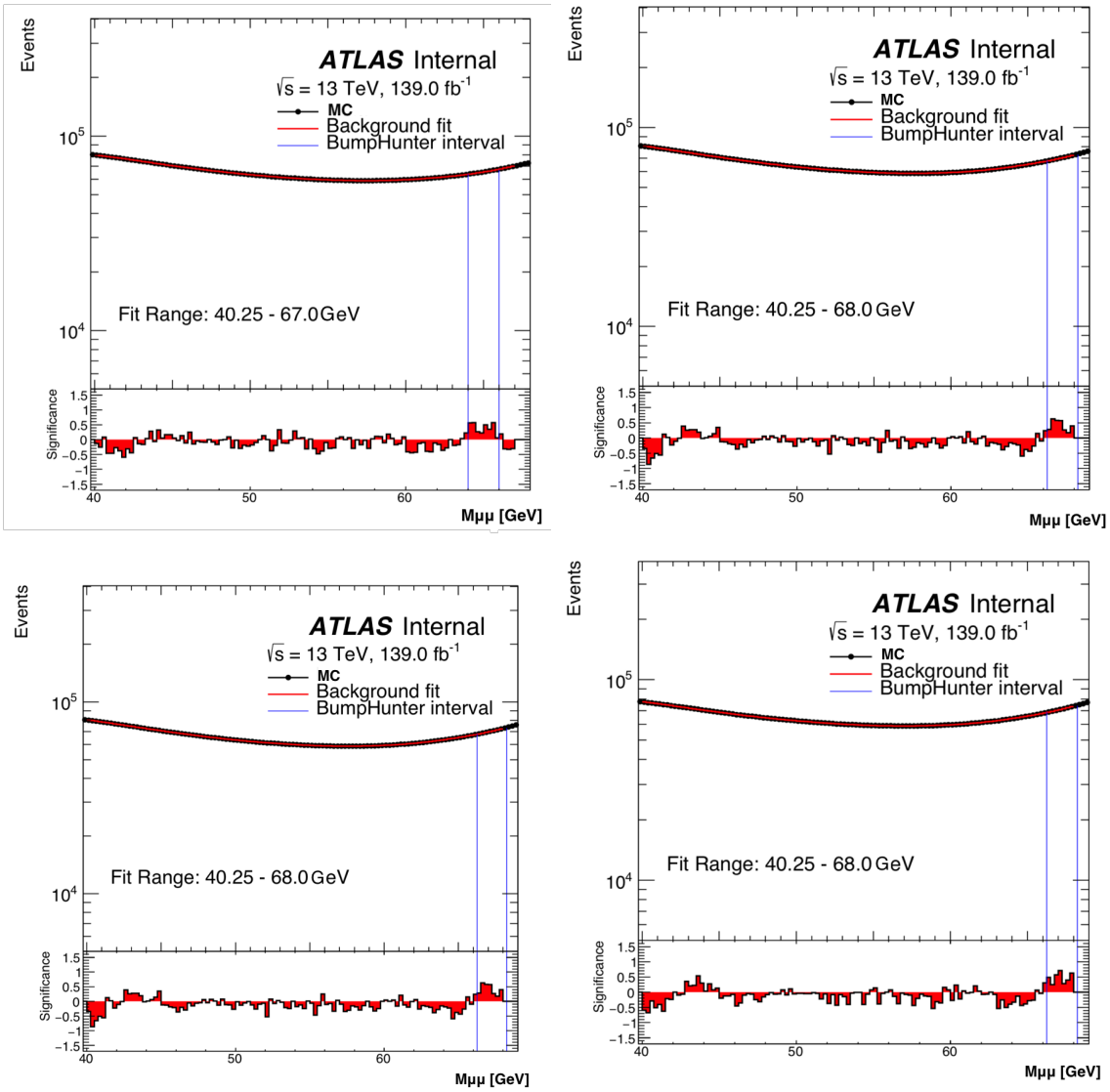

Figure 8.10: These figures illustrates the Gaussian Process background kernel fit on the different variation of fast simulation detailed in Section 8.4.1. The fit test statistics as well as the residual in the bottom panel shows that the background kernel is able to capture features in the background variation.

8.5.3 Background and Signal Estimation

Background estimation from the background kernel alone was not able to separate the background from the signal to high efficiency. The final background and signal estimation are performed through the following separation equations. The computed results is used for the limit setting where signal strength is estimated. Figure 8.11 shows an example separation performed by the method.

- **Background Prediction**

$$\mu_{bkg}(x_*|y) = \mu_{\text{bkg kernel}}(x_*|y) + K_{\text{bkg kernel}}(x_*, x) \cdot K_{\text{sig+bkg kernel}}(x, x') \cdot (y(x) - \mu_{\text{bkg kernel}}(x_*|y)) \tag{8.3}$$

- **Signal Prediction**

$$\mu_{sig}(x_*|y) = K_{\text{sig kernel}}(x_*, x) \cdot K_{\text{sig+bkg kernel}}(x, x') \cdot (y(x) - \mu_{\text{bkg kernel}}(x_*|y)) \tag{8.4}$$

Here, $\mu(x_*|y)$ is the mean function posterior prediction of of point x_*, given known data point x and y, K is the kernel. $\mu(x_*)$ is the prior probability distribution mean. x is a vector of the input mass point, and x' are the same points in a 2d matrix.

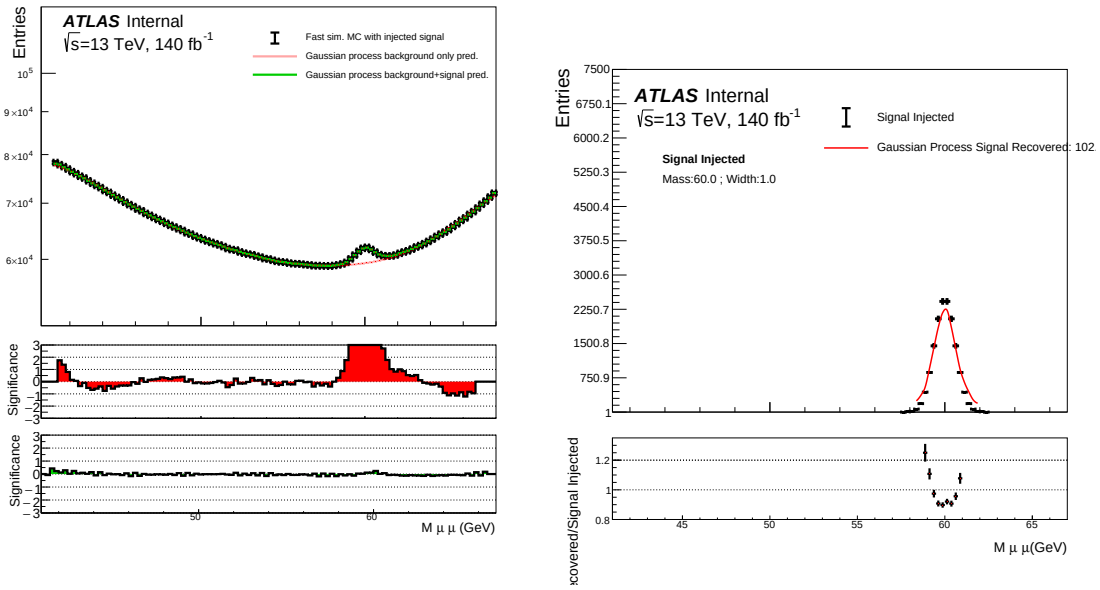

Figure 8.11: These figures shows the background estimation and the signal estimation separated a sample MC generated from a Gaussian signal injected into the background. The signal reconstruction yield for this particular signal is up to 94%.

8.5.4 Background Prediction Performance Studies

The Gaussian Process background prediction went through testing suggested in the ATLAS smoothing recommendation document [97]. to ensure the smooth background procedure is valid for resonance searches. Two tests, the signal injection test and the spurious signal test are conducted to ensure the background estimation is sensitive to signals above a certain size in comparison to the backgroud error. The results are presented in the following subsection.

Signal injection test

The aim of the signal injection test is to quantify the signal sensitivity of the background estimation method. If the background estimation method can discriminate signal of at least 3 times the size of the background estimation statistical uncertainty along the search region mass point, it passes the test. The test is also used to select a lower bound on the lengthscale of the Gaussian Process background kernel in Eq. 8.1. Only a lower bound lengthscale with the above mentioned sensitivity is used for the analysis.

Details of the procedure of the signal injection test can be found in Ref [97]. Only results are presented here. Results found that a minimum lengthscale of 4 GeV is needed for the background kernel for the background model to be sensitive to signal of 3 σ background estimation statistical uncertainty in the 45-68 GeV range in the inclusive region.

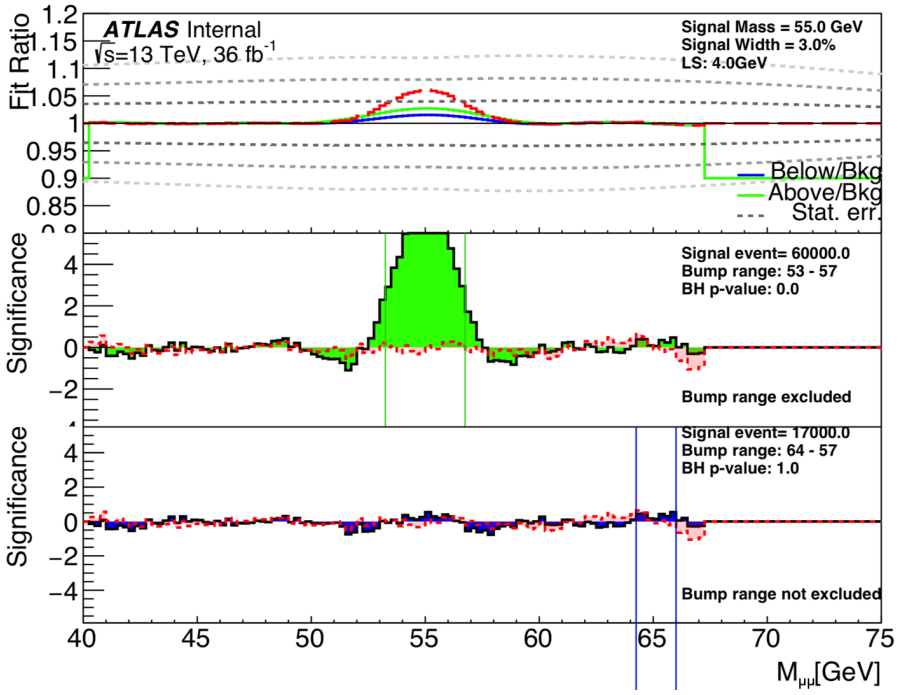

Figure 8.12: This figure illustrate a signal injection test performed on background MC a resonance mass point 55GeV of 3% mass width. In the first panel. the red line shows the background MC + signal injected divided by the background MC; the green and the blue line are the fit ratio of the "just above" bumphunter window exclusion(when a window has a bumphunter p-value below 0.01), and the ratio of the "just below" trigger of the bumphunter fit versus the background MC. The grey bands shows the width of the background estimation statistical uncertainty. Results shows that the the fit is sensitive to signal < 3 σ of the background error in this mass point and width, passing the signal injection test.

Background Modelling

Using the minimal lengthscale chosen from the signal injection test from the above section and allowing other hyperparameters to float, tests fits are performed on the nominal background MC set, and also performed on the different statistical variation of the background, the 1 σ up and 1 σ down variation of the fast simulation Pythia, as well as the η variation, defined in Section 8.4.1. The fitting result shows that lengthscale chosen for Gaussian Process works well for all of these statistical variations.

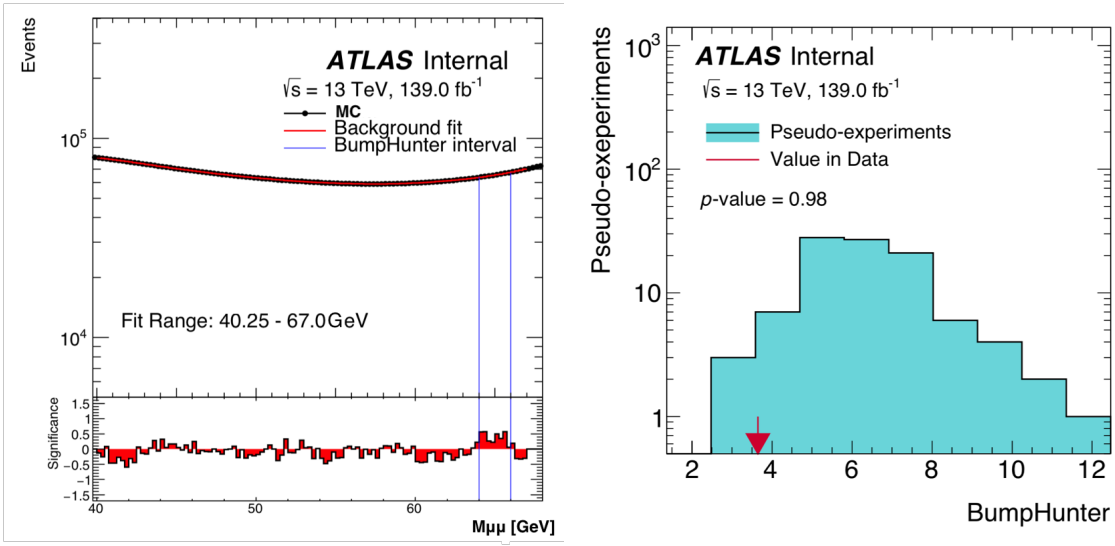

Figure 8.13: These figure illustrates the fit on MC, along with the bumphunter test statistics and the observed value distribution. It is shown that the most discrepant window does not fall below the critical p-value of 0.01. Details on the bumphunting procedure can be found here.

8.5.5 Spurious signal test

The spurious signal test is a test that defines the background estimation uncertainty relative to signal yield. Details are presented in Ref [97]. The test is considered passed if the signal extracted versus the background estimation uncertainty ratio is < 0.5. The spurious signal test results on the Gaussian Process are shown in Figure 8.14. Currently, work is ongoing to further reduce the spurious signal.

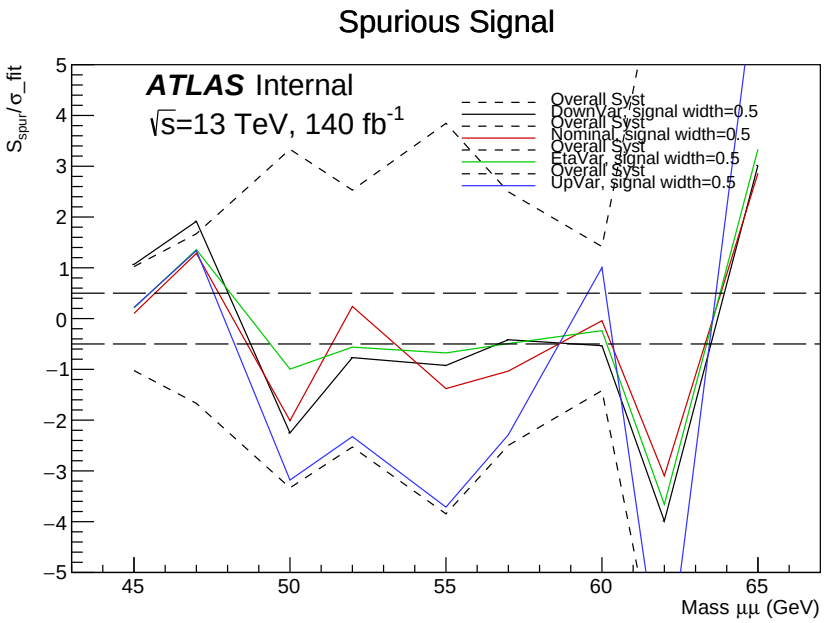

Figure 8.14: This figure illustrates the results of the spurious signal test on several variations of the background model produced with simulated samples

8.6 Statistics Testing

Details on the statistical test can be found here in Section 6.5. As of the writing of this thesis, the data have not yet been unblinded. MC studies were implemented to verify the procedure.

8.7 The Search

The search aims to either accept or reject the null hypothesis of only SM background exist in the data. Details are listed in this Section 6.5.1. Here, examples demonstrating the what the result may look like when data is the background MC; and when the data is the background MC and additional signal is shown. This is a demonstration of the working pipeline of the statistical test.

An example of the search is implemented with just the background and no signal injected is shown in Figure 8.15 and another result with an artificially injected signal is shown in 8.16. The tests are performed as a demonstration of what the result of the unblinded data may look like if it is similar to the background MC, or if an excess is present.

In the background only MC example, the loglikelihood, the χ^2 ,and the bumphunter test statistics all have p-value above 0.01. No anomaly is found and the null hypothesis is accepted. In the

background and signal example, the bumphunter test statistics all have p-value below 0.01. The result indicate an excess could be present.

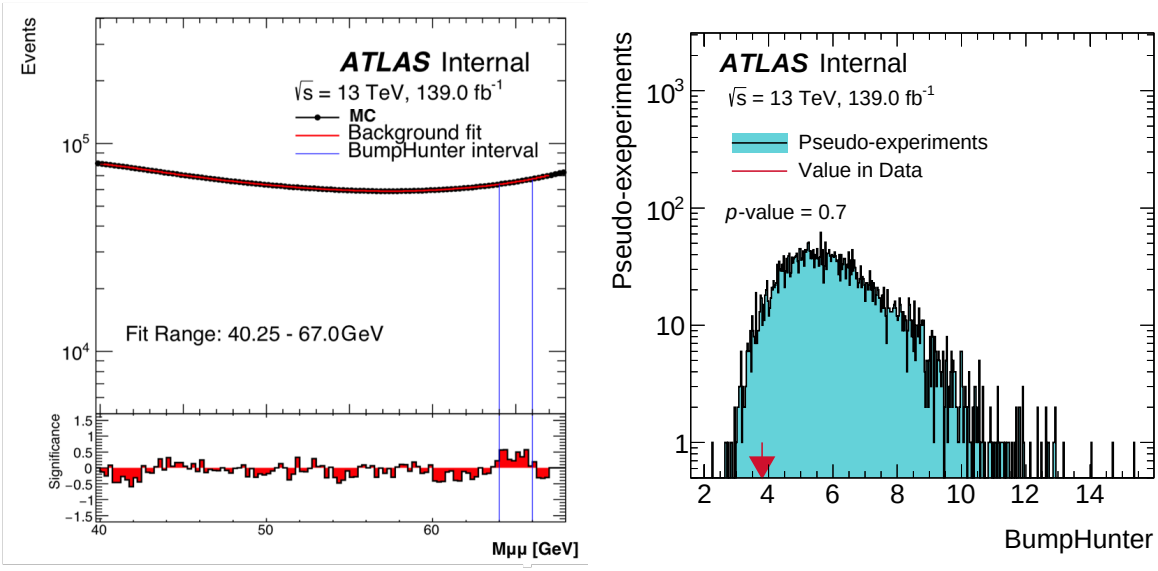

Figure 8.15: These figures illustrate a statistical test on background only MC, the p-value is observed to be way above the 0.01 cut off for anomaly. In this case the null hypothesis is accepted.

Another example of the search is implemented with the background with a toy signal of a Gaussian shape that peaks at 50 GeV. The bumphunter test statistics have p-value below 0.01. The fit result is presented in Figure 8.16. The null hypothesis is rejected.

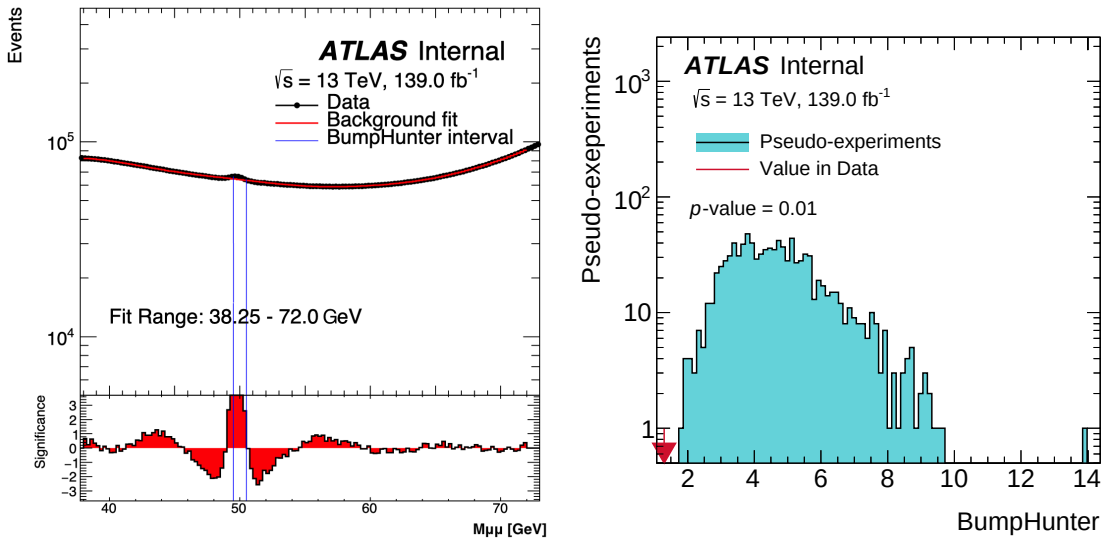

Figure 8.16: These figures illustrate a test performed on signal injected at 50 GeV, and the window exclusion that picked out the signal injected in there.

These demonstrations indicate that the statistical pipeline is functioning and ready to be applied to collision data.

8.8 Limit Setting

In the dimuon analysis, the limit setting procedure is done through the Asimov approximation of the frequentist limits described in Section 6.6. Preliminary limit setting based on Gaussian Process is still currently under test. A limits calculated by approximation based on the fit function method on background only MC are shown here in Figure 8.17.

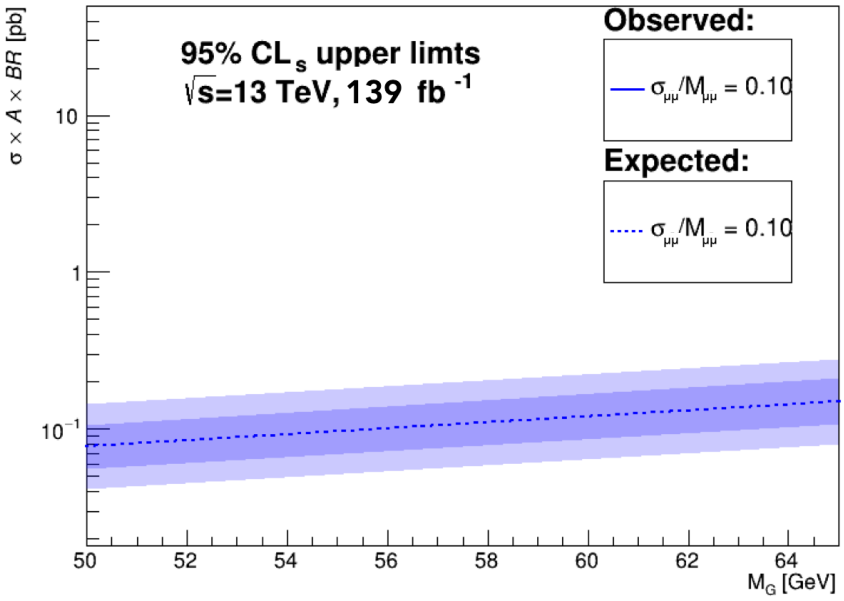

Figure 8.17: This figure illustrate limits from the background MC.

8.9 Conclusion and Future Work

As per 2022-2-27, a presentation of the above result was discussed at the ATLAS statistics forum and it was recommended that the analysis be reperformed with all the hyper-parameters fixed from the fitting of different variations of fast simulations. Another outstanding items include the implementation of the Gaussian Process test statistics into the frequentist limit setting statistical framework. This will allow for direct calculation of the likelihood for the Asimov calculation. These items are underway.

Chapter 9

Future Resonances: The Unexplored Landscape of Two-body Resonances

The possible ranks higher than the actual.

–Martin Heidegger

This chapter is heavily based on work previously published on [177] in collaboration with Nathaniel Craig, Patrick Draper, Kyoungchul Kong and Daniel Whiteson.

9.1 Introduction

Searches for two-body decays of heavy resonances have a rich history of important discoveries, from the J/ψ to the Higgs boson. Such resonances can provide an unambiguous signature of a localized invariant mass peak and offer simple background estimation from sidebands, allowing for discovery without requiring full models of the signal or background processes. These experimental features, combined with compelling theoretical arguments, motivate much of the current program of resonance searches.

The theoretical arguments for new resonances mostly consist of simple generic extensions to the Standard Model (e.g. a new $U(1)$) or modifications to the SM which address an outstanding theoretical problem (e.g. Kaluza-Klein gravitons). To date, most of the experimental searches have followed these theoretical arguments, leading to many searches for pairs of identical objects (eg $ee, \mu\mu, jj$) and in rarer cases for non-identical pairs (eg $e\mu, ZW$). However, the dramatic scale of the open theoretical questions facing particle physics suggests that a correct theory of

Nature may not be one of the models currently in fashion or under specific consideration. This motivates an experimental program which is not narrowly focused on current models and the signatures they suggest, but with a broad scope and systematic approach capable of theoretically unanticipated discoveries. While there have been many proposals for model-independent search programs at hadron colliders (such as the framework of on-shell effective theories [178]), they have been largely motivated by specific theoretical frameworks, and consequently many holes remain in the existing experimental program at the LHC. To make concrete progress, we propose a systematic search for new particles decaying into n-body resonances. In the $n = 2$ case, this would consist of searches for resonances in all pairs of objects, even those which have no theoretical motivation or are theoretically disfavored.

The typical difficulty facing searches without specific theoretical motivation is the large number of possible observables, which incurs a very large trials factor and greatly reduces the discovery sensitivity. Here, rather than relying on theoretical guidance, we propose to restrict the vast space of possible theories into those that align well with experimental strengths. We are interested in covering the intermediate ground between the very specific and the very general search programs, by focusing on well-defined topologies independent of specific theory considerations. This broadens the search program beyond favored theories, but not so much so as to compromise discovery potential. Given that the data exist and resonances are fairly easy to discover, we argue that the two-particle spectra are worth directly examining. In many cases, there are indirect constraints on such resonances from other experiments or subjective theoretical arguments, but there is no real substitute for a direct search.

In this chapter, we lay out the details of the implementation of such a search program and survey the existing experimental and theoretical landscape for exclusive $n = 2$-body resonances, leaving $n = 3+$ (as well as inclusive $n = 2$ final states) for future work. We find that the majority of 2-body resonances have some indirect theoretical constraints but have received almost no experimental attention, leaving most of the landscape unexplored and a large potential for unanticipated discovery.

9.2 Scope & experimental searches

We consider resonances decaying to a basic set of identifiable light objects (charged leptons, photons, light-quark jets, b-tagged jets) as well as heavy objects (top quarks, weak bosons, Higgs bosons) which are routinely identified[1]. In the case of $n = 2$ objects, this gives 55 unique pairs of exclusive

[1] One could imagine restricting the scope to light objects, categorizing the heavy objects as higher-level decays (eg $X \to WW \to 4j$ would be considered in the $n = 4$ category rather than $X \to WW$ as $n = 2$). This is equivalent, but allows us to call attention to these typical objects rather than considering them as special mass cases of higher-level decays.

final states, see Table 9.1. Final states with higher number of objects have a larger number of exclusive final states; we reserve these for future work.

We examined experimental searches from ATLAS and CMS in data collected from proton-proton collisions with $\sqrt{s}$ = 8 TeV. We consider exclusive final states only in terms of the pairs of identifiable objects defined above. For example, in the $e\gamma$ category of this exclusive n = 2 survey, we consider only searches for $e\gamma$, of which there are none, and do not consider searches for $e^+e^-\gamma$, of which there are several motivated by excited lepton models that give a resonance in $e\gamma$. The final state of $e^+e^-\gamma$ would be covered by an n = 3 study, and extrapolation of those limits to the n = 2 $e\gamma$ category requires theoretical assumptions about the production modes.

The survey of n = 2 final states is shown in Table 9.1, with the striking feature that most diagonal entries have existing searches, where as most off-diagonal entries do not. In the case of the Higgs boson in particular, there are several unexamined resonance categories. Note that the lack of searches in these resonance categories is not for want of theory models. Examples of theories that populate the entire landscape of 2-body resonances are shown in Table 9.2.

Even in cases where searches exist, there are often unexamined regions in the resonance mass. Figures 9.1 and 9.2 show the strongest limits on the cross section times branching ratio as a function of the resonance mass for all results which satisfy the requirements.

9.3 Theoretical constraints

Various theoretical constraints may be imposed on n-body resonances, which in turn influence the likely production and decay modes at the LHC. In order to maintain the broadest possible scope, we consider only the most stringent constraints imposed by gauge invariance and Lorentz invariance, as experimental constraints on e.g. flavor violation depend on the details of the underlying model and may in principle be evaded.

Gauge invariance and Lorentz invariance restrict the possible statistics and quantum numbers of a resonance decaying to a specified 2-body final state. The statistics and possible $SU(3)_c$ and $U(1)_{em}$ numbers of 2-body resonances are enumerated according to their exclusive final state in Table 9.3. Note that we enumerate only $SU(3)_c \times U(1)_{em}$ quantum numbers rather than $SU(3)_c \times SU(2)_L \times U(1)_Y$ quantum numbers, because a large number of $SU(3)_c \times SU(2)_L \times U(1)_Y$ representations may share the same exclusive final state provided additional insertions of the Higgs vacuum expectation value. We also do not exhaustively list all possible $SU(3)_c$ representations, but for simplicity restrict our attention to states transforming in the fundamental or adjoint representation; resonances transforming in other representations of $SU(3)_c$ may have different pair production cross sections but do not lead to significantly different signatures. While a fermionic

resonance with Standard Model quantum numbers generally contributes to gauge anomalies, these anomalies may be cancelled by additional particles that do not influence the collider signatures of the resonance.

Gauge invariance and Lorentz invariance also dictate the structure of operators coupling a resonance to Standard Model particles, and in many cases the couplings must arise via irrelevant operators. For example, a resonance X decaying to tg cannot couple via a minimal gauge coupling $\bar{X}\gamma^{\mu}G_{\mu}t$, but may couple via e.g. a chromoelectric dipole operator of the form $\bar{X}\gamma^{\mu\nu}G_{\mu\nu}t$. In many cases, more than one Lorentz structure is allowed for a given coupling. The various possible Lorentz structures for each coupling have a modest impact on kinematic distributions for the production and decay of each resonance (see e.g. [178]), but they do not alter the key feature of interest in this work, namely a bump in the n-body invariant mass spectrum.

Note that these conclusions may be altered in the presence of significant interference effects, which may lead to deficits or peak-dip structures in the invariant mass spectrum if the Standard Model continuum interferes with the signal process. The existence and structure of interference effects cannot be determined by quantum numbers alone, and depends additionally on both the Lorentz structure and phases of couplings between the resonance and Standard Model states. However, in the limit of weak coupling, interference between a narrow resonance and Standard Model continuum backgrounds is negligible and may be neglected. To good approximation, as an expansion at weak coupling, searches for n-body resonances may therefore be parameterized solely in terms of the resonance mass, width, and production cross section times branching ratio.

Having specified the possible gauge quantum numbers of the 2-body resonance given the final state, gauge invariance and Lorentz invariance provide a guide to the possible production modes at the LHC. For each resonance there are three possibilities:

1. The particle can be *resonantly produced* either exclusively using its tree-level decay coupling (as in, e.g., a resonance decaying to qq or gg); via loop-induced processes involving the decay coupling (as in, e.g., gluon fusion production of a $t\bar{t}$ resonance); or via additional couplings to quarks and gluons allowed by its quantum numbers. The presence of such additional couplings may lead to additional theoretical constraints discussed below. Such resonant production channels fall under the scope of the exclusive 2-body searches proposed here.

2. The particle can be produced via *associated production* exclusively using its decay couplings. For example, a resonance X coupling to tW^{+} can be produced in the process $qg \to tqX$ using only the XtW^{+} coupling and Standard Model gauge couplings. This assumes no additional couplings to quarks and/or gluons. Such associated production channels fall under the scope of $n \geq 3$ studies, with a feature in the appropriate 2-body invariant mass spectrum.

3. The particle can be *pair produced* using its gauge quantum numbers (e.g. Drell-Yan via elec-

troweak quantum numbers). This process is kinematically suppressed for heavier resonances, but may be appreciable if the gauge couplings are significantly larger than the decay couplings. Such pair production channels fall under the scope of $n = 4$ studies, with features in the appropriately-paired 2-body invariant mass spectra.

The possible production modes for each resonance are enumerated. In principle, a given resonance may be produced in all three modes, with varying rates depending on the relative sizes of phase space factors and production and decay couplings. In each case the final state contains a peak in the appropriate 2-body invariant mass, but with varying amounts of additional event activity. In this sense, the associated- and pair-production modes may not qualify for the $n = 2$ exclusive case considered above, but serve as a useful foundation for future $n > 2$ studies.

There are several possible 2-body resonances for which resonant production is incompatible with Standard Model gauge invariance, in the sense that the quantum numbers of the final state cannot be produced by any initial state with appreciable parton density in proton-proton collisions. Nonetheless, searches for these 2-body resonances at the LHC remain motivated by the possibility of new physics that mimics a Standard Model final state in the LHC detectors (in the sense that, e.g., a long-lived neutral particle decaying to electron-positron pairs might be reconstructed as a photon). These states may also be produced in associated production with associated particles sufficiently soft to still appear as an exclusive 2-body resonance, or may originate from $n \geq 2$ exclusive final states with missing energy appearing in $n = 2$ exclusive searches. Such states may also be resonantly produced at other colliders consistent with gauge invariance, such as in electron-proton collisions at HERA.

Apart from gauge invariance and Lorentz invariance, less robust constraints may also apply. Many such constraints arise only when the resonance possesses both its decay coupling and additional couplings to quarks and/or gluons. Proton decay provides the strongest such constraint, as strong bounds on the proton lifetime imply that the couplings of resonances inducing proton decay are vanishingly small. In the case of 2-body resonances, resonances coupling to a single pair of Standard Model particles will not induce proton decay, but proton decay may be induced by additional couplings to quarks required for resonant production at the LHC. Resonances for which this occurs are indicated in Table 9.3; in these cases it is reasonable to expect $n = 2$ resonant production rates to be small.

Beyond proton decay, there are a variety of constraints on flavor violation, lepton number violation, and other types of baryon number violation, but in practice even strong constraints may be avoided by appropriate symmetries, textures, or fortuitous cancellations (as in e.g. maximal flavor violation [179] or diquark-type interactions [180]). In these cases there is no substitute for a direct search.

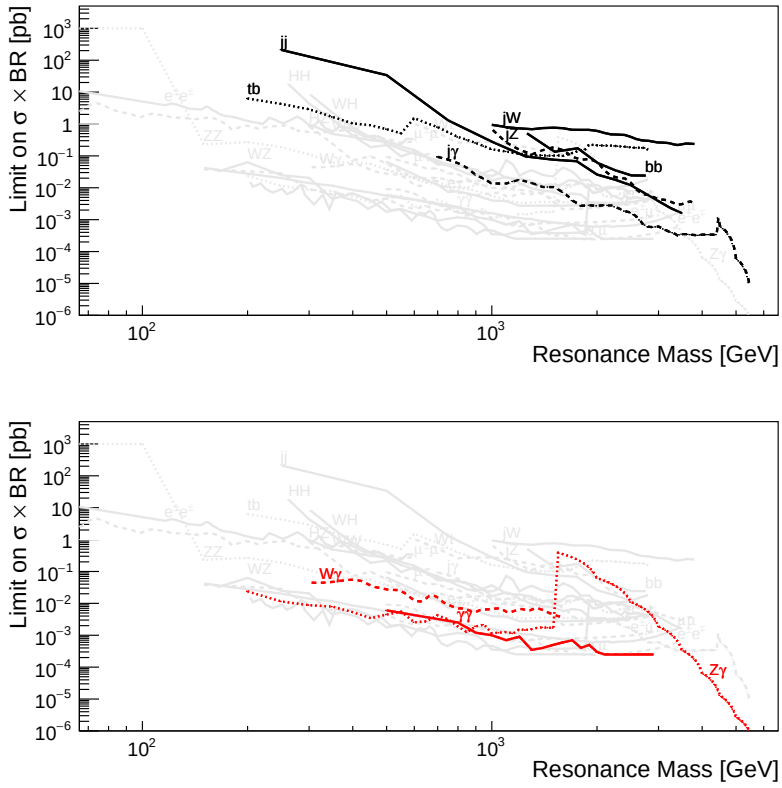

Figure 9.1: Existing limits on the cross section times branching ratio for resonances to various 2-body final states, as a function of the resonance mass. Top pane emphasizes hadronic final states, bottom pane emphasizes photonic final states. References for searches can be found in Table 9.1.

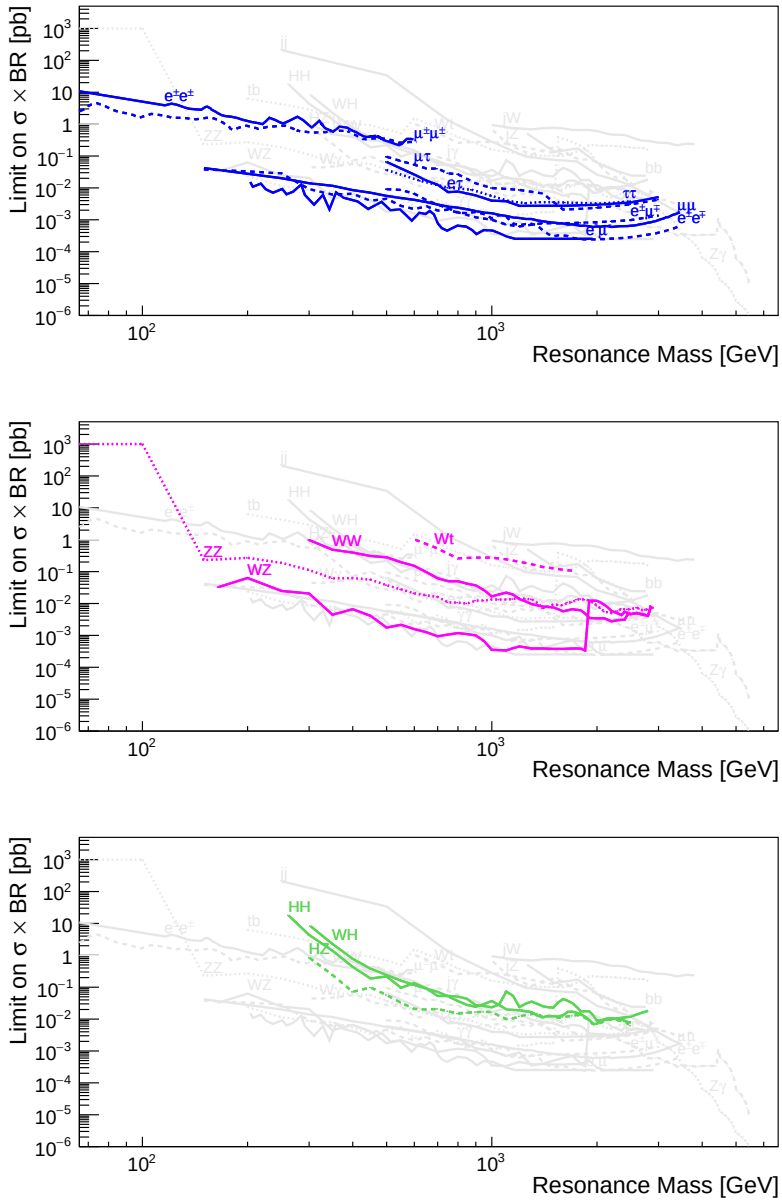

Figure 9.2: Existing limits on the cross section times branching ratio for resonances to various 2-body final states, as a function of the resonance mass. Top pane emphasizes leptonic final states, center pane emphasizes bosonic final states, and the bottom pane emphasizes Higgs final states. References for searches can be found in Table 9.1.

Table 9.1: Existing two-body exclusive final state resonance searches at $\sqrt{s}$ = 8 TeV. The ∅ symbol indicates no existing search at the LHC.

	e	μ	τ	γ	j	b	t	W	Z	h
e	$\pm\mp$[181],$\pm\pm$[182]	$\pm\pm$[182, 183] $\pm\mp$[184, 183]	[184]	∅	∅	∅	∅	∅	∅	∅
μ		$\pm\mp$[181],$\pm\pm$[182]	[184]	∅	∅	∅	∅	∅	∅	∅
τ			[185]	∅	∅	∅	[186]	∅	∅	∅
γ				[187]	[188, 189, 190]	∅	∅	[191]	[191]	∅
j					[192]	[193]	[194]	[195]	[195]	∅
b						[193]	[196]	∅	∅	∅
t							[197]	[198]	∅	∅
W								[199, 200, 201, 202]	[200, 201, 203, 204]	[205, 206, 207]
Z									[208, 200, 202]	[205, 209, 210, 207]
h										[211, 212, 213, 214]

Table 9.2

	e	μ	τ	γ	j	b	t	W	Z	h
e	$Z', H^{\pm\pm}$	$/\,R, H^{\pm\pm}$	$/\,R, H^{\pm\pm}$	L^*	$LQ, /\,R$	$LQ, /\,R$	$LQ, /\,R$	L^*, ν_{KK}	L^*, e_{KK}	L^*
μ		$Z', H^{\pm\pm}$	$/\,R, H^{\pm\pm}$	L^*	$LQ, /\,R$	$LQ, /\,R$	$LQ, /\,R$	L^*, ν_{KK}	L^*, μ_{KK}	L^*
τ			$Z', H, H^{\pm\pm}$	L^*	$LQ, /\,R$	$LQ, /\,R$	$LQ, /\,R$	L^*, ν_{KK}	L^*, τ_{KK}	L^*
γ				$H, G_{KK}, \mathcal{Q}$	Q^*	Q^*	Q^*	$W_{KK}, \mathcal{Q}$	$H, \mathcal{Q}$	Z_{KK}
j					Z', ρ, G_{KK}	$W', /\,R$	$T', /\,R$	Q^*, Q_{KK}	Q^*, Q_{KK}	Q'
b						Z', H	$W', /\,R, H^{\pm}$	T', Q^*, Q_{KK}	Q^*, Q_{KK}	B'
t							H, G', Z'	T'	T'	T'
W								H, G_{KK}, ρ	$W', \mathcal{Q}$	$H^{\pm}, \mathcal{Q}, \rho$
Z									H, G_{KK}, ρ	A, ρ
h										H, G_{KK}

9.4 Discussion

The data from the LHC are extraordinarily valuable, in that its collection required an enormous investment of financial and human resources and in its potential power to answer outstanding questions of particle physics. However, once those resources are spent and the data are collected, there remain difficult questions regarding how to use it. Experimental analysis of a given final state requires limited human and financial resources, and every search increases field-wide trials factor, making any local excess less globally significant. Therefore, it is necessarily the case that some experimental territory will be left uncovered, and proposals for new experimental searches must have a compelling argument.

Here we have argued that in addition to the usual stable of theoretically-motivated searches, a set of experimentally-motivated searches should be conducted. We propose a set of exclusive 2-body resonance searches, which naturally limits the number of final states and are well matched to experimental capabilities. This is in contrast to the strategy of general searches, which attempt to satisfy a broad set of theory motivations, but do not focus on experimental strengths and suffer a very large trials factor.

The final states with matched objects have been examined, though there remain openings at low- and high-mass regions. More significantly, we find that many of the mismatched pair final states have had no attention, despite the existence of theoretical models and the absence of strong theo-

Table 9.3: The possible QCD and EM quantum numbers of each 2-body resonance, indicated as (**QCD**,**EM**). Alternate quantum number assignments are indicated in parentheses. Round (square) brackets indicate a bosonic (fermionic) resonance. An * indicates that there is no possible initial state for resonant production at the LHC. A $\diamondsuit$ ($\heartsuit$) indicates that this state would lead to $\Delta B = 1$ ($\Delta L = 1$) processes if it possessed a resonant production mode at the LHC from additional couplings to quarks or gluons.

	ℓ	γ	q	g	b	t	W^+	Z	h
ℓ	$(\mathbf{1},2)^*$	$[\mathbf{1},1]^*$	$(\bar{\mathbf{3}},1(4)/3)^{\diamondsuit\heartsuit}$	$[\mathbf{8},1]^*$	$(\bar{\mathbf{3}},4/3)^{\diamondsuit\heartsuit}$	$(\bar{\mathbf{3}},1/3)^{\diamondsuit\heartsuit}$	$[\mathbf{1},0]^*$	$[\mathbf{1},1]^*$	$[\mathbf{1},1]^*$
$\bar{\ell}$	$(\mathbf{1},0)$	$[\mathbf{1},-1]^*$	$(\bar{\mathbf{3}},-2(5^*)/3)^{\diamondsuit\heartsuit}$	$[\mathbf{8},-1]^*$	$(\bar{\mathbf{3}},-2/3)^{\diamondsuit\heartsuit}$	$(\bar{\mathbf{3}},-5/3)^*$	$[\mathbf{1},-2]^*$	$[\mathbf{1},-1]^*$	$[\mathbf{1},-1]^*$
γ	$[\mathbf{1},1]^*$	$(\mathbf{1},0)$	$[\bar{\mathbf{3}},1(-2)/3]$	$(\mathbf{8},0)$	$[\bar{\mathbf{3}},1/3]$	$[\bar{\mathbf{3}},-2/3]$	$(\mathbf{1},-1)$	$(\mathbf{1},0)$	$(\mathbf{1},0)$
q	$(\bar{\mathbf{3}},1(4)/3)^{\diamondsuit\heartsuit}$	$[\bar{\mathbf{3}},1(-2)/3]$	$(\mathbf{3},-1(2)(-4)/3)$	$[\bar{\mathbf{3}},1(-2)/3]$	$(\mathbf{3},-1(2)/3)$	$(\mathbf{3},-1(-4)/3)$	$[\bar{\mathbf{3}},-2(-5^*)/3]$	$[\bar{\mathbf{3}},1(-2)/3]$	$[\bar{\mathbf{3}},1(-2)/3]$
$\bar{q}$	$(\mathbf{3},2(5^*)/3)^{\diamondsuit\heartsuit}$	$[\mathbf{3},-1(2)/3]$	$(\mathbf{1}(\mathbf{8}),0(-1))$	$[\mathbf{3},-1(2)/3]$	$(\mathbf{1}(\mathbf{8}),0(-1))$	$(\mathbf{1}(\mathbf{8}),0(-1))$	$[\mathbf{3},-1(-4^*)/3]$	$[\mathbf{3},-1(2)/3]$	$[\mathbf{3},-1(2)/3]$
g	$[\mathbf{8},1]^*$	$(\mathbf{8},0)$	$[\bar{\mathbf{3}},1(-2)/3]$	$(\mathbf{1}(\mathbf{8}),0)$	$[\bar{\mathbf{3}},1/3]$	$[\bar{\mathbf{3}},-2/3]$	$(\mathbf{8},-1)$	$(\mathbf{8},0)$	$(\mathbf{8},0)$
b		$[\bar{\mathbf{3}},1/3]$	$(\mathbf{3},-1(2)/3)$	$[\bar{\mathbf{3}},1/3]$	$(\mathbf{3},2/3)$	$(\mathbf{3},-1/3)$	$[\bar{\mathbf{3}},-2/3]$	$[\bar{\mathbf{3}},1/3]$	$[\bar{\mathbf{3}},1/3]$
$\bar{b}$			$(\mathbf{1}(\mathbf{8}),0(-1))$	$[\mathbf{3},-1/3]$	$(\mathbf{1}(\mathbf{8}),0)$	$(\mathbf{1}(\mathbf{8}),-1)$	$[\mathbf{3},-4/3]^*$	$[\mathbf{3},-1/3]$	$[\mathbf{3},-1/3]$
t				$[\bar{\mathbf{3}},-2/3]$	$(\mathbf{3},-1/3)$	$(\mathbf{3},-4/3)$	$[\bar{\mathbf{3}},-5/3]^*$	$[\bar{\mathbf{3}},-2/3]$	$[\bar{\mathbf{3}},-2/3]$
$\bar{t}$					$(\mathbf{1}(\mathbf{8}),1)$	$(\mathbf{1}(\mathbf{8}),0)$	$[\mathbf{3},-1/3]$	$[\mathbf{3},2/3]$	$[\mathbf{3},2/3]$
W^+						$[\bar{\mathbf{3}},-5/3]^*$	$(\mathbf{1},-2)^*$	$(\mathbf{1},-1)$	$(\mathbf{1},-1)$
W^-							$(\mathbf{1},0)$	$(\mathbf{1},1)$	$(\mathbf{1},1)$
Z								$(\mathbf{1},0)$	$(\mathbf{1},0)$
h									$(\mathbf{1},0)$

retical constraints.

Chapter 10

Concluding Words: Anomalous Resonance as a Question

Particle physics has come a long way since its early days. Since the discovery of the Higgs Boson in 2012, the Standard Model is considered completed. But human's quest to understand fundamental physics is far from over. Many existing issues in Standard Model points to a picture out there unknown, yet to be understood. This evidence, especially those concerning Dark Matter, drove the resonance search analyses presented in Chapter 7 and Chapter 8. However, as a highly distinguishable signature, resonances hunting offers much more than a tool to hunt for a specific candidate. In the age where most exotic and SUSY searches returned empty results, what ought to concern physicists regarding data is no longer merely what can be searched for, but also what can be *asked*: what questions can be asked of data for them to reveal to us what we do not know? This chapter summarizes some directions that can be taken in the resonance hunting regime for future studies.

10.1 Unexplored Landscape of the Two Body Resonances

Chapter 9 explored uncovered two-body final states in resonance hunting in detail. The paper has since been superseded by newer results [215]. The surveys offer an overview of all two-body final states that are left unsearched for in collider physics that could provide a wealth of sources for possible places to look for new physics signatures.

10.2 Gaussian Process as a Background Modeling Method

The Gaussian Process-based background estimation method is currently being finalized in ATLAS with the dimuon analysis in Chapter 8. It provides a more flexible method better suited for high luminosity for smooth background modeling for other resonance hunting analyses where MC is limited. The method offers the advantage of being *generalizable* for any final state with a smooth background estimation in the signal region. The method will be applicable to many other future analyses.

10.3 Data Scouting

Due to limited bandwidth, the trigger described in Chapter 8 set a lower bound in the mass of the resonance that could be searched for. Searching for a signal with initial state radiation mitigates this but it also results in a lowered sensitivity to the signal. Data scouting is a method proposed to create a special triggering stream and object to mitigate the limit triggering bandwidth by storing only partial events. Only information directly related to the analysis will be stored. Currently, the dimuon data scouting analysis is under study in ATLAS and will be a future area with promising improved sensitivity.

10.4 Anomaly Detection for Resonances with Machine Learning Method

The concept of "model-independent" searches is not unfamiliar to LHC. Searches for new particles often include model-independent results in the form of excesses beyond certain statistical significance LHC also has its dedicated general search [216]. However, these current approaches are not truly model-independent: they are either signal model-dependent in the sensitivity optimal kinematic cut for targeted search or LHC background dependent in the general search. Search sensitivity is greatly diminished if the anomaly is not as predicted by the signal or background models. An improved method will instead teach data to perform optimal selection on its own based only on the anomaly observed in data. One recent proposal is the weakly supervised Classification Without Labels (CWoLa) hunting method [217]. This technique discards the usual supervised Signal-over-background (S/B) kinematic strategy, where the optimal selection is made based on the maximal S/B ratio of a specific model combination. In utilizing CWoLa for resonance hunting, the bump-like signal produces a signal-rich center-band and signal-deprived side-bands optimal for optimal sensitivity kinematic cuts training. If a new particle is embedded in the dataset, CWoLa training will produce a selection cut that maximizes events in the central-band-bump without any underlying

S/B model assumptions. The data is made to reveal surprising anomalies on its own from the data alone. The existing two-quark final state resonance CWoLa search [218] to other final states including muons, photons, and other uncovered resonance signatures. While the dijet analysis has proven the feasibility of the method in ATLAS, many detailed technical aspects, further generalizations, and expansions into larger feature spaces must still be performed. The new analyses on muon and photon final states will go beyond the predecessor by focusing the training on additional features including the jet substructure of the ISR jet. More complicated signal topologies, where the primary resonant decay object can be composite, can also be explored using simpler muon/photon final state objects. The CWoLa model-independent searches will serve as complementary additions to current physics analyses' model-dependent and independent search methods, and it will push sensitivity into new regions with attuned understanding driven by the data itself.

Bibliography

[1] HG Plato. *Republic*. Princeton University Press, 1961 (cit. on p. 0).

[2] Immanuel Kant. "Critique of pure reason. 1781". In: *Modern Classical Philosophers, Cambridge, MA: Houghton Mifflin* (1908), pp. 370–456 (cit. on p. 0).

[3] Marian David. "The Correspondence Theory of Truth". In: *The Stanford Encyclopedia of Philosophy*. Ed. by Edward N. Zalta. Winter 2020. Metaphysics Research Lab, Stanford University, 2020 (cit. on p. 0).

[4] Alain Badiou. *Being and event*. A&C Black, 2007 (cit. on p. 1).

[5] Thomas Kuhn. *The structure of scientific revolutions*. Princeton University Press, 2021 (cit. on p. 1).

[6] Alain Badiou. *Ethics: An essay on the understanding of evil*. Verso, 2002 (cit. on p. 1).

[7] Willy Sarlet and Frans Cantrijn. "Generalizations of Noether's theorem in classical mechanics". In: *Siam Review* 23.4 (1981), pp. 467–494 (cit. on p. 4).

[8] Daniel Joseph Antrim. "Sweet Little Nothings; or, Searching for a Pair of Stops, Va Pair of Higgs Bosons, and a Pair of New Small Wheels for the Upgrade of the Forward Muon System of the ATLAS Detector at CERN". Presented 23 Oct 2019. 2019. URL: `https://cds.cern.ch/record/2699575` (cit. on p. 6).

[9] Michael E Peskin. *An introduction to quantum field theory*. CRC press, 2018 (cit. on pp. 7, 8, 9).

[10] Peter W Higgs. "Broken symmetries and the masses of gauge bosons". In: *Physical Review Letters* 13.16 (1964), p. 508 (cit. on p. 7).

[11] Diego Fasoli, Anna Cattani, and Stefano Panzeri. "The complexity of dynamics in small neural circuits". In: (Jan. 2016). DOI: `10.5281/zenodo.55275` (cit. on p. 7).

[12] Yoichiro Nambu. "Quasi-Particles and Gauge Invariance in the Theory of Superconductivity". In: *Phys. Rev.* 117 (3 1960), pp. 648–663. DOI: `10.1103/PhysRev.117.648`. URL: `https://link.aps.org/doi/10.1103/PhysRev.117.648` (cit. on p. 9).

[13] Wikipedia contributors. *Standard Model — Wikipedia, The Free Encyclopedia*. [Online; accessed 17-December-2021]. 2021. URL: https://en.wikipedia.org/w/index.php?title=Standard_Model&oldid=1060203113 (cit. on p. 11).

[14] Steven Weinstein and Dean Rickles. "Quantum Gravity". In: *The Stanford Encyclopedia of Philosophy*. Ed. by Edward N. Zalta. Fall 2021. Metaphysics Research Lab, Stanford University, 2021 (cit. on p. 11).

[15] Ya B Zel'Dovich. "The cosmological constant and the theory of elementary particles". In: *Soviet Physics Uspekhi* 11.3 (1968), p. 381 (cit. on p. 12).

[16] P. A. R. Ade et al. "Planck2015 results". In: *Astronomy & Astrophysics* 594 (2016), A13. ISSN: 1432-0746. DOI: 10.1051/0004-6361/201525830. URL: http://dx.doi.org/10.1051/0004-6361/201525830 (cit. on p. 12).

[17] Howard E. Haber and Laurel Stephenson Haskins. "Supersymmetric Theory and Models". In: *Anticipating the Next Discoveries in Particle Physics* (2018). DOI: 10.1142/9789813233348_0006. URL: http://dx.doi.org/10.1142/9789813233348_0006 (cit. on p. 12).

[18] C. Abel et al. "Measurement of the Permanent Electric Dipole Moment of the Neutron". In: *Phys. Rev. Lett.* 124 (8 2020), p. 081803. DOI: 10.1103/PhysRevLett.124.081803. URL: https://link.aps.org/doi/10.1103/PhysRevLett.124.081803 (cit. on p. 13).

[19] R.D. Peccei and Helen Quinn. "CP Conservation in the Presence of Pseudoparticles". In: *Physical Review Letters - PHYS REV LETT* 38 (June 1977), pp. 1440–1443. DOI: 10.1103/PhysRevLett.38.1440 (cit. on p. 13).

[20] Peter AR Ade et al. "Planck 2015 results-xiii. cosmological parameters". In: *Astronomy & Astrophysics* 594 (2016), A13 (cit. on p. 14).

[21] F. Zwicky. "On the Masses of Nebulae and of Clusters of Nebulae". In: *Astrophys. J.* 86 (1937), pp. 217–246. DOI: 10.1086/143864 (cit. on p. 16).

[22] Horace W. Babcock. "The rotation of the Andromeda Nebula". In: *Lick Observatory Bulletin* 498 (Jan. 1939), pp. 41–51. DOI: 10.5479/ADS/bib/1939LicOB.19.41B (cit. on p. 16).

[23] Jan Hendrik Oort. "The structure of the cloud of comets surrounding the Solar System and a hypothesis concerning its origin". In: *Bulletin of the Astronomical Institutes of the Netherlands* 11 (1950), pp. 91–110 (cit. on p. 16).

[24] Miguel Escudero et al. "Toward (finally!) ruling out Z and Higgs mediated dark matter models". In: *Journal of Cosmology and Astroparticle Physics* 2016.12 (2016), 029–029. ISSN: 1475-7516. DOI: 10.1088/1475-7516/2016/12/029. URL: http://dx.doi.org/10.1088/1475-7516/2016/12/029 (cit. on p. 16).

[25] Vera C Rubin and W Kent Ford Jr. "Rotation of the Andromeda nebula from a spectroscopic survey of emission regions". In: *The Astrophysical Journal* 159 (1970), p. 379 (cit. on p. 17).

[26] Kenneth C Freeman. "On the disks of spiral and S0 galaxies". In: *The Astrophysical Journal* 160 (1970), p. 811 (cit. on p. 17).

[27] Asher Yahalom. "The Effect of Retardation on Galactic Rotation Curves". In: *Journal of Physics: Conference Series* 1239 (May 2019), p. 012006. DOI: 10.1088/1742-6596/1239/1/012006 (cit. on p. 18).

[28] A. Popolo. "Non-Baryonic Dark Matter in Cosmology". In: *International Journal of Modern Physics D* 23 (May 2013). DOI: 10.1142/S0218271814300055 (cit. on pp. 19, 20).

[29] David M Wittman et al. "Detection of weak gravitational lensing distortions of distant galaxies by cosmic dark matter at large scales". In: *nature* 405.6783 (2000), pp. 143–148 (cit. on p. 19).

[30] DJ Fixsen. "The temperature of the cosmic microwave background". In: *The Astrophysical Journal* 707.2 (2009), p. 916 (cit. on p. 20).

[31] Yashar Akrami et al. "Planck 2018 results. I. Overview and the cosmological legacy of Planck". In: (July 2018) (cit. on p. 21).

[32] Antonio Boveia and Caterina Doglioni. "Dark matter searches at colliders". In: *Annual Review of Nuclear and Particle Science* 68 (2018), pp. 429–459 (cit. on p. 22).

[33] Scott W Randall et al. "Constraints on the self-interaction cross section of dark matter from numerical simulations of the merging galaxy cluster 1E 0657–56". In: *The Astrophysical Journal* 679.2 (2008), p. 1173 (cit. on p. 22).

[34] Scott Dodelson and Lawrence M Widrow. "Sterile neutrinos as dark matter". In: *Physical Review Letters* 72.1 (1994), p. 17 (cit. on p. 23).

[35] FP An et al. "Search for a light sterile neutrino at Daya Bay". In: *Physical review letters* 113.14 (2014), p. 141802 (cit. on p. 23).

[36] Hin Lok Henoch Wong, Daya Bay Collaboration, et al. "Search for a Light Sterile Neutrino at Daya Bay". In: *Journal of Physics: Conference Series*. Vol. 888. 1. IOP Publishing. 2017, p. 012130 (cit. on p. 23).

[37] I Alekseev et al. "Search for sterile neutrinos at the DANSS experiment". In: *Physics Letters B* 787 (2018), pp. 56–63 (cit. on p. 23).

[38] Roberto D Peccei and Helen R Quinn. "CP Conservation in the Presence of Instantons". In: *Phys. Rev. Lett* 38.1440-1443 (1977), p. 328 (cit. on p. 23).

[39] Elena Aprile et al. "Excess electronic recoil events in XENON1T". In: *Physical Review D* 102.7 (2020), p. 072004 (cit. on pp. 23, 25).

[40] P. S. Bhupal Dev, Anupam Mazumdar, and Saleh Qutub. "Constraining non-thermal and thermal properties of Dark Matter". In: *Frontiers in Physics* 2 (2014). ISSN: 2296-424X. DOI: 10.3389/fphy.2014.00026. URL: http://dx.doi.org/10.3389/fphy.2014.00026 (cit. on p. 23).

[41] Edward Kolb and Michael Turner. "The Early Universe". In: *Front. Phys., Vol. 69,* -1 (Feb. 1983). DOI: 10.1038/294521a0 (cit. on p. 24).

[42] DN McKinsey, LZ Collaboration, et al. "The LZ dark matter experiment". In: *Journal of Physics: Conference Series*. Vol. 718. 4. IOP Publishing. 2016, p. 042039 (cit. on p. 25).

[43] R. Agnese et al. "New Results from the Search for Low-Mass Weakly Interacting Massive Particles with the CDMS Low Ionization Threshold Experiment". In: *Physical Review Letters* 116.7 (2016). ISSN: 1079-7114. DOI: 10.1103/physrevlett.116.071301. URL: http://dx.doi.org/10.1103/PhysRevLett.116.071301 (cit. on p. 25).

[44] G. Angloher et al. "Results on low mass WIMPs using an upgraded CRESST-II detector". In: *The European Physical Journal C* 74.12 (2014). ISSN: 1434-6052. DOI: 10.1140/epjc/s10052-014-3184-9. URL: http://dx.doi.org/10.1140/epjc/s10052-014-3184-9 (cit. on p. 25).

[45] R. Bernabei et al. "The DAMA/LIBRA apparatus". In: *Nuclear Instruments and Methods in Physics Research Section A: Accelerators, Spectrometers, Detectors and Associated Equipment* 592.3 (2008), 297–315. ISSN: 0168-9002. DOI: 10.1016/j.nima.2008.04.082. URL: http://dx.doi.org/10.1016/j.nima.2008.04.082 (cit. on p. 25).

[46] Andrea Albert et al. "Searching for dark matter annihilation in recently discovered Milky Way satellites with Fermi-LAT". In: *The Astrophysical Journal* 834.2 (2017), p. 110 (cit. on p. 25).

[47] Felix Aharonian et al. "HESS observations of the Galactic Center region and their possible dark matter interpretation". In: *Physical Review Letters* 97.22 (2006), p. 221102 (cit. on p. 25).

[48] Jalal Abdallah et al. "Simplified Models for Dark Matter Searches at the LHC". In: *Phys. Dark Universe* 9-10 (2015). v3: Fixed typo in eqns 14 & 15, 8–23. 16 p. DOI: 10.1016/j.dark.2015.08.001. arXiv: 1506.03116. URL: http://cds.cern.ch/record/2024101 (cit. on p. 26).

[49] Giorgio Busoni et al. "On the validity of the effective field theory for dark matter searches at the LHC, part II: complete analysis for the s-channel". In: *Journal of Cosmology and Astroparticle Physics* 2014.06 (2014), 060–060. ISSN: 1475-7516. DOI: 10.1088/1475-7516/2014/06/060. URL: http://dx.doi.org/10.1088/1475-7516/2014/06/060 (cit. on p. 27).

[50] G.C. Branco et al. "Theory and phenomenology of two-Higgs-doublet models". In: *Physics Reports* 516.1-2 (2012), 1–102. ISSN: 0370-1573. DOI: 10.1016/j.physrep.2012.02.002. URL: http://dx.doi.org/10.1016/j.physrep.2012.02.002 (cit. on p. 27).

[51] CSABA CSÁKI. "THE MINIMAL SUPERSYMMETRIC STANDARD MODEL". In: *Modern Physics Letters A* 11.08 (1996), 599–613. ISSN: 1793-6632. DOI: 10.1142/s021773239600062x. URL: http://dx.doi.org/10.1142/S021773239600062X (cit. on p. 27).

[52] Antonio Boveia and Caterina Doglioni. "Dark Matter Searches at Colliders". In: *Annual Review of Nuclear and Particle Science* 68.1 (2018), 429–459. ISSN: 1545-4134. DOI: 10.1146/annurev-nucl-101917-021008. URL: http://dx.doi.org/10.1146/annurev-nucl-101917-021008 (cit. on p. 28).

[53] Daniel Abercrombie et al. "Dark Matter benchmark models for early LHC Run-2 Searches: Report of the ATLAS/CMS Dark Matter Forum". In: *Physics of the Dark Universe* 27 (2020), p. 100371. ISSN: 2212-6864. DOI: 10.1016/j.dark.2019.100371. URL: http://dx.doi.org/10.1016/j.dark.2019.100371 (cit. on p. 28).

[54] Juliette Alimena et al. "Searching for long-lived particles beyond the Standard Model at the Large Hadron Collider". In: *Journal of Physics G: Nuclear and Particle Physics* 47.9 (2020), p. 090501. ISSN: 1361-6471. DOI: 10.1088/1361-6471/ab4574. URL: http://dx.doi.org/10.1088/1361-6471/ab4574 (cit. on p. 30).

[55] A. Airapetian et al. "ATLAS: Detector and physics performance technical design report. Volume 2". In: (May 1999) (cit. on pp. 31, 33, 35).

[56] Oliver Sim Brüning et al. *LHC Design Report*. CERN Yellow Reports: Monographs. Geneva: CERN, 2004. DOI: 10.5170/CERN-2004-003-V-1. URL: https://cds.cern.ch/record/782076 (cit. on pp. 31, 32, 37, 38).

[57] Zenrō Hioki. "How Does the Discovery of Z Boson Improve the Prediction for W±Boson Mass?" In: *Progress of Theoretical Physics* 68.6 (1982), pp. 2134–2140 (cit. on p. 31).

[58] Serguei Chatrchyan et al. "Observation of a new boson at a mass of 125 GeV with the CMS experiment at the LHC". In: *Physics Letters B* 716.1 (2012), pp. 30–61 (cit. on p. 31).

[59] Tim Berners-Lee et al. "The world-wide web". In: *Communications of the ACM* 37.8 (1994), pp. 76–82 (cit. on p. 31).

[60] G. L. Bayatian et al. "CMS Physics: Technical Design Report Volume 1: Detector Performance and Software". In: (2006) (cit. on p. 33).

[61] RICH LHCb. "Technical Design Report". In: *CERN/LHCC* 11 (2001), p. 2001 (cit. on p. 33).

[62] P Cortese. *ALICE transition-radiation detector: Technical Design Report*. Technical design report. ALICE. Geneva: CERN, 2001. URL: https://cds.cern.ch/record/519145 (cit. on p. 33).

[63] O Adriani et al. *LHCf experiment: Technical Design Report*. Technical design report. LHCf. Geneva: CERN, 2006. URL: https://cds.cern.ch/record/926196 (cit. on p. 33).

[64] Akitaka Ariga et al. *Technical Proposal for FASER: ForwArd Search ExpeRiment at the LHC*. Tech. rep. Geneva: CERN, 2018. arXiv: 1812.09139. URL: https://cds.cern.ch/record/2651328 (cit. on p. 33).

[65] James Pinfold et al. *Technical Design Report of the MoEDAL Experiment*. Tech. rep. 2009. URL: https://cds.cern.ch/record/1181486 (cit. on p. 33).

[66] V. Berardi et al. “TOTEM: Technical design report. Total cross section, elastic scattering and diffraction dissociation at the Large Hadron Collider at CERN”. In: (Jan. 2004) (cit. on p. 33).

[67] Fabienne Marcastel. “CERN’s Accelerator Complex. La chaîne des accélérateurs du CERN”. In: (2013). General Photo. URL: http://cds.cern.ch/record/1621583 (cit. on p. 34).

[68] Thomas Sven Pettersson and P Lefèvre. *The Large Hadron Collider: conceptual design*. Tech. rep. 1995. URL: https://cds.cern.ch/record/291782 (cit. on p. 36).

[69] Joao Pequenao. “Computer generated image of the whole ATLAS detector”. 2008. URL: https://cds.cern.ch/record/1095924 (cit. on p. 39).

[70] The ATLAS Collaboration et al. “The ATLAS Experiment at the CERN Large Hadron Collider”. In: 3.08 (2008), S08003–S08003. DOI: 10.1088/1748-0221/3/08/s08003. URL: https://doi.org/10.1088/1748-0221/3/08/s08003 (cit. on p. 39).

[71] Wikipedia contributors. *Pseudorapidity — Wikipedia, The Free Encyclopedia*. [Online; accessed 5-November-2021]. 2021. URL: https://en.wikipedia.org/w/index.php?title=Pseudorapidity&oldid=1052183914 (cit. on p. 40).

[72] Joao Pequenao. “Computer generated image of the ATLAS inner detector”. 2008. URL: https://cds.cern.ch/record/1095926 (cit. on pp. 41, 42).

[73] Joao Pequenao. “Computer Generated image of the ATLAS calorimeter”. 2008. URL: https://cds.cern.ch/record/1095927 (cit. on p. 43).

[74] Joao Pequenao. “Computer generated image of the ATLAS Muons subsystem”. 2008. URL: https://cds.cern.ch/record/1095929 (cit. on pp. 44, 45).

[75] Sascha Mehlhase. “ATLAS detector slice (and particle visualisations)”. In: (2021). URL: https://cds.cern.ch/record/2770815 (cit. on pp. 47, 57).

[76] T Cornelissen et al. “The new ATLAS track reconstruction (NEWT)”. In: *Journal of Physics: Conference Series* 119 (July 2008), p. 032014. DOI: 10.1088/1742-6596/119/3/032014 (cit. on pp. 47, 48).

[77] E. Bouhova-Thacker et al. “Vertex reconstruction in the ATLAS experiment at the LHC”. In: *2008 IEEE Nuclear Science Symposium Conference Record*. 2008, pp. 1720–1727. DOI: 10.1109/NSSMIC.2008.4774734 (cit. on p. 48).

[78] Aad G. et al. “Muon reconstruction and identification efficiency in ATLAS using the full Run 2 *pp* collision data set at $\sqrt{s}$ = 13 TeV”. In: *Eur. Phys. J., C* 81 (2020), 578. 44 p. DOI: 10.1140/epjc/s10052-021-09233-2. arXiv: 2012.00578. URL: https://cds.cern.ch/record/2746302 (cit. on pp. 49, 52, 54).

[79] Experiment ATLAS. “An ATLAS event with 4 muons”. General Photo. 2014. URL: https://cds.cern.ch/record/1697053 (cit. on p. 49).

[80] G. Aad et al. "Muon reconstruction performance of the ATLAS detector in proton–proton collision data at $\sqrt{s}$ s =13 TeV". In: *The European Physical Journal C* 76.5 (2016). ISSN: 1434-6052. DOI: 10.1140/epjc/s10052-016-4120-y. URL: http://dx.doi.org/10.1140/epjc/s10052-016-4120-y (cit. on pp. 49, 50, 51).

[81] Georges Aad et al. "Muon reconstruction and identification efficiency in ATLAS using the full Run 2 *pp* collision data set at $\sqrt{s}$ = 13 TeV". In: (2020). 60 pages in total, author list starting page 44, 23 figures, 3 tables. Submitted to journal EPJC. All figures including auxiliary figures are available at https://atlas.web.cern.ch/Atlas/GROUPS/PHYSICS/PAPERS/MUON-2018-03/. DOI: 10.3204/PUBDB-2020-05158. arXiv: 2012.00578. URL: https://bib-pubdb1.desy.de/record/453350 (cit. on p. 53).

[82] A. Schwartzman et al. "Image Processing, Computer Vision, and Deep Learning: new approaches to the analysis and physics interpretation of LHC events". In: *Journal of Physics: Conference Series* 762 (Oct. 2016), p. 012035. DOI: 10.1088/1742-6596/762/1/012035 (cit. on p. 55).

[83] Matteo Cacciari, Gavin P Salam, and Gregory Soyez. "The anti-ktjet clustering algorithm". In: *Journal of High Energy Physics* 2008.04 (2008), 063–063. ISSN: 1029-8479. DOI: 10.1088/1126-6708/2008/04/063. URL: http://dx.doi.org/10.1088/1126-6708/2008/04/063 (cit. on p. 56).

[84] *High-mass di-photon resonances:The first 2016 atlas results* (cit. on p. 57).

[85] W Lampl et al. *Calorimeter Clustering Algorithms: Description and Performance*. Tech. rep. Geneva: CERN, 2008. URL: https://cds.cern.ch/record/1099735 (cit. on p. 58).

[86] M. Aaboud et al. "Electron and photon energy calibration with the ATLAS detector using 2015–2016 LHC proton-proton collision data". In: *Journal of Instrumentation* 14.03 (2019), P03017–P03017. ISSN: 1748-0221. DOI: 10.1088/1748-0221/14/03/p03017. URL: http://dx.doi.org/10.1088/1748-0221/14/03/P03017 (cit. on pp. 58, 59).

[87] J. E. Augustin et al. "Discovery of a Narrow Resonance in e^+e^- Annihilation". In: *Phys. Rev. Lett.* 33 (23 1974), pp. 1406–1408. DOI: 10.1103/PhysRevLett.33.1406. URL: https://link.aps.org/doi/10.1103/PhysRevLett.33.1406 (cit. on p. 60).

[88] J. J. Aubert et al. "Experimental Observation of a Heavy Particle *J*". In: *Phys. Rev. Lett.* 33 (23 1974), pp. 1404–1406. DOI: 10.1103/PhysRevLett.33.1404. URL: https://link.aps.org/doi/10.1103/PhysRevLett.33.1404 (cit. on p. 60).

[89] S. W. Herb et al. "Observation of a Dimuon Resonance at 9.5-GeV in 400-GeV Proton-Nucleus Collisions". In: *Phys. Rev. Lett.* 39 (1977), pp. 252–255. DOI: 10.1103/PhysRevLett.39.252 (cit. on p. 60).

[90] Geoffrey T J Arnison et al. "Experimental observation of isolated large transverse energy electrons with associated missing energy at $\sqrt{s}$ = 540GeV". In: *Phys. Lett. B* 122 (1983), 103–116. 31 p. DOI: 10.5170/CERN-1983-004.123. URL: https://cds.cern.ch/record/142059.

[91] Wolfgang Hollik, Fridger Schrempp, and Barbara Schrempp. "Composite scalars in e+ e-collisions and radiative Z decays". In: *Physics Letters B* 140.5-6 (1984), pp. 424–430 (cit. on p. 60).

[92] Torbjörn Sjöstrand, Stephen Mrenna, and Peter Skands. "A brief introduction to PYTHIA 8.1". In: *Computer Physics Communications* 178.11 (2008), 852–867. ISSN: 0010-4655. DOI: 10.1016/j.cpc.2008.01.036. URL: http://dx.doi.org/10.1016/j.cpc.2008.01.036 (cit. on p. 61).

[93] Carlo Oleari. "The powheg-box". In: *arXiv preprint arXiv:1007.3893* (2010) (cit. on p. 61).

[94] Z Nagy. *NLOJET++ Home page* (cit. on p. 61).

[95] S et. al Agostinelli. "GEANT4–a simulation toolkikt. GEANT4. A Simulation toolkit". In: *Nucl. Instrum. Methods Phys. Res., A* 506 (2002), 250–303. 54 p. DOI: 10.1016/S0168-9002(03)01368-8. URL: https://cds.cern.ch/record/602040 (cit. on p. 61).

[96] Meghan Frate et al. *Modeling Smooth Backgrounds and Generic Localized Signals with Gaussian Processes*. 2017. arXiv: 1709.05681 [physics.data-an] (cit. on pp. 63, 67, 68, 76, 77).

[97] *Recommendations for the Modeling of Smooth Backgrounds*. Tech. rep. Geneva: CERN, 2020. URL: https://cds.cern.ch/record/2743717 (cit. on pp. 63, 64, 69, 103, 104, 105).

[98] Katherine Pachal. "Search for new physics in the dijet invariant mass spectrum at 8 TeV". Presented 01 Jun 2015. 2015. URL: https://cds.cern.ch/record/2063032 (cit. on pp. 63, 72).

[99] J. Alitti et al. "A Measurement of two jet decays of the W and Z bosons at the CERN $\bar{p}p$ collider". In: *Z. Phys. C* 49 (1991), pp. 17–28. DOI: 10.1007/BF01570793 (cit. on p. 63).

[100] F. Abe et al. "Search for New Particles Decaying to Dijets inpp¯Collisions at s=1.8TeV". In: *Physical Review Letters* 74.18 (1995), 3538–3543. ISSN: 1079-7114. DOI: 10.1103/physrevlett.74.3538. URL: http://dx.doi.org/10.1103/PhysRevLett.74.3538 (cit. on p. 64).

[101] F. Abe et.al. "Search for new particles decaying to dijets at CDF". English (US). In: *Physical Review D - Particles, Fields, Gravitation and Cosmology* 55.9 (1997), R5263–R5268. ISSN: 1550-7998. DOI: 10.1103/PhysRevD.55.R5263 (cit. on p. 64).

[102] T. Aaltonen et al. "Search for new particles decaying into dijets in proton-antiproton collisions ats=1.96 TeV". In: *Physical Review D* 79.11 (2009). ISSN: 1550-2368. DOI: 10.1103/physrevd.79.112002. URL: http://dx.doi.org/10.1103/PhysRevD.79.112002 (cit. on p. 64).

[103] G. Aad et al. "Search for microscopic black holes and string balls in final states with leptons and jets with the ATLAS detector at s $\sqrt{s}$ = 8 TeV". In: *Journal of High Energy Physics* 2014.8 (2014). ISSN: 1029-8479. DOI: 10.1007/jhep08(2014)103. URL: http://dx.doi.org/10.1007/JHEP08(2014)103 (cit. on pp. 64, 93, 94).

[104] Carl Edward Rasmussen. "Gaussian processes in machine learning". In: *Summer school on machine learning*. Springer. 2003, pp. 63–71 (cit. on p. 67).

[105] Sang Gyu Kwak and Jong Hae Kim. "Central limit theorem: the cornerstone of modern statistics". In: *Korean journal of anesthesiology* 70.2 (2017), p. 144 (cit. on p. 67).

[106] Georgios Choudalakis. *On hypothesis testing, trials factor, hypertests and the BumpHunter*. 2011. arXiv: 1101.0390 [physics.data-an] (cit. on p. 69).

[107] Glen Cowan et al. "Asymptotic formulae for likelihood-based tests of new physics". In: *The European Physical Journal C* 71.2 (2011). ISSN: 1434-6052. DOI: 10.1140/epjc/s10052-011-1554-0. URL: http://dx.doi.org/10.1140/epjc/s10052-011-1554-0 (cit. on pp. 75, 76).

[108] M. Aaboud et al. "Search for low-mass resonances decaying into two jets and produced in association with a photon using pp collisions at s=13 TeV with the ATLAS detector". In: *Physics Letters B* 795 (2019), 56–75. ISSN: 0370-2693. DOI: 10.1016/j.physletb.2019.03.067. URL: http://dx.doi.org/10.1016/j.physletb.2019.03.067 (cit. on p. 79).

[109] Mikael Chala et al. "Constraining dark sectors with monojets and dijets". In: *JHEP* 07 (2015), p. 089. DOI: 10.1007/JHEP07(2015)089. arXiv: 1503.05916 [hep-ph] (cit. on pp. 79, 80).

[110] D. Abercrombie et al. *Dark matter benchmark models for early LHC Run-2 searches: report of the ATLAS/CMS Dark Matter Forum*. 2015. arXiv: 1507.00966 [hep-ex] (cit. on pp. 79, 80, 87).

[111] UA1 Collaboration. "Angular distributions and structure functions from two jet events at the CERN SPS $p\bar{p}$ collider". In: *Phys. Lett. B* 136 (1984), p. 294. DOI: 10.1016/0370-2693(84)91164-X (cit. on p. 79).

[112] UA1 Collaboration. "Two jet mass distributions at the CERN $p\bar{p}$ Collider". In: *Phys. Lett. B* 209 (1988), pp. 127–134. DOI: 10.1016/0370-2693(88)91843-6 (cit. on p. 79).

[113] UA2 Collaboration. "Measurement of jet production properties at the CERN $p\bar{p}$ collider". In: *Phys. Lett. B* 144 (1984), pp. 283–290. DOI: 10.1016/0370-2693(84)91822-7 (cit. on p. 79).

[114] CDF Collaboration. "Search for new particles decaying into dijets in proton-antiproton collisions at $\sqrt{s}$ = 1.96 TeV". In: *Phys. Rev. D* 79 (2009), p. 112002. DOI: 10.1103/PhysRevD.79.112002. arXiv: 0812.4036 [hep-ex] (cit. on pp. 79, 84).

[115] UA2 Collaboration. "A Measurement of two jet decays of the W and Z bosons at the CERN $\bar{p}p$ collider". In: *Z. Phys. C* 49 (1991), pp. 17–28. DOI: 10.1007/BF01570793 (cit. on pp. 79, 84).

[116] ATLAS Collaboration. "Search for New Particles in Two-Jet Final States in 7 TeV Proton–Proton Collisions with the ATLAS Detector at the LHC". In: *Phys. Rev. Lett.* 105 (2010), p. 161801. DOI: 10.1103/PhysRevLett.105.161801. arXiv: 1008.2461 [hep-ex] (cit. on pp. 79, 84).

[117] CMS Collaboration. "Search for Dijet Resonances in 7 TeV pp Collisions at CMS". In: *Phys. Rev. Lett.* 105 (2010), p. 211801. DOI: 10.1103/PhysRevLett.105.211801. arXiv: 1010.0203 [hep-ex] (cit. on p. 79).

[118] CMS Collaboration. "Measurement of Dijet Angular Distributions and Search for Quark Compositeness in pp Collisions at $\sqrt{s}$ = 7 TeV". In: *Phys. Rev. Lett.* 106 (2011), p. 201804. DOI: 10.1103/PhysRevLett.106.201804. arXiv: 1102.2020 [hep-ex] (cit. on p. 79).

[119] CMS Collaboration. "Search for resonances in the dijet mass spectrum from 7 TeV pp collisions at CMS". In: *Phys. Lett. B* 704 (2011), p. 123. DOI: 10.1016/j.physletb.2011.09.015. arXiv: 1107.4771 [hep-ex] (cit. on pp. 79, 84).

[120] ATLAS Collaboration. "A search for new physics in dijet mass and angular distributions in pp collisions at $\sqrt{s}$ = 7 TeV measured with the ATLAS detector". In: *New J. Phys.* 13 (2011), p. 053044. DOI: 10.1088/1367-2630/13/5/053044. arXiv: 1103.3864 [hep-ex] (cit. on pp. 79, 88).

[121] ATLAS Collaboration. "Search for new physics in the dijet mass distribution using 1 fb^{-1} of pp collision data at $\sqrt{s}$ = 7 TeV collected by the ATLAS detector". In: *Phys. Lett. B* 708 (2012), p. 37. DOI: 10.1016/j.physletb.2012.01.035. arXiv: 1108.6311 [hep-ex] (cit. on p. 79).

[122] ATLAS Collaboration. "ATLAS search for new phenomena in dijet mass and angular distributions using pp collisions at $\sqrt{s}$ = 7 TeV". In: *JHEP* 01 (2013), p. 029. DOI: 10.1007/JHEP01(2013)029. arXiv: 1210.1718 [hep-ex] (cit. on p. 79).

[123] ATLAS Collaboration. "Search for new phenomena in the dijet mass distribution using pp collision data at $\sqrt{s}$ = 8 TeV with the ATLAS detector". In: *Phys. Rev. D* 91 (2015), p. 052007. DOI: 10.1103/PhysRevD.91.052007. arXiv: 1407.1376 [hep-ex] (cit. on pp. 79, 84).

[124] CMS Collaboration. "Search for narrow resonances using the dijet mass spectrum in pp collisions at $\sqrt{s}$ = 8 TeV". In: *Phys. Rev. D* 87 (2013), p. 114015. DOI: 10.1103/PhysRevD.87.114015. arXiv: 1302.4794 [hep-ex] (cit. on p. 79).

[125] ATLAS Collaboration. "Search for new phenomena in dijet mass and angular distributions from pp collisions at $\sqrt{s}$ = 13 TeV with the ATLAS detector". In: *Phys. Lett. B* 754 (2016), p. 302. DOI: 10.1016/j.physletb.2016.01.032. arXiv: 1512.01530 [hep-ex] (cit. on pp. 79, 84, 87).

[126] CMS Collaboration. "Search for new phenomena in events with high jet multiplicity and low missing transverse momentum in proton–proton collisions at $\sqrt{s}$ = 8 TeV". In: *Phys. Lett. B* 770 (2017), p. 257. DOI: 10.1016/j.physletb.2017.01.073. arXiv: 1608.01224 [hep-ex] (cit. on p. 79).

[127] CMS Collaboration. "Search for narrow and broad dijet resonances in proton–proton collisions at $\sqrt{s}$ = 13 TeV and constraints on dark matter mediators and other new particles". In: *JHEP* 08 (2018), p. 130. DOI: 10.1007/JHEP08(2018)130. arXiv: 1806.00843 [hep-ex] (cit. on p. 79).

[128] CMS Collaboration. "Search for dijet resonances in proton–proton collisions at $\sqrt{s}$ = 13 TeV and constraints on dark matter and other models". In: *Phys. Lett. B* 769 (2017), p. 520. DOI: 10.1016/j.physletb.2017.02.012. arXiv: 1611.03568 [hep-ex] (cit. on pp. 79, 80, 84).

[129] ATLAS Collaboration. "Search for Low-Mass Dijet Resonances Using Trigger-Level Jets with the ATLAS Detector in pp Collisions at $\sqrt{s}$ = 13 TeV". In: *Phys. Rev. Lett.* 121 (2018), p. 081801. DOI: 10.1103/PhysRevLett.121.081801. arXiv: 1804.03496 [hep-ex] (cit. on pp. 79, 80, 84).

[130] ATLAS Collaboration. "Search for new phenomena in dijet events using 37 fb^{-1} of pp collision data collected at $\sqrt{s}$ = 13 TeV with the ATLAS detector". In: *Phys. Rev. D* 96 (2017), p. 052004. DOI: 10.1103/PhysRevD.96.052004. arXiv: 1703.09127 [hep-ex] (cit. on pp. 79, 84).

[131] Bogdan A. Dobrescu and Felix Yu. "Coupling-mass mapping of dijet peak searches". In: *Phys. Rev. D* 88.3 (2013), p. 035021. DOI: 10.1103/PhysRevD.90.079901. arXiv: 1306.2629 [hep-ph] (cit. on p. 80).

[132] Robert M. Harris and Konstantinos Kousouris. "Searches for dijet resonances at hadron colliders". In: *Int. J. Mod. Phys. A* 26 (2011), pp. 5005–5055. DOI: 10.1142/S0217751X11054905. arXiv: 1110.5302 [hep-ex] (cit. on p. 80).

[133] Haipeng An, Ran Huo, and Lian-Tao Wang. "Searching for low mass dark portal at the LHC". In: *Phys. Dark Univ.* 2 (2013), pp. 50–57. DOI: 10.1016/j.dark.2013.03.002. arXiv: 1212.2221 [hep-ph] (cit. on p. 80).

[134] Chase Shimmin and Daniel Whiteson. "Boosting low-mass hadronic resonances". In: *Phys. Rev. D* 94.5 (2016), p. 055001. DOI: 10.1103/PhysRevD.94.055001. arXiv: 1602.07727 [hep-ph] (cit. on p. 80).

[135] ATLAS Collaboration. "Search for light resonances decaying to boosted quark pairs and produced in association with a photon or a jet in proton–proton collisions at $\sqrt{s}$ = 13 TeV with the ATLAS detector". In: *Phys. Lett. B* 788 (2019), pp. 316–335. DOI: 10.1016/j.physletb.2018.09.062. arXiv: 1801.08769 [hep-ex] (cit. on p. 80).

[136] CMS Collaboration. "Search for low mass vector resonances decaying into quark–antiquark pairs in proton–proton collisions at $\sqrt{s}$ = 13 TeV". In: *JHEP* 01 (2018), p. 097. DOI: 10.1007/JHEP01(2018)097. arXiv: 1710.00159 [hep-ex] (cit. on p. 80).

[137] CMS Collaboration. "Search for low-mass resonances decaying into bottom quark-antiquark pairs in proton-proton collisions at $\sqrt{s}$ = 13 TeV". In: *Phys. Rev.* D99.1 (2019), p. 012005. DOI: 10.1103/PhysRevD.99.012005. arXiv: 1810.11822 [hep-ex] (cit. on p. 80).

[138] ATLAS Collaboration. "Search for resonances in the mass distribution of jet pairs with one or two jets identified as b-jets in proton–proton collisions at $\sqrt{s}$ = 13 TeV with the ATLAS detector". In: *Phys. Rev. D* 98 (2018), p. 032016. DOI: 10.1103/PhysRevD.98.032016. arXiv: 1805.09299 [hep-ex] (cit. on p. 80).

[139] CMS Collaboration. "Search for Narrow Resonances in the b-Tagged Dijet Mass Spectrum in Proton–Proton Collisions at $\sqrt{s}$ = 8 TeV". In: *Phys. Rev. Lett.* 120 (2018), p. 201801. DOI: 10.1103/PhysRevLett.120.201801. arXiv: 1802.06149 [hep-ex] (cit. on p. 80).

[140] ATLAS Collaboration. *Tagging and suppression of pileup jets with the ATLAS detector*. ATLAS-CONF-2014-018. 2014. URL: https://cds.cern.ch/record/1700870 (cit. on p. 81).

[141] ATLAS Collaboration. "Measurement of the photon identification efficiencies with the ATLAS detector using LHC Run 2 data collected in 2015 and 2016". In: *Submitted to: Eur. Phys. J.* (2018). arXiv: 1810.05087 [hep-ex] (cit. on pp. 81, 82, 90).

[142] ATLAS Collaboration. "Electron and photon energy calibration with the ATLAS detector using LHC Run 1 data". In: *Eur. Phys. J. C* 74 (2014), p. 3071. DOI: 10.1140/epjc/s10052-014-3071-4. arXiv: 1407.5063 [hep-ex] (cit. on p. 81).

[143] ATLAS Collaboration. "Electron and photon energy calibration with the ATLAS detector using 2015-2016 LHC proton-proton collision data". In: (2018). arXiv: 1812.03848 [hep-ex] (cit. on p. 82).

[144] ATLAS Collaboration. "Search for new phenomena in high-mass diphoton final states using 37 fb^{-1} of proton–proton collisions collected at $\sqrt{s}$ = 13 TeV with the ATLAS detector". In: *Phys. Lett. B* 775 (2017), p. 105. DOI: 10.1016/j.physletb.2017.10.039. arXiv: 1707.04147 [hep-ex] (cit. on p. 82).

[145] M. Cacciari, G.P. Salam, and G. Soyez. "The anti-k$_t$ jet clustering algorithm". In: *JHEP* 04 (2008), p. 063. DOI: 10.1088/1126-6708/2008/04/063. arXiv: 0802.1189 [hep-ph] (cit. on p. 82).

[146] M. Cacciari and G.P. Salam. "Dispelling the N^3 myth for the k_t jet-finder". In: *Phys. Lett. B* 641 (2006), p. 57. DOI: 10.1016/j.physletb.2006.08.037. arXiv: hep-ph/0512210 (cit. on p. 82).

[147] ATLAS Collaboration. "Topological cell clustering in the ATLAS calorimeters and its performance in LHC Run 1". In: *Eur. Phys. J. C* 77 (2017), p. 490. DOI: 10.1140/epjc/s10052-017-5004-5. arXiv: 1603.02934 [hep-ex] (cit. on p. 82).

[148] ATLAS Collaboration. *Selection of jets produced in* 13 *TeV proton–proton collisions with the ATLAS detector*. ATLAS-CONF-2015-029. 2015. URL: https://cds.cern.ch/record/2037702 (cit. on p. 82).

[149] ATLAS Collaboration. "Performance of pile-up mitigation techniques for jets in pp collisions at $\sqrt{s}$ = 8 TeV using the ATLAS detector". In: *Eur. Phys. J. C* 76 (2016), p. 581. DOI: 10.1140/epjc/s10052-016-4395-z. arXiv: 1510.03823 [hep-ex] (cit. on p. 82).

[150] ATLAS Collaboration. "Jet energy scale measurements and their systematic uncertainties in proton–proton collisions at $\sqrt{s}$ = 13 TeV with the ATLAS detector". In: *Phys. Rev. D* 96 (2017), p. 072002. DOI: 10.1103/PhysRevD.96.072002. arXiv: 1703.09665 [hep-ex] (cit. on pp. 82, 88, 90).

[151] ATLAS Collaboration. *Optimisation and performance studies of the ATLAS b-tagging algorithms for the 2017-18 LHC run*. ATL-PHYS-PUB-2017-013. 2017. URL: https://cds.cern.ch/record/2273281 (cit. on p. 82).

[152] ATLAS Collaboration. "Measurements of b-jet tagging efficiency with the ATLAS detector using $t\bar{t}$ events at $\sqrt{s}$ = 13 TeV". In: *JHEP* 08 (2018), p. 089. DOI: 10.1007/JHEP08(2018)089. arXiv: 1805.01845 [hep-ex] (cit. on pp. 82, 90).

[153] T. Gleisberg et al. "Event generation with SHERPA 1.1". In: *JHEP* 02 (2009), p. 007. DOI: 10.1088/1126-6708/2009/02/007. arXiv: 0811.4622 [hep-ph] (cit. on p. 85).

[154] Steffen Schumann and Frank Krauss. "A parton shower algorithm based on Catani-Seymour dipole factorisation". In: *JHEP* 03 (2008), p. 038. DOI: 10.1088/1126-6708/2008/03/038. arXiv: 0709.1027 [hep-ph] (cit. on p. 85).

[155] Stefan Höeche et al. "QCD matrix elements and truncated showers". In: *JHEP* 05 (2009), p. 053. DOI: 10.1088/1126-6708/2009/05/053. arXiv: 0903.1219 [hep-ph] (cit. on p. 85).

[156] Hung-Liang Lai et al. "New parton distributions for collider physics". In: *Phys. Rev. D* 82 (2010), p. 074024. DOI: 10.1103/PhysRevD.82.074024. arXiv: 1007.2241 [hep-ph] (cit. on p. 85).

[157] CDF Collaboration. "Global search for new physics with 2.0 fb^{-1} at CDF". In: *Phys. Rev. D* 79 (2009), p. 011101. DOI: 10.1103/PhysRevD.79.011101. arXiv: 0809.3781 [hep-ex] (cit. on p. 87).

[158] G. Choudalakis. *On hypothesis testing, trials factor, hypertests and the BumpHunter*. 2011. arXiv: 1101.0390 [physics.data-an] (cit. on p. 87).

[159] J. Alwall et al. "The automated computation of tree-level and next-to-leading order differential cross sections, and their matching to parton shower simulations". In: *JHEP* 07 (2014), p. 079. DOI: 10.1007/JHEP07(2014)079. arXiv: 1405.0301 [hep-ph] (cit. on p. 87).

[160] Richard D. Ball et al. "Parton distributions with LHC data". In: *Nucl. Phys. B* 867 (2013), pp. 244–289. DOI: 10.1016/j.nuclphysb.2012.10.003. arXiv: 1207.1303 [hep-ph] (cit. on p. 87).

[161] Torbjorn Sjöstrand, Stephen Mrenna, and Peter Z. Skands. "A brief introduction to PYTHIA 8.1". In: *Comput. Phys. Commun.* 178 (2008), pp. 852–867. DOI: 10.1016/j.cpc.2008.01.036. arXiv: 0710.3820 [hep-ph] (cit. on p. 87).

[162] ATLAS Collaboration. *ATLAS Pythia 8 tunes to 7 TeV data*. ATL-PHYS-PUB-2014-021. 2014. URL: https://cds.cern.ch/record/1966419 (cit. on pp. 87, 97).

[163] ATLAS Collaboration. *A method for the construction of strongly reduced representations of ATLAS experimental uncertainties and the application thereof to the jet energy scale*. ATL-PHYS-PUB-2015-014. 2015. URL: https://cds.cern.ch/record/2037436 (cit. on p. 88).

[164] ATLAS Collaboration. *Jet calibration and systematic uncertainties for jets reconstructed in the ATLAS Detector at* $\sqrt{s}$ = 13 *TeV*. ATL-PHYS-PUB-2015-015. 2015. URL: https://cds.cern.ch/record/2037613 (cit. on p. 88).

[165] ATLAS Collaboration. "Luminosity determination in *pp* collisions at $\sqrt{s}$ = 8 TeV using the ATLAS detector at the LHC". In: *Eur. Phys. J. C* 76 (2016), p. 653. DOI: 10.1140/epjc/s10052-016-4466-1. arXiv: 1608.03953 [hep-ex] (cit. on p. 90).

[166] G. Avoni et al. "The new LUCID-2 detector for luminosity measurement and monitoring in ATLAS". In: *JINST* 13.07 (2018), P07017. DOI: 10.1088/1748-0221/13/07/P07017 (cit. on p. 90).

[167] et. al Aaboud. "Search for new high-mass phenomena in the dilepton final state using 36 fb^{-1} of proton-proton collision data at $\sqrt{s}$ = 13 TeV with the ATLAS detector. Search for new high-mass phenomena in the dilepton final state using 36.1 fb^{-1} of proton-proton collision data at $\sqrt{s}$ = 13 TeV with the ATLAS detector". In: *JHEP* 10 (2017), 182. 42 p. DOI: 10.1007/JHEP10(2017)182. arXiv: 1707.02424. URL: https://cds.cern.ch/record/2273892 (cit. on p. 92).

[168] G. et. al. Aad. "Search for high-mass dilepton resonances using 139 fb-1 of pp collision data collected at s=13 TeV with the ATLAS detector". In: *Physics Letters B* 796 (2019), 68–87. ISSN: 0370-2693. DOI: 10.1016/j.physletb.2019.07.016. URL: http://dx.doi.org/10.1016/j.physletb.2019.07.016 (cit. on p. 92).

[169] Patrick Meade and Lisa Randall. "Black holes and quantum gravity at the LHC". In: *Journal of High Energy Physics* 2008.05 (2008), 003–003. ISSN: 1029-8479. DOI: 10.1088/1126-6708/2008/05/003. URL: http://dx.doi.org/10.1088/1126-6708/2008/05/003 (cit. on p. 93).

[170] M. V. Chizhov, V. A. Bednyakov, and J. A. Budagov. "Proposal for chiral-boson search at LHC via their unique new signature". In: *Physics of Atomic Nuclei* 71.12 (2008), 2096–2100. ISSN: 1562-692X. DOI: 10.1134/s1063778808120107. URL: http://dx.doi.org/10.1134/S1063778808120107 (cit. on p. 93).

[171] *Search for a narrow resonance decaying to a pair of muons in proton-proton collisions at 13 TeV*. Tech. rep. Geneva: CERN, 2019. URL: https://cds.cern.ch/record/2684861 (cit. on p. 93).

[172] Aaij et. al. "Searches for low-mass dimuon resonances". In: *JHEP* 2010 (2020). All figures and tables, along with machine-readable versions and any supplementary material and additional information, are available at https://cern.ch/lhcbproject/Publications/p/LHCb-PAPER-2020-013.html (LHCb public pages), 156. 27 p. DOI: 10.1007/JHEP10(2020)156. arXiv: 2007.03923. URL: https://cds.cern.ch/record/2722971 (cit. on p. 93).

[173] J. Alwall et al. "The automated computation of tree-level and next-to-leading order differential cross sections, and their matching to parton shower simulations". In: *Journal of High Energy Physics* 2014.7 (2014). ISSN: 1029-8479. DOI: 10.1007/jhep07(2014)079. URL: http://dx.doi.org/10.1007/JHEP07(2014)079 (cit. on p. 95).

[174] Torbjörn Sjöstrand, Stephen Mrenna, and Peter Skands. "A brief introduction to PYTHIA 8.1". In: *Computer Physics Communications* 178.11 (2008), 852–867. ISSN: 0010-4655. DOI: 10.1016/j.cpc.2008.01.036. URL: http://dx.doi.org/10.1016/j.cpc.2008.01.036 (cit. on p. 95).

[175] Sea Agostinelli et al. "GEANT4—a simulation toolkit". In: *Nuclear instruments and methods in physics research section A: Accelerators, Spectrometers, Detectors and Associated Equipment* 506.3 (2003), pp. 250–303 (cit. on p. 95).

[176] Giacomo Artoni et al. *Search for the Higgs boson decaying to a pair of muons in pp collisions at $\sqrt{s}$ = 13 TeV with the ATLAS detector: Support note with updates on the EPS 2019 CONF-note analysis.* Tech. rep. Geneva: CERN, 2019. URL: https://cds.cern.ch/record/2703492 (cit. on p. 97).

[177] Nathaniel Craig et al. *The unexplored landscape of two-body resonances*. 2016. arXiv: 1610.09392 [hep-ph] (cit. on p. 109).

[178] Nima Arkani-Hamed et al. *MARMOSET: The Path from LHC Data to the New Standard Model via On-Shell Effective Theories*. 2007. arXiv: hep-ph/0703088 [hep-ph] (cit. on pp. 110, 112).

[179] Shaouly Bar-Shalom and Arvind Rajaraman. "Models and phenomenology of maximal flavor violation". In: *Physical Review D* 77.9 (2008). ISSN: 1550-2368. DOI: 10.1103/physrevd.77.095011. URL: http://dx.doi.org/10.1103/PhysRevD.77.095011 (cit. on p. 113).

[180] Gian Francesco Giudice, Ben Gripaios, and Raman Sundrum. "Flavourful production at hadron colliders". In: *Journal of High Energy Physics* 2011.8 (2011). ISSN: 1029-8479. DOI: 10.1007/jhep08(2011)055. URL: http://dx.doi.org/10.1007/JHEP08(2011)055 (cit. on p. 113).

[181] G. et. al. Aad. "Search for high-mass dilepton resonances in pp collisions at s=8 TeV with the ATLAS detector". In: *Physical Review D* 90.5 (2014). ISSN: 1550-2368. DOI: 10.1103/physrevd.90.052005. URL: http://dx.doi.org/10.1103/PhysRevD.90.052005 (cit. on p. 116).

[182] G. et. al. Aad. "Search for anomalous production of prompt same-sign lepton pairs and pair-produced doubly charged Higgs bosons with s = 8 $\sqrt{s}$ = 8 TeV pp collisions using the ATLAS detector". In: *Journal of High Energy Physics* 2015.3 (2015). ISSN: 1029-8479. DOI: 10.1007/jhep03(2015)041. URL: http://dx.doi.org/10.1007/JHEP03(2015)041 (cit. on p. 116).

[183] V. et al Khachatryan. "Search for lepton flavour violating decays of heavy resonances and quantum black holes to an eμe μ pair in proton–proton collisions at $\sqrt{s}$ = 8 TeVs=8TeV". In: *The European Physical Journal C* 76.6 (2016). ISSN: 1434-6052. DOI: 10.1140/epjc/s10052-016-4149-y. URL: http://dx.doi.org/10.1140/epjc/s10052-016-4149-y (cit. on p. 116).

[184] G. et. al. Aad. "Search for a Heavy Neutral Particle Decaying toeμ,eτ, or $\mu\tau$ in pp Collisions at s=8 TeVwith the ATLAS Detector". In: *Physical Review Letters* 115.3 (2015). ISSN: 1079-7114. DOI: 10.1103/physrevlett.115.031801. URL: http://dx.doi.org/10.1103/PhysRevLett.115.031801 (cit. on p. 116).

[185] G. et. al. Aad. "A search for high-mass resonances decaying to τ + $\tau-$ in pp collisions at $\sqrt{s}$ = 8 TeV with the ATLAS detector". In: *Journal of High Energy Physics* 2015.7 (2015). ISSN: 1029-8479. DOI: 10.1007/jhep07(2015)157. URL: http://dx.doi.org/10.1007/JHEP07(2015)157 (cit. on p. 116).

[186] V. et. al Khachatryan. "Search for third-generation scalar leptoquarks in the tτ channel in proton-proton collisions at $\sqrt{s}$ = 8TeV". In: *Journal of High Energy Physics* 2015.7 (2015). ISSN: 1029-8479. DOI: 10.1007/jhep07(2015)042. URL: http://dx.doi.org/10.1007/JHEP07(2015)042 (cit. on p. 116).

[187] G. et. al. Aad. "Search for high-mass diphoton resonances inppcollisions ats=8 TeVwith the ATLAS detector". In: *Physical Review D* 92.3 (2015). ISSN: 1550-2368. DOI: 10.1103/physrevd.92.032004. URL: http://dx.doi.org/10.1103/PhysRevD.92.032004 (cit. on p. 116).

[188] V. Khachatryan. "Search for excited quarks in the γ+jet final state in proton–proton collisions at s=8 TeV". In: *Physics Letters B* 738 (2014), 274–293. ISSN: 0370-2693. DOI: 10.1016/j.physletb.2014.09.048. URL: http://dx.doi.org/10.1016/j.physletb.2014.09.048 (cit. on p. 116).

[189] G. et. al. Aad. "Search for new phenomena in photon+jet events collected in proton–proton collisions at $\sqrt{s} = 13$ with the ATLAS detector". In: *Physics Letters B* 728 (2014), 562–578. ISSN: 0370-2693. DOI: 10.1016/j.physletb.2013.12.029. URL: http://dx.doi.org/10.1016/j.physletb.2013.12.029 (cit. on p. 116).

[190] G. et. al Aad. "Search for new phenomena with photon+jet events in proton-proton collisions at s = 13 $\sqrt{s}$ = 13 TeV with the ATLAS detector". In: *Journal of High Energy Physics* 2016.3 (2016). ISSN: 1029-8479. DOI: 10.1007/jhep03(2016)041. URL: http://dx.doi.org/10.1007/JHEP03(2016)041 (cit. on p. 116).

[191] G. et al Aad. "Search for new resonances in Wγ and Zγ final states in pp collisions at s=8 TeV with the ATLAS detector". In: *Physics Letters B* 738 (2014), 428–447. ISSN: 0370-2693. DOI: 10.1016/j.physletb.2014.10.002. URL: http://dx.doi.org/10.1016/j.physletb.2014.10.002 (cit. on p. 116).

[192] G. et. al Aad. "Search for new phenomena in the dijet mass distribution usingppcollision data ats=8 TeVwith the ATLAS detector". In: *Physical Review D* 91.5 (2015). ISSN: 1550-2368. DOI: 10.1103/physrevd.91.052007. URL: http://dx.doi.org/10.1103/PhysRevD.91.052007 (cit. on p. 116).

[193] *Search for Heavy Resonances Decaying into bb and bg Final States in pp Collisions at sqrt(s) = 8 TeV*. Tech. rep. Geneva: CERN, 2013. URL: https://cds.cern.ch/record/1542405 (cit. on p. 116).

[194] G. et. al. Aad. "Search for resonant top quark plus jet production intt¯+jetsevents with the ATLAS detector inppcollisions ats=7 TeV". In: *Physical Review D* 86.9 (2012). ISSN: 1550-2368. DOI: 10.1103/physrevd.86.091103. URL: http://dx.doi.org/10.1103/PhysRevD.86.091103 (cit. on p. 116).

[195] V. et. al. Khachatryan. "Search for massive resonances in dijet systems containing jets tagged as W or Z boson decays in pp collisions at $\sqrt{s}$= 8 TeV". In: *Journal of High Energy Physics* 2014.8 (2014). ISSN: 1029-8479. DOI: 10.1007/jhep08(2014)173. URL: http://dx.doi.org/10.1007/JHEP08(2014)173 (cit. on p. 116).

[196] G. et. al. Aad. "Search for charged Higgs bosons in the H $\pm \rightarrow$ tb decay channel in pp collisions at s = 8 $\sqrt{s}$ = 8 TeV using the ATLAS detector". In: *Journal of High Energy Physics* 2016.3 (2016). ISSN: 1029-8479. DOI: 10.1007/jhep03(2016)127. URL: http://dx.doi.org/10.1007/JHEP03(2016)127 (cit. on p. 116).

[197] G. et. al Aad. "A search for t t ¯ $t\bar{t}$ resonances using lepton-plus-jets events in proton-proton collisions at s = 8 $\sqrt{s}$ = 8 TeV with the ATLAS detector". In: *Journal of High Energy Physics* 2015.8 (2015). ISSN: 1029-8479. DOI: 10.1007/jhep08(2015)148. URL: http://dx.doi.org/10.1007/JHEP08(2015)148 (cit. on p. 116).

[198] G. et. al. Aad. "Search for the production of single vector-like and excited quarks in the Wt final state in pp collisions at s = 8 $\sqrt{s}$ = 8 TeV with the ATLAS detector". In: *Journal of High Energy Physics* 2016.2 (2016). ISSN: 1029-8479. DOI: 10.1007/jhep02(2016)110. URL: http://dx.doi.org/10.1007/JHEP02(2016)110 (cit. on p. 116).

[199] G. et. al. Aad. "Search for a high-mass Higgs boson decaying to a W boson pair in pp collisions at s = 8 $\sqrt{s}$ = 8 TeV with the ATLAS detector". In: *Journal of High Energy Physics* 2016.1 (2016). ISSN: 1029-8479. DOI: 10.1007/jhep01(2016)032. URL: http://dx.doi.org/10.1007/JHEP01(2016)032 (cit. on p. 116).

[200] G. et. al Aad. "Search for high-mass diboson resonances with boson-tagged jets in proton-proton collisions at s = 8 $\sqrt{s}$ = 8 TeV with the ATLAS detector". In: *Journal of High Energy Physics* 2015.12 (2015), 1–39. ISSN: 1029-8479. DOI: 10.1007/jhep12(2015)055. URL: http://dx.doi.org/10.1007/JHEP12(2015)055 (cit. on p. 116).

[201] G. et. al. Aad. "Search for production of WW/WZ W W / W Z resonances decaying to a lepton, neutrino and jets in pp p p collisions at $\sqrt{s}$ = 8 s = 8 TeV with the ATLAS detector". In: *The European Physical Journal C* 75.5 (2015). ISSN: 1434-6052. DOI: 10.1140/epjc/s10052-015-3425-6. URL: http://dx.doi.org/10.1140/epjc/s10052-015-3425-6 (cit. on p. 116).

[202] V. et. al. Khachatryan. "Search for massive resonances decaying into pairs of boosted bosons in semi-leptonic final states at $\sqrt{s}$ = 8 TeV". In: *Journal of High Energy Physics* 2014.8 (2014). ISSN: 1029-8479. DOI: 10.1007/jhep08(2014)174. URL: http://dx.doi.org/10.1007/JHEP08(2014)174 (cit. on p. 116).

[203] V. et. al. Khachatryan. "Search for new resonances decaying via WZ to leptons in proton–proton collisions at s=8TeV". In: *Physics Letters B* 740 (2015), 83–104. ISSN: 0370-2693. DOI: 10.1016/j.physletb.2014.11.026. URL: http://dx.doi.org/10.1016/j.physletb.2014.11.026 (cit. on p. 116).

[204] G. et. al. Aad. "Combination of searches for WW, WZ, and ZZ resonances in pp collisions at s=8 TeV with the ATLAS detector". In: *Physics Letters B* 755 (2016), 285–305. ISSN: 0370-2693. DOI: 10.1016/j.physletb.2016.02.015. URL: http://dx.doi.org/10.1016/j.physletb.2016.02.015 (cit. on p. 116).

[205] G. Aad. "Search for a new resonance decaying to a W or Z boson and a Higgs boson in the". In: *The European Physical Journal C* 75.6 (2015). ISSN: 1434-6052. DOI: 10.1140/epjc/s10052-015-3474-x. URL: http://dx.doi.org/10.1140/epjc/s10052-015-3474-x (cit. on p. 116).

[206] V. et. al Khachatryan. "Search for massive WH resonances decaying into the". In: *The European Physical Journal C* 76.5 (2016). ISSN: 1434-6052. DOI: 10.1140/epjc/s10052-016-4067-z. URL: http://dx.doi.org/10.1140/epjc/s10052-016-4067-z (cit. on p. 116).

[207] V. et. al. Khachatryan. "Search for a massive resonance decaying into a Higgs boson and a W or Z boson in hadronic final states in proton-proton collisions at $\sqrt{s}$ = 8 TeV". In: *Journal of High Energy Physics* 2016.2 (2016). ISSN: 1029-8479. DOI: 10.1007/jhep02(2016)145. URL: http://dx.doi.org/10.1007/JHEP02(2016)145 (cit. on p. 116).

[208] G. et. al Aad. "Search for an additional, heavy Higgs boson in the $H \to ZZ$ H $\to$ Z Z decay channel at $\sqrt{s}$ = 8 TeV s = 8 TeV in p p collision data with the ATLAS detector". In: *The European Physical Journal C* 76.1 (2016). ISSN: 1434-6052. DOI: 10.1140/epjc/s10052-015-3820-z. URL: http://dx.doi.org/10.1140/epjc/s10052-015-3820-z (cit. on p. 116).

[209] V. et. al Khachatryan. "Search for a pseudoscalar boson decaying into a Z boson and the 125 GeV Higgs boson in l+l-bb- final states". In: *Physics Letters B* 748 (2015), 221–243. ISSN: 0370-2693. DOI: 10.1016/j.physletb.2015.07.010. URL: http://dx.doi.org/10.1016/j.physletb.2015.07.010 (cit. on p. 116).

[210] V. et. al. Khachatryan. "Search for narrow high-mass resonances in proton–proton collisions at s=8 TeV decaying to a Z and a Higgs boson". In: *Physics Letters B* 748 (2015), 255–277. ISSN: 0370-2693. DOI: 10.1016/j.physletb.2015.07.011. URL: http://dx.doi.org/10.1016/j.physletb.2015.07.011 (cit. on p. 116).

[211] G. et. al Aad. "Searches for Higgs boson pair production in the hh→ bb$\tau\tau$,$\gamma\gamma$WW*,$\gamma\gamma$bb, bbbb channels with the ATLAS detector". In: *Physical Review D* 92.9 (2015). ISSN: 1550-2368. DOI: 10.1103/physrevd.92.092004. URL: http://dx.doi.org/10.1103/PhysRevD.92.092004 (cit. on p. 116).

[212] V. et. al Khachatryan. "Search for resonant pair production of Higgs bosons decaying to two bottom quark–antiquark pairs in proton–proton collisions at 8 TeV". In: *Physics Letters B* 749 (2015), 560–582. ISSN: 0370-2693. DOI: 10.1016/j.physletb.2015.08.047. URL: http://dx.doi.org/10.1016/j.physletb.2015.08.047 (cit. on p. 116).

[213] *Search for resonant pair production of Higgs bosons decaying to $b\bar{b}$ and $\tau^+\tau^-$ in proton-proton collisions at $\sqrt{s}$ = 8 TeV*. Tech. rep. Geneva: CERN, 2015. URL: https://cds.cern.ch/record/2125293 (cit. on p. 116).

[214] V. et. al Khachatryan. "Search for heavy resonances decaying to two Higgs bosons in final states containing four b quarks". In: *The European Physical Journal C* 76.7 (2016). ISSN: 1434-6052. DOI: 10.1140/epjc/s10052-016-4206-6. URL: http://dx.doi.org/10.1140/epjc/s10052-016-4206-6 (cit. on p. 116).

[215] Jeong Han Kim et al. "The motivation and status of two-body resonance decays after the LHC Run 2 and beyond". In: *Journal of High Energy Physics* 2020.4 (2020). ISSN: 1029-8479. DOI: 10.1007/jhep04(2020)030. URL: http://dx.doi.org/10.1007/JHEP04(2020)030 (cit. on p. 118).

[216] M. Aaboud. "A strategy for a general search for new phenomena using data-derived signal regions and its application within the ATLAS experiment". In: *The European Physical Journal C* 79.2 (2019). ISSN: 1434-6052. DOI: 10.1140/epjc/s10052-019-6540-y. URL: http://dx.doi.org/10.1140/epjc/s10052-019-6540-y (cit. on p. 119).

[217] Jack H. Collins, Kiel Howe, and Benjamin Nachman. "Extending the search for new resonances with machine learning". In: *Physical Review D* 99.1 (2019). ISSN: 2470-0029. DOI: 10.1103/physrevd.99.014038. URL: http://dx.doi.org/10.1103/PhysRevD.99.014038 (cit. on p. 119).

[218] G. et. al. Aad. "Dijet Resonance Search with Weak Supervision Using s=13TeV pp Collisions in the ATLAS Detector". In: *Physical Review Letters* 125.13 (2020). ISSN: 1079-7114. DOI: 10.1103/physrevlett.125.131801. URL: http://dx.doi.org/10.1103/PhysRevLett.125.131801 (cit. on p. 120).